

**LIBRARY  
Michigan State  
University**

**PLACE IN RETURN BOX to remove this checkout from your record.  
TO AVOID FINES return on or before date due.**

<b>DATE DUE</b>	<b>DATE DUE</b>	<b>DATE DUE</b>
_____	_____	_____
_____	_____	_____
_____	_____	_____
_____	_____	_____
_____	_____	_____
_____	_____	_____
_____	_____	_____

STRUCTURAL PROPERTIES  
OF  
MISMATCHED ALLOYS

By

Normand Mousseau

A THESIS

Submitted to

Michigan State University

in partial fulfillment of the requirements

for the degree of

DOCTOR OF PHILOSOPHY

Department of Physics and Astronomy

1993

# ABSTRACT

## STRUCTURAL PROPERTIES OF MISMATCHED ALLOYS

By

Normand Mousseau

The problem of understanding the local structure of disordered alloys has been around for a long time. In this thesis, I look more specifically at the effect of size-mismatch disorder in binary alloys under many forms: metallic and semiconductor alloys, bulk and surfaces, two and three dimensional systems. I have studied the limitations of a central-force model (CFM) and an embedded-atom potential (EAM) in describing the local structure of binary metallic alloys composed of Ag, Au, Cu, Ni, Pd, or Pt. Although an analytical model developed using the CFM explains qualitatively well the experimental and numerical results, in many cases, it is important to add electronic density effects through a more sophisticated potential like EAM in order to agree quantitatively with experiment. I have also looked at amorphous and crystalline silicon-germanium alloys. It turns out that the effect of size-mismatch is the same on a crystalline and an amorphous lattice. In the latter case, it can be seen as a perturbation of the much larger disorder due to the amorphisation process. However, the analytical predictions differ, for both the crystalline and amorphous alloys, from the experimental

results. If one is to believe the data, there is only one possible explanation for this inconsistency: large amounts of hydrogen are present in the samples used for the measurements. Since the data analysis of EXAFS results is not always straightforward, I have proposed some experiments that could shed light on this problem. One of these experiments would be to look at the (111) surface of a Si-Ge alloy with a scanning tunneling microscope. I also present in this thesis the theoretical predictions for the height distribution at the surface as well as some more general structural information about the relaxation in the network as one goes away from the surface. Finally, I have studied the effect of size-mismatch in a purely two dimensional lattice, looking for mismatch-driven phase transitions. Although it is possible to map size-mismatch on an effective temperature at low disorder, I have not been able to find any indication that a hexatic phase exists in these 2d systems. Since systems were studied with different potentials in very large unit cells, the conclusion is that the hexatic phase is not universal for two dimensional networks.

De choses répandues au hasard,  
le plus bel ordre, l'ordre-du-monde.

Héraclite

# ACKNOWLEDGEMENTS

I would like to express my deeper gratitude to my thesis advisor Professor Michael F. Thorpe for his constant support, his physical insight and for sharing with me his love of physics. During the last three years, he has guided me with confidence and humour through the meanders of research. His continual search for simplicity even in complex problems will always serve as a guide to me.

I am also grateful to Professors C. F. Foiles, S. D. Mahanti, R. Stein, D. Stump and D. Tománek for serving on my guidance committee. I would like to thank Mrs. Janet King for making life in this department so much simpler as well as MM. Ron Winsauer, Seong-Gon Kim and Dr. George Perkins for helping me with computers.

I wish to thank Dr. Yong Cai and M. Jidong Chen for their numerous discussions, comments and help at various stages of this work. I am grateful to Professor R. A. Johnson for discussions related to chapter 3, to Dr. S. de Gironcoli for sending me his numerical results used in chapter 4, to Professor F. Wooten for allowing me to use the coordinates of his  $\alpha$ -Si model and to Professor J. B. Boyce and Dr. G. S. Cargill III for useful comments regarding chapter 5.

Finally, I want to acknowledge the moral support given to me by my friends B. Djordjević, D. Vasiljević, F. Liu, G. Overney and J.-H. Pinto as well as those from Science Theatre, particularly D. Casavant, D. Bercik, D. Kuhl, J. Kriessler, J. Discenna, J. Conrad, R. Lambert, and S. Snyder. They all made my life much more enjoyable while I was in East Lansing.

Financial support from the Natural Sciences and Engineering Research Council of Canada, the Fonds pour la formation de chercheurs et l'aide à la recherche du Québec and the Center for Fundamental Materials Research of MSU without which this thesis could not have been, is also greatly acknowledged.

# Contents

<b>Abstract</b> . . . . .	i
<b>Acknowledgments</b> . . . . .	iv
<b>1 Introduction</b> . . . . .	<b>1</b>
1.1 Order and Disorder . . . . .	2
1.2 Alloys and Amorphous Systems . . . . .	4
1.2.1 Short-range order . . . . .	4
1.2.2 Medium-range order . . . . .	6
1.2.3 Long-range order (LRO) . . . . .	6
1.3 Understanding alloys . . . . .	7
1.4 EXAFS . . . . .	12
1.5 Conclusion . . . . .	19
<b>2 Theory</b> . . . . .	<b>21</b>
2.1 Bond mismatch . . . . .	22
2.2 Force constant disorder . . . . .	29
2.3 Site-mismatch . . . . .	29
2.4 $a^*$ and $a^{**}$ . . . . .	31
2.5 Semiconductors . . . . .	34
2.6 Correlation . . . . .	35

<i>CONTENTS</i>	vii
2.7 Conclusion . . . . .	36
<b>3 Metallic Alloys</b>	<b>39</b>
3.1 Embedded-atom method . . . . .	42
3.2 Central force model . . . . .	45
3.3 Computer simulations . . . . .	47
3.4 Results . . . . .	48
3.5 Conclusion . . . . .	64
<b>4 Crystalline and Amorphous SiGe</b>	<b>67</b>
4.1 Solution for binary alloys . . . . .	69
4.2 Results . . . . .	73
4.3 Effect of amorphisation . . . . .	78
4.4 Conclusion . . . . .	85
<b>5 About EXAFS Results</b>	<b>88</b>
5.1 Assumptions . . . . .	89
5.2 Comparison between theory and experiment . . . . .	90
5.3 Structural model . . . . .	95
5.4 Discussion . . . . .	105
5.5 Conclusion . . . . .	107
<b>6 Surface of semiconductors</b>	<b>108</b>
6.1 Theory . . . . .	109
6.1.1 Bond mismatch . . . . .	111
6.1.2 Site mismatch . . . . .	112
6.2 Topological rigidity parameters . . . . .	113

<i>CONTENTS</i>	viii
6.3 Triangular lattice . . . . .	115
6.4 Silicon-Germanium alloy . . . . .	117
6.5 Conclusion . . . . .	128
<b>7 Two-dimensional melting</b>	<b>131</b>
7.1 Review . . . . .	132
7.2 Theory . . . . .	139
7.3 Details of simulations . . . . .	141
7.4 Results . . . . .	145
7.5 Discussion . . . . .	155
7.6 Conclusion . . . . .	158
<b>8 Conclusion</b>	<b>161</b>
<b>A Conjugate-gradient method</b>	<b>165</b>
<b>B Johnson's long-range potential</b>	<b>169</b>
<b>Bibliography . . . . .</b>	<b>171</b>

# List of Figures

1.1	Sketch of chemical and structural disorder. . . . .	3
1.2	Characteristics of short- and medium-range order. . . . .	5
1.3	Nearest-neighbor distance for $\text{Ga}_{1-x}\text{In}_x\text{As}$ . . . . .	10
1.4	X-ray absorption coefficient. . . . .	13
1.5	Absorptance of Cu at the onset of Cu K-shell. . . . .	14
1.6	Origin of EXAFS. . . . .	15
1.7	EXAFS oscillations. . . . .	17
1.8	Fourier transform of the EXAFS signal. . . . .	17
2.1	Perfect triangular network. . . . .	22
2.2	Triangular network with bond mismatch. . . . .	23
2.3	Variation of the configurational energy. . . . .	28
2.4	Force constant disorder. . . . .	30
2.5	Representation of the topological rigidity parameters. . . . .	33
2.6	The topological rigidity $a^{**}$ and $2b^{**}$ . . . . .	36
2.7	Bond correlations. . . . .	37
3.1	Nearest-neighbor distances for $\text{Au}_{1-x}\text{Ag}_x$ . . . . .	49
3.2	Same as Figure 3.1, except for $\text{Cu}_{1-x}\text{Au}_x$ . . . . .	51
3.3	Same as Figure 3.1, except for $\text{Cu}_{1-x}\text{Pd}_x$ . . . . .	52

3.4	Same as Figure 3.1, except for $\text{Pd}_{1-x}\text{Pt}_x$ .	53
3.5	Same as Figure 3.1, except for $\text{Ni}_{1-x}\text{Ag}_x$ .	54
3.6	Same as Figure 3.1, except for $\text{Ni}_{1-x}\text{Au}_x$ .	56
3.7	Nearest-neighbor distances for alloys relaxed with the EAM potential.	59
3.8	Nearest-neighbor distances for alloys relaxed with the CFM potential.	60
3.9	Same as figure 3.8.	62
3.10	Bulk and shear modulus for three alloys.	63
3.11	Nearest-neighbor distances in $\text{Ni}_{0.5}\text{Au}_{0.5}$ .	65
4.1	Nearest-neighbor bond lengths for $\text{Si}_{1-x}\text{Ge}_x$ .	74
4.2	Nearest-neighbor bond lengths distribution for $\text{Si}_{0.55}\text{Ge}_{0.45}$ .	76
4.3	Nearest-neighbor bond lengths distribution for $\text{Si}_{0.89}\text{Ge}_{0.11}$ .	77
4.4	Next-nearest-neighbor distance in $\text{Si}_{1-x}\text{Ge}_x$ .	79
4.5	Strained energy due to length mismatch in $\alpha\text{-Si}_{1-x}\text{Ge}_x$ .	80
4.6	Nearest-neighbor distance for $\alpha\text{-Si}_{1-x}\text{Ge}_x$ .	84
4.7	Next-nearest-neighbor distances in $\alpha\text{-Si}_{1-x}\text{Ge}_x$ .	86
5.1	Experimental nearest-neighbor distribution	94
5.2	Nearest-neighbor length distribution for $c\text{-Si}_{1-x}\text{Ge}_x$ : H.	97
5.3	Variation of the topological rigidity parameter with the mean coordination.	99
5.4	Sketch of a cube, tube and plane with open surfaces.	101
5.5	Variation of the topological rigidity parameter for open surfaces.	102
5.6	Sketch of the proposed structural model for SiGe alloys.	103
5.7	Variation of the bulk modulus B as a function of the mean coordination.	104

6.1	Triangular network cut along (10) and (11) direction. . . . .	116
6.2	Variation of the topological rigidity parameter as a function of depth	118
6.3	Topological rigidity parameter as a function of the layer number for surface (111). . . . .	121
6.4	Topological rigidity parameter as a function of the layer number for surface (100). . . . .	122
6.5	Height distribution at the surface (111). . . . .	124
6.6	Gaussian fit for partial $z$ displacement distribution. . . . .	125
6.7	Si displacement distribution along $z$ . . . . .	126
6.8	Ge displacement distribution along $z$ . . . . .	127
6.9	Simulated density plot of the surface (111) of $Si_{50}Ge_{50}$ alloy. . . .	129
7.1	Different types defects on the two-dimensional triangular lattice. .	138
7.2	Proposed phase diagram of the two-dimensional melting in the mismatch-temperature plane. . . . .	142
7.3	Pseudo-harmonic potential. . . . .	144
7.4	First derivative of the pseudo-harmonic potential. . . . .	146
7.5	Position-position correlation for a pseudo-harmonic system. . . .	148
7.6	Position-position correlation for a Lennard-Jones system. . . . .	149
7.7	Angular correlations and defects for a pseudo-harmonic system. .	150
7.8	Angular correlations and defects for a Lennard-Jones system. . .	151
7.9	Configurational energy as a function of effective temperature. . . .	152
7.10	Splay rigidity. . . . .	154
7.11	Possible phase transitions for the KTHNY theory in the elastic constants-temperature space. . . . .	155
7.12	Pseudo-harmonic 50-50 alloys with 40% mismatch. . . . .	157

*LIST OF FIGURES*

xii

7.13 Lennard-Jones 50-50 alloy with 26% mismatch. . . . . 159

# List of Tables

3.1	Parameters for the Johnson EAM potential. . . . .	45
3.2	Recapitulation of the results for the CFM and EAM potentials. . . . .	58
4.1	Parameters for Kirkwood and Keating potentials. . . . .	69
4.2	Structural comparison between <i>a</i> -Si and <i>c</i> -Si <sub>1-x</sub> Ge <sub>x</sub> . . . . .	83
6.1	Partial displacements at the surface. . . . .	123
7.1	The three phases of a two-dimensional solid as predicted by the KTHNY theory with their associated correlation and defects. . . . .	135

# Chapter 1

## Introduction

Until the early sixties, the world as seen by most condensed-matter physicists consisted mainly of perfect crystals. Everything else, doped semiconductors, random alloys and glasses, was considered dirty and unworthy of research. As mathematical and computational tools developed in the sixties and the seventies, the importance and interest of these materials began to be appreciated in the physics community. By their nature, disordered systems are difficult to work with: their properties can vary widely from sample to sample, they often show more memory of the preparation method than pure crystals, etc. Moreover, the conceptual framework used in the study of crystals cannot always be extended directly to disordered systems. How can we define a defect in amorphous silicon, for example?

In this chapter, I will present some concepts that are useful when working with disordered systems, with a special emphasis on random alloys and amorphous materials. I will then examine some of the preceding approaches to understand random alloy structure and discuss their limitations. Finally, since much of this new work has been motivated by the development of the extended X-ray absorption fine structure scattering technique (EXAFS), I will briefly describe the theory

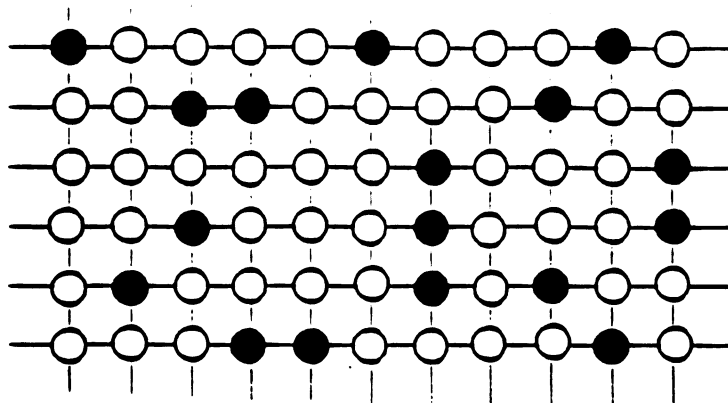
behind this experiment as well as its current possibilities and restrictions.

## 1.1 Order and Disorder

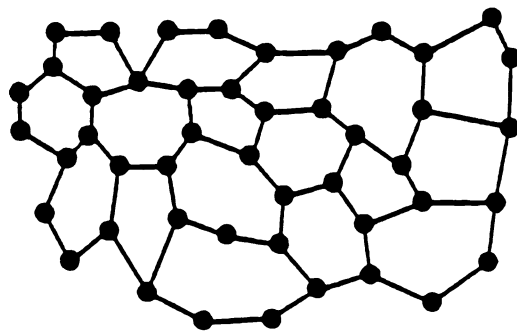
There are many levels of disorder in nature. Doped semiconductors, for example, are only weakly disordered with typically one impurity per thousand or more atoms. However, even such small quantities can have a decisive role in determining the electronic properties of materials. This disorder is very different from that found in glasses and amorphous solids. It is therefore important to try to classify these various structures. We can distinguish between two major classes of disorder: chemical and structural disorder (see Figure 1.1). Each of these two classes can also be divided according to the length scale characterizing the absence of order.

For chemical disorder, different species of atoms are placed at random on a crystalline lattice which retains more or less its original symmetries. In this class are solid solutions (or random alloys), substitutional impurities and vacancies, the main difference between the first two being the concentration of the different constituents. Substitutional impurities are typically very dilute and do not interact with each other; solid solutions are a mixture of two or more atomic species with comparable concentration. For a long time, physicists believed that most structural quantities in random alloys could be modeled correctly with a simple average over properties of the constituent species. However, as it has been discovered in the last decade, the situation is not so simple.

Glasses and amorphous solids are characterized by structural disorder. In most cases, the coordination is maintained, but there is no remnant of crystalline structure beyond the first-neighbor shell; these states are more akin to a liquid than a crystalline phase. Glasses and amorphous solids can exist in the pure



(a)



(b)

Figure 1.1: (a) Representation of chemical disorder with two different species distributed randomly on a crystalline network and (b) structurally disordered lattice.

form or alloyed. The question of the glass transition remains one of the most important unsolved questions in contemporary condensed-matter physics. In spite of large amounts of work dedicated to this problem over the last two decades, many fundamental structural and electronic properties are not yet properly understood. For example, nobody has been able to obtain a satisfying model of the amorphous silicon structure by computer quenching, raising questions about the time scale involved in creating amorphous materials and in the validity of the interaction potentials used for these simulations.

## 1.2 Alloys and Amorphous Systems

Another important component of classification of these structure is related with the length scales for which the system is, or is not, ordered. The classification used here is described in more detail in a review article by S. R. Elliot (1989). It is usually divided in three length scales: short-, medium- and long-range order, each associated with different experimental probes.

### 1.2.1 Short-range order

There seems to be a consensus in the literature about the definition of short-range order (SRO). The SRO characterizes the purely local structure in a disordered material, i.e. the central atom and the first-neighbor shell. It is usually defined by the first-neighbor distance  $r_{ij}$  and by the bond angle  $\theta_{jik}$  as shown in Figure 1.2(a). In a constrained environment, the strain can be minimized by an equilibrium between these two quantities, depending upon the ratio of the angular to the stretching the force constant. In an amorphous materials (a-Si, for example),

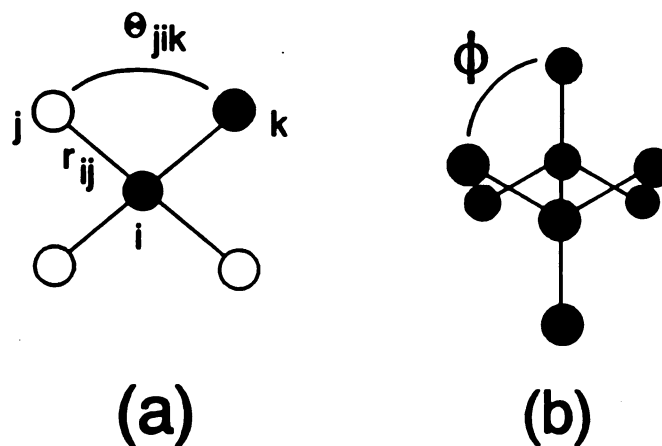


Figure 1.2: Characteristics of short- and medium- range order in a diamond lattice. (a) nearest-neighbor distance  $r$  and bonding angle  $\theta$ ; (b) Dihedral angle between to adjacent tetrahedra.

the average values of  $r_{ij}$  and  $\theta_{jik}$  and first-neighbor shell are very similar to the crystalline one; however, the fluctuations can be relatively large. In an random semiconductor alloy, although the average values of the bond angle and the first-neighbor distances are the same as for a pure semiconductor, the  $r_{ij}$  distribution possesses multiple peaks corresponding to preferred values for all the lengths in the problem.

In alloys, the short-range order is also defined by the correlation between first neighbors. Usually these correlations can be picked up by EXAFS or other diffraction experiments if they are strong; however, when the correlation is weak, varying only by a few percent from the random case, it is very difficult to obtain reliable experimental data and one must rely on analytical or computational work.

### 1.2.2 Medium-range order

It is possible to subdivide the medium-range order (MRO) in three parts (Elliot, 1989): near, medium and far medium-range order. I will consider here only the first (NMRO) part, placing the two others with the long-range order.

The near medium-range order is characterized mainly, in semiconductors, by the relative position of two neighboring tetrahedra, measured by the dihedral angle. (Figure 1.2(b)). This quantity is very important for amorphous materials because it is at this level that the differentiation really appears between disordered structures and crystals. In the case of alloys, the medium-range order is defined by a correlation between second or third neighbors. This local clustering is almost impossible to measure experimentally and the effects of such correlation have not been really studied yet. Generally speaking, because it is too large for scattering experiments and too small for direct observation, the MRO remains obscure. In spite of its importance for amorphous and for glasses, very little effort has been put into studying theoretically or experimentally the impact of varying the correlation in angle or concentration at this level. With the development of more powerful computers and more efficient semi-empirical potentials and *ab initio* methods, one expects to see major developments this direction over the next few years.

### 1.2.3 Long-range order (LRO)

The long-range order should be renamed long-range *structure* since it is difficult to imagine correlation at this scale; however, we can here include defects like microvoids, cracks and structural defects like disclinations. In multilayers, they often appear in order to release the strain energy due to lattice size mismatch. They are an indicator of the strain energy as well as the distance over which the lattice

perturbation relaxes when submitted to a very local strain, like the introduction of a larger atom in the lattice.

Although the disordered structures have been divided into many length scales, it is important to note that there is not always a clear cut distinction between these different length scales and that they often overlap. However, following the methods developed for the study of the crystal, most of the theoretical work in disordered systems has concentrated on the local order, while experiments can more easily be performed on large samples. In the world of crystals, the fluctuations are small, and average quantities obtained from x-ray diffraction and other global experiments are representative of their local values; the Bloch theorem guarantees a one to one correspondence between the local and the global properties. But the knowledge of the local situation in disordered materials is not enough to obtain a global understanding of the structure of the solid and vice versa. More effort has to be made in trying to link the properties of the disordered materials with medium and long range order. But for this, one must go beyond the usual theories of alloys and other disordered systems.

### 1.3 Understanding alloys

Until very recently, the understanding of the electronic properties of alloys was based on the virtual crystal approximation (VCA). In this theory, all the atoms are positioned on a crystalline lattice with a lattice parameter following, for most semiconductor alloys, the Végard's law (Végard, 1921),

$$d = (1 - x)d_A + xd_B, \quad (1.1)$$

where  $d$  is the lattice constant of the alloys  $A_{1-x}B_x$ . This empirical relation was proposed in the 1920s to support x-ray diffraction results. Local variations of the potential are averaged out and this quantity forms the basis for the calculation of the electronic properties. Since the fluctuations are washed away, the system recovers its symmetry, and periodicity and crystal states can be assigned. The VCA constitutes therefore an interpolation between the properties of the independent constituents. In spite of these limitations, the predictions of this theory have had a relative success, with agreement with experiment varying from excellent to poor. One of the difficulties in judging the quality of this approximation is that the experimental precision on spectroscopic and other electronic measurements is not precise enough to constitute an excellent test. Nevertheless, in view of certain discrepancies, some refinements of the VCA have been developed so as to include the random fluctuation potential. Since the discrepancies can be due to many phenomena—random fluctuations, ordering, clustering and impurities, for example—it becomes important to characterize the effects of each of these features separately.

The major refinement comes by going one step further, with the coherent potential approximation (CPA). Proposed independently by Soven (1967) and Taylor (1967) at the end of the sixties, this self-consistent method uses the average Green's function instead of the virtual crystal as the zeroth approximation. This approximation can be seen also as a mean-field approach to the multiscattering theory. Although there is no formal demonstration of the limits of this approximation, it usually works very well in the case of small fluctuations but fails when the fluctuations become very large—in one dimension, for example (Elliott et al, 1974).

At the beginning of the 1980s however, a major blow was given to all the schemes based on the virtual crystal approximation, shaking most of the concepts forming the basis of understanding the structure of alloys. In 1983, Mikkelsen and Boyce published their x-ray absorption fine structure (EXAFS) measurements indicating that, in the GaInAs random alloys, the Ga-As and In-As nearest-neighbor distances remained almost constant at all compositions. (see Figure 1.3). The distribution of nearest-neighbors was therefore not a small deviation from the Végard's law, but rather indicated that the lattice itself was very distorted in order to accommodate the different bond lengths disposed at random through the lattice. The justification for VCA and CPA were lost in great parts. The first theoretical explanation came from Zunger and Jaffe (1983) who proposed some local distortion of the underlying crystal lattice. For large enough mismatch, the atoms would gain by going locally from the zinc-blende structure to a chalcopyrite arrangement. They presented a zeroth order theory where the mismatch parameter determines how far the chalcopyrite departs from the zinc-blende structure. Although this model did not include the influence of the concentration on the position of the center and width of the partial length distributions, it provided a new view of the alloy problem with two distinct bond lengths averaging out the Végard's law.

Along with this important structural discovery was the realization that the strain, imposed on a binary alloy by fitting on the same lattice atoms of different sizes, cannot be neglected when trying to understand the electronic properties of an alloy. In 1982, Osbourn proposed that strained-layered structures could display electronic and optical properties not found in unstrained-constituent materials. Before him, the strain was considered as a necessary evil in the creation

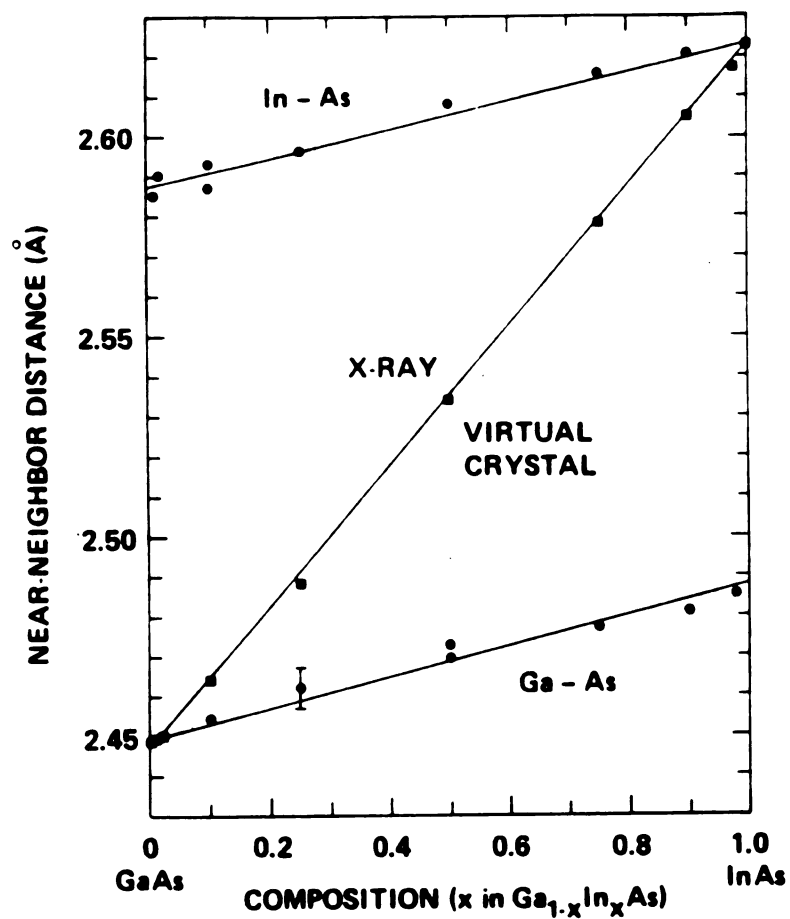


Figure 1.3: Partial and total first-neighbor distance for  $\text{Ga}_{1-x}\text{In}_x\text{As}$  as obtained experimentally by Mikkelsen and Boyce (1983).

of interesting semiconductor heterostructures. But because the strain produced internally by mixing size-mismatch elements can be much greater than that which can be obtained externally, effects on the band structure due to this phenomenon are not negligible. With a mismatch as small as 2%, the band structure will be modified by more than 100 meV (Pearsall, 1990). Today, a lot of effort is targeted to study the strain in multilayered compounds, specifically the reaction of the interface and the maximum thicknesses one can obtain without creating defects in the layers. In only a few years, this field has become a technological enterprise where the discoveries are almost directly applied to the development of optical devices.

More recently at MSU we worked on developing a structural model of alloys that would explain the EXAFS results in a consistent theory. This theory will be presented in more detail in chapter 1 and forms the basis of my thesis. Using harmonic interaction potentials, an *exact* expression for all the partial lengths in the binary, pseudo-binary, ternary and quaternary compounds as well as for multilayered materials has been obtained. The limits of the random model discussed here are obvious. Almost no disordered system presents perfectly random order, particularly when it comes to the choice of first and second neighbors. Even in the case of SiGe, which surely can be dubbed as one of the most perfect random binary structures, electronically speaking, recent measurements have shown that there is some correlation in molecular-beam-epitaxy grown films (Jesson *et al.*, 1992) although these correlations do not appear in the usual methods of preparing bulk alloys. The structural model is nevertheless extremely useful and must be considered as a valuable step for the understanding of alloys. First, it represents a huge step forward, compared with the VCA and CPA theories; second, although

it is not simple, it is possible to include corrections in this theory to take into account the effect of correlation particularly if these are weak like they seem to be in most semiconductor alloys. Furthermore, if the accuracy of the experiment could be increased enough to present noticeable deviation from this theory, it would allow for some quantitative measure of the correlation.

## 1.4 EXAFS

Since extended x-ray absorption fine structure spectroscopy (EXAFS) represents the major source of experimental results about the local structure of disordered systems, it is important to understand the underlying theory and limitations of the technique. Most of the material of this section has been taken from two review articles: Hayes and Boyce (1982) and Stern (1985). Although the fine structure at the absorption edge has been known for a long time, it is only about 25 years ago with the opening of two facilities producing an intense source of x-rays that the efforts to really understand the phenomenon were made. In this section, I will present a very condensed theory of EXAFS, followed by a discussion of different approximations and how they limit the information one can get from this method.

In Figure 1.4, one can see the variation of the x-ray absorption coefficient of copper metal with the energy of the incident photon. The coefficient decreases more or less monotonically except at some specific energies when a step occurs. These steps or absorption edges correspond to the binding energies of shells of electrons in the atom. In the Figure 1.4, two edges are indicated as the L-edge ( $n = 2$  shell electrons) and K-edge ( $n = 1$  shell electrons); just after the edge, the absorption coefficient shows a very rich behavior with peaks and valleys extending on about 1000 eV past the edge (Figure 1.5). The oscillations happening in the

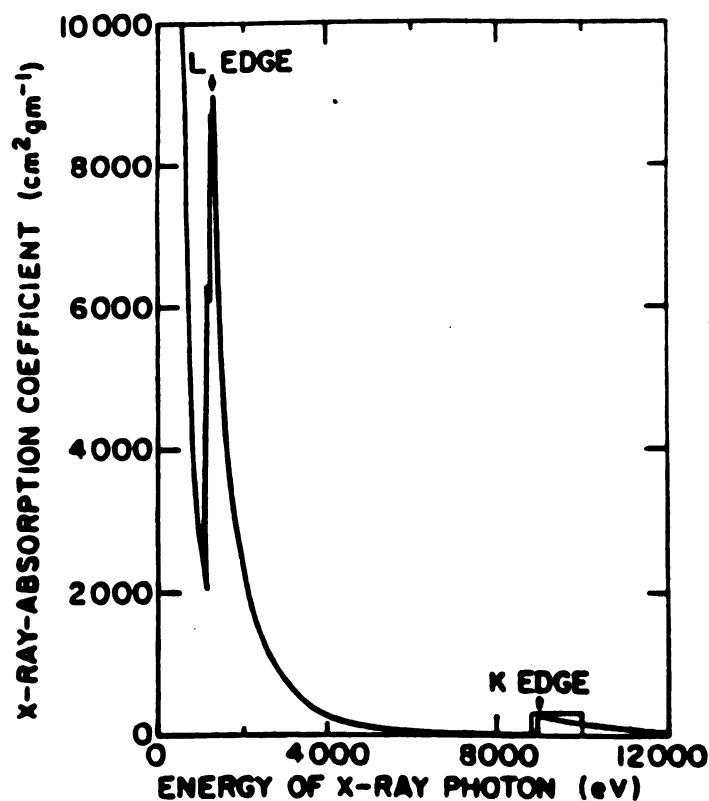


Figure 1.4: X-ray absorption coefficient as a function of photon energy (Stern, 1985)

first 20 eV after the edge are classified as near-edge (NEXAFS) region while the rest of the structure is called the extended x-ray absorption fine structure (EXAFS) region.

EXAFS is typically understood in terms of single-scattering phenomena. A photon excites an electron in the core shell of an atom. The photoexcited electron wave propagates and interferes with scattered waves from the surrounding atoms (Figure 1.6). The oscillations measured are a signature of these interferences and hence, of the local atomic structure. We can express this signature as a

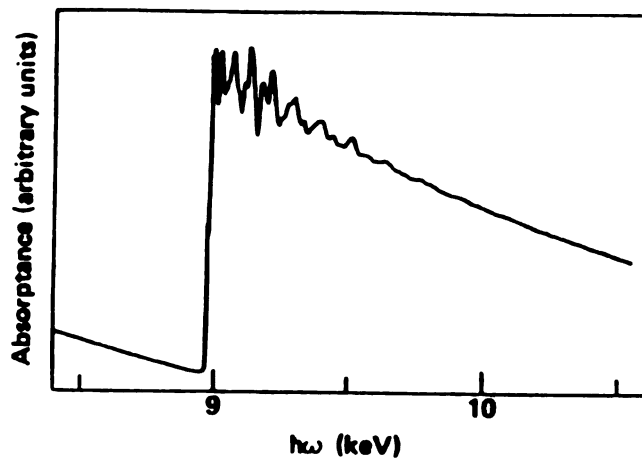


Figure 1.5: Absorbance of Cu metal at the onset of Cu K-shell absorption (Stern, 1985 )

perturbation  $\chi(\omega)$  over a smooth photoexcitation rate  $\sigma^0(\omega)$  that would be seen if the atom was isolated

$$\sigma(\omega) = \sigma^0(\omega) [1 + \chi(\omega)], \quad (1.2)$$

where  $\chi$  contains the EXAFS information. Since  $\chi$  is due to interference between backscattering waves and ongoing waves around an atom, the main contribution comes from the product of the photoelectron momentum  $k$  and twice the distance between the central atom and a neighbor,  $2r$ . If we also take into account the attenuation of the wave and the reflection coefficient of the neighboring atom, we can express  $\chi$  as

$$k\chi_\alpha(\omega) = \sum_\beta \int_0^\infty dr r^2 p_{\alpha\beta}(r) 2\text{Re} \left[ e^{2ikr} \Lambda_{\alpha\beta}(k, r) \right], \quad (1.3)$$

where

$$\Lambda_{\alpha\beta}(k, r) \simeq -\frac{2i\pi^2 m}{\hbar^2} t_\beta^+(-k, k) \exp \left[ -\frac{2}{\lambda(k)} + 2i\eta_\alpha(k) \right]. \quad (1.4)$$

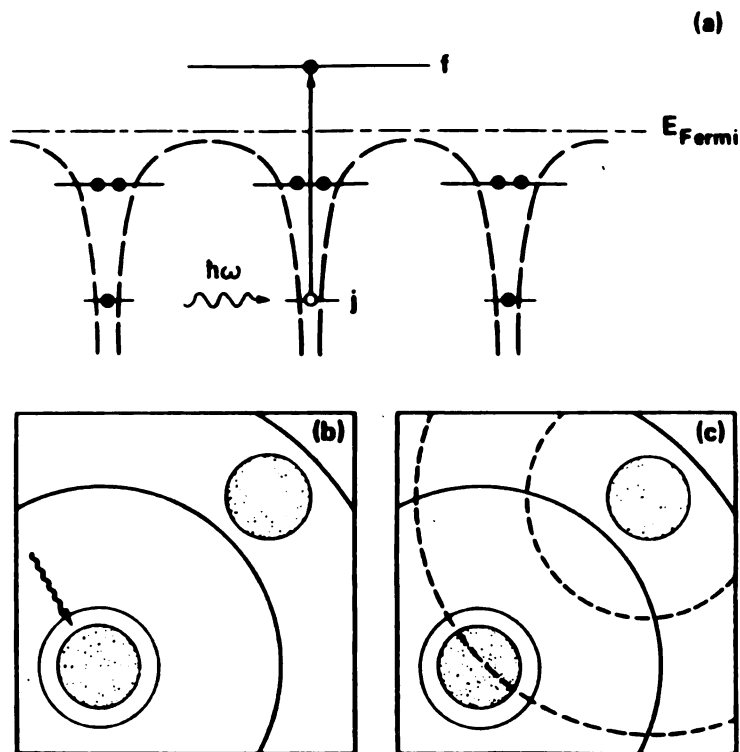


Figure 1.6: Origin of EXAFS. (a) A photon is absorbed by an atom, exciting an electron from the core state  $j$  to a continuum state. (b) The electronic wave propagates outward and interferes with neighboring atoms (c). (Hayes and Boyce, 1982).

The first equation gives the total contribution of all the atomic species  $\beta$  of the neighbors to a central atom of species  $\alpha$  as a function of the energy  $\hbar\omega$  on the incoming x-ray photon. The integral is the product of the radial distribution function  $p_{\alpha\beta}(r)$  and a complicated energy term  $\Lambda$ . This last term includes the scattering matrix  $t_{\beta}^+$ , the electron mean-free path length  $\lambda$  and the phase shift due to the potential of the excited atom  $\eta_{\alpha}$ . However, it does not include many-body correlations (angular dependence, etc.), which makes it simple to use in the analysis of the experimental results.

From the absorptance of Cu (Figure 1.5), it is possible to extract the

quantity  $k\chi$  (Figure 1.7). If only one distance entered in the radial distribution function (RDF), we would expect to see only one frequency in the EXAFS oscillations; however, there are many frequencies on this Figure. Since it is easier to understand the RDF in real space, we can Fourier transform (FT) the signal (Equation 1.3):

$$\phi_\alpha \simeq \sum_\beta \int_0^\infty dr' r'^{-2} p_{\alpha\beta}(r') \xi_{\alpha\beta}(r - r'), \quad (1.5)$$

where

$$\xi_{\alpha\beta}(r, r'') = FT[W(k)\Lambda_{\alpha,\beta}(k, r'')], \quad (1.6)$$

and  $W(k)$  is a square window function. So  $\phi$  is essentially a linear combination of  $\xi$ 's, one for each peak in the RDF. However, looking at the Fourier transform of the Cu K-shell absorption (Figure 1.8), we see that because of the interference, the resulting curve is not so simple to analyze. There are many complications that enter in the analysis of the EXAFS oscillations. I will not examine all of them but only the major ones in order to evaluate the advantages and limitations of this method.

- The general treatment of photoabsorption is a one-electron approximation. It neglects, among other phenomena, the effect on the core of the excitation of the photoelectron. While the electron is excited, one can expect that the core will react differently, altering the cross-section and thus the EXAFS. Although this effect is somewhat taken care of by using the eigenfunctions of the  $Z+1$  atom (reflecting the presence of one core hole), all the details have not yet been worked out.
- A substantial simplification of the equations for EXAFS results from the neglect of multiple-atom scattering, with the consideration of only short-

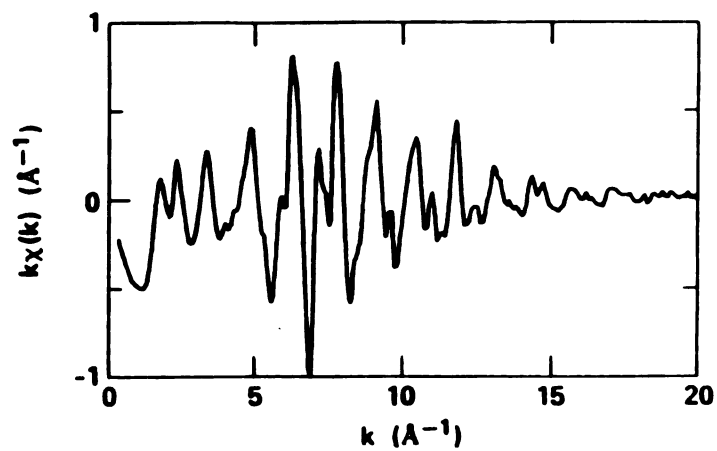


Figure 1.7: The EXAFS oscillations pass the K-shell absorption edge in Cu (Hayes and Boyce, 1982)

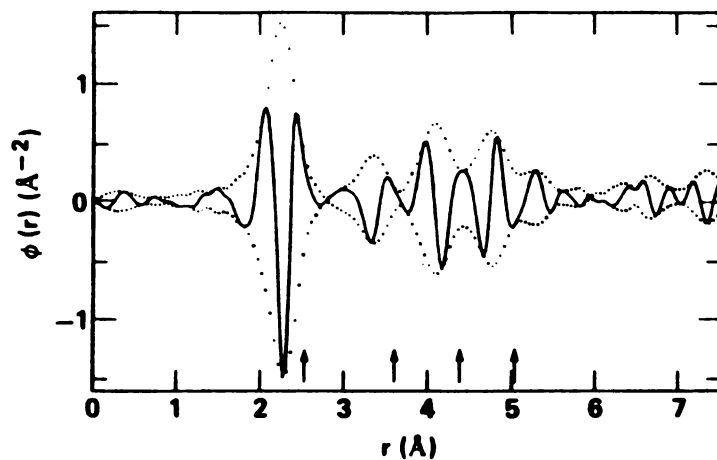


Figure 1.8: The real part and the magnitude of the Fourier transform of the EXAFS signal for Cu (solid and dotted line, respectively). The near-neighbor distances in Cu are indicated by vertical arrows (Hayes and Boyce, 1982).

range order. It is surely one of the main advantage of EXAFS over LEED where one must solve the full Schrödinger equation. However, comparisons of the theory with experimental results in Zn chalcogenides has shown that the inclusion of the multiple-atom scattering is sometimes necessary.

- In order to compare the theory and the data, it is necessary to establish two independent variables: the phase-shift  $k$  of the outgoing electron wave due to the excited atom from the calculations and the x-ray photon energy  $\hbar\omega$  from the experiment. These two variables are related by the final state electron energy

$$\begin{aligned} E &= E_{\alpha, nl} + \hbar\omega \\ &= E_0 + \frac{\hbar^2 k^2}{2m}. \end{aligned} \tag{1.7}$$

The correspondence depends on an accurate evaluation of  $E_{\alpha, nl} - E_0$ ; a task which is almost impossible in practice due to the simple models used for the interaction  $V_0$ . When comparing systems that are very similar, it is only required that the difference between the assumed  $E_0$  and its real value be the same for all the cases.  $E_0$  is then considered as a fitting parameter for one known system and checked for consistency in the other materials. However, this approximation creates a problem when one wants to compare very different materials.

The general method used to interpret EXAFS results is to compare a model with the experimental data and to extract the structural information from the fitted parameters. Since the measurement itself is relatively straightforward, the obvious limitations of EXAFS lie in the model used for fitting the data. Although the present models can work very well for disordered samples that are

electronically close to a known structure, its precision is not so good when there is no known structure close to the one observed. In order to clarify many important details of the local structure of disordered systems, EXAFS remains an excellent tool. However, there is still a need for more complete models that would increase the accuracy of EXAFS to a fraction of a hundredth of Å so that it can serve as an accurate test for the theories solving problems with this precision.

## 1.5 Conclusion

In the next chapters, I will present some results that will help in understanding the specific role of size mismatch in disordered systems: solid solutions on a crystalline and amorphous lattice. It is rather surprising that even for simple alloys, the local structure has not been understood much earlier since all the theoretical tools were available. After explaining in some details the general theory developed by Thorpe, Jin and Mahanti (1989), Thorpe and Garboczi (1990) and Cai and Thorpe (1992a, 1992b), I look at the deviations from this theory in the case of metallic alloys, where the concept of natural size, introduced by Pauling, does not apply very well. Then the theory is checked for SiGe crystalline and amorphous alloys. Although the crystalline alloys are not really a challenge, the study of the effect of amorphisation versus size-mismatch on the structure gave us a better understanding of the strength of this simple topological model. However straightforward the theoretical results for the SiGe alloys are, they do not agree very well with a series of EXAFS experiments on both amorphous and crystalline structure. The following chapter examines the disagreement and looks at whether the theory or the experiment fails. One method to determine whether the experiment or the theory is incomplete or wrong in the case of these alloys is to use a different probe

to look at the structure. Chapter 6 extends the Cai and Thorpe theory to the surface of SiGe alloys, making predictions that can be checked against scanning tunneling microscope measurements that are more direct than EXAFS. A confirmation of the theoretical results on atomic positions at the surface would indicate strongly that the theory is also valid in the bulk. Finally, I examine the effect of size-mismatch on a two-dimensional lattice. Many claims have been made in the last decade and a half about the solid-liquid transition in these systems. In the hope of improving the understanding of this transition, I have performed some simulations, increasing the disorder with size-mismatch instead of temperature. Although not a perfect mapping, the size-mismatch technique has the advantage of being a static study, allowing us to get much closer to the phase transition without having to care about the divergence in the fluctuations.

# Chapter 2

## Theory

The development of the general theory of mismatch alloys was performed over many years by M. F. Thorpe, S. D. Mahanti and their collaborators. They began to study this problem in the context of intercalation compounds, trying to predict what kind of deformation the intercalant would suffer under the pressure of the intercalated layers and its neighbors (Thorpe, Jin and Mahanti, 1989). From one-dimension, the problem was extended to two and three dimensions for both bond and site mismatch.

This chapter presents the general theory for the bond-mismatch problem with only nearest-neighbor interactions since the formalism is simpler. I will then only state the corresponding results for site-mismatch disorder without proof and describe briefly the derivation in the case of a two- and three-body potential, that I will present in more details in chapter 4 and following.

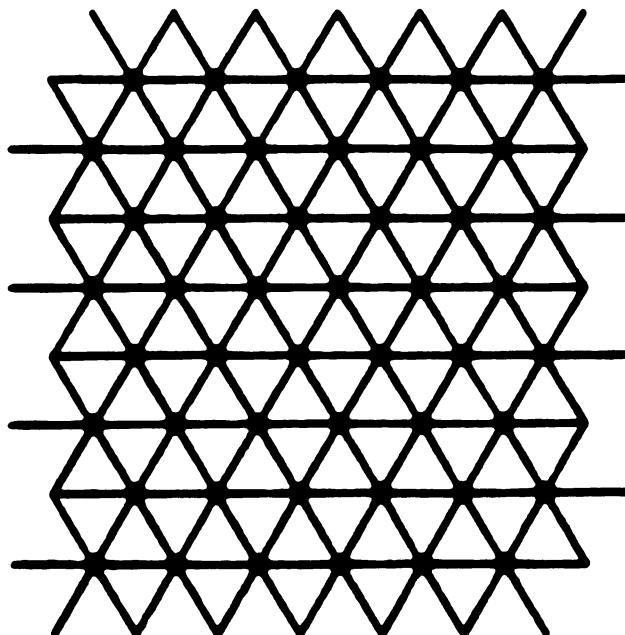


Figure 2.1: A triangular network (Thorpe and Garboczi, 1990)

## 2.1 Bond mismatch

For simplicity, I will consider a two dimensional triangular network, which is equivalent to a face-centered cubic network in three dimensions (Figure 2.1). The following derivation is taken from Thorpe and Garboczi (1990).

On this network, one distributes at random bonds of natural length  $L_A^0$  and  $L_B^0$  (Figure 2.2) with probability  $1 - x$  and  $x$  respectively. Each of these bonds is a Hooke's spring so the total energy is given by

$$V = \frac{1}{2} \sum_{\langle ij \rangle} K_{ij} (L_{ij} - L_{ij}^0)^2, \quad (2.1)$$

where  $\langle ij \rangle$  signifies that the contribution of each bond is counted only once, and the average length, by

$$\langle L \rangle = (1 - x) \langle L_A \rangle + x \langle L_B \rangle. \quad (2.2)$$

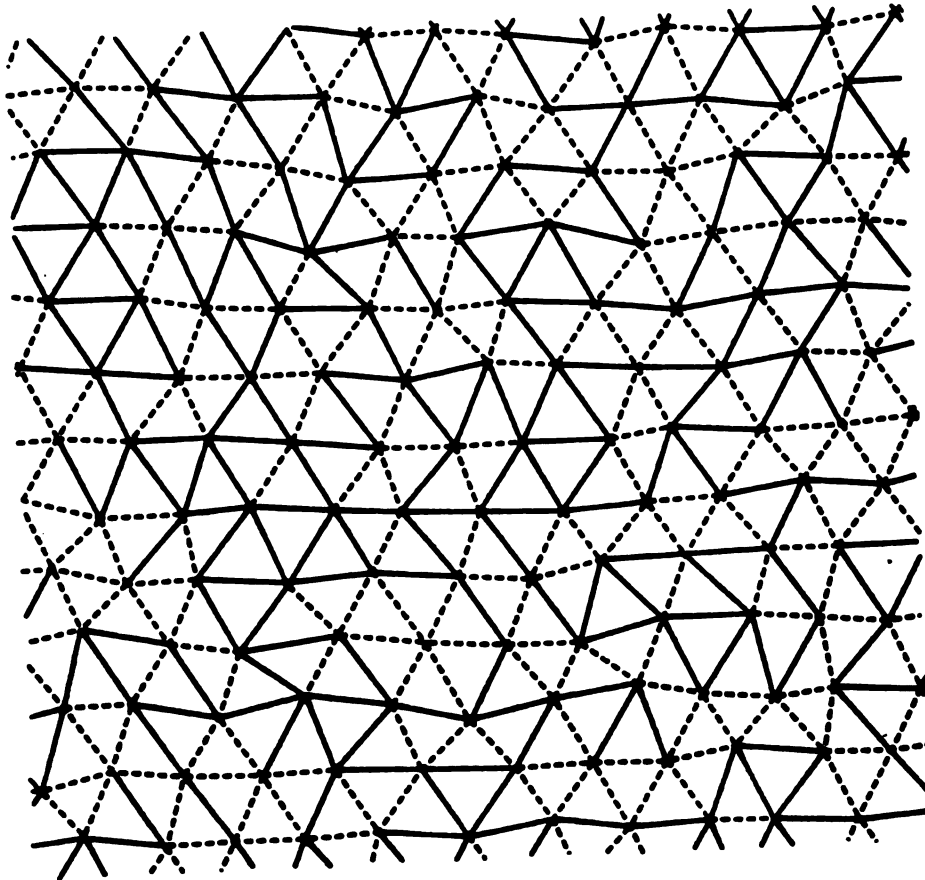


Figure 2.2: Relaxed triangular network where two sizes of bonds have been distributed randomly (Thorpe and Garboczi, 1990).

The only requirement for equilibrium is that the force on each bond vanishes. So, minimizing the energy with respect to  $i$ , we obtain

$$0 = \sum_j K_{ij} [(\mathbf{R}_i - \mathbf{R}_j) - L_{ij}^0 \hat{\mathbf{R}}_{ij}], \quad (2.3)$$

with  $\hat{\mathbf{R}}_{ij}$  the unit vector from  $\mathbf{R}_i$  to  $\mathbf{R}_j$ . Since this equation is linear, we can rewrite it as a weighted sum of the average lengths. If we suppose that displacements from the perfect triangular network are small, then all displacements are along the bond and the previous equation becomes

$$0 = (1 - x)K_A(\langle L_A \rangle - L_A^0) + xK_B(\langle L_B \rangle - L_B^0). \quad (2.4)$$

It is equivalent to say that if we draw any line cutting a plane of bonds, the sum of all tensions must be zero. If we put  $K_A = K_B = K$ ,

$$\langle L \rangle = (1 - x)\langle L_A \rangle + x\langle L_B \rangle = (1 - x)L_A^0 + xL_B^0, \quad (2.5)$$

which is simply the Végard's law (Végard, 1921), proposed for alloys more than 70 years ago. Note that this relation is *exact* for any disorder as long as all elastic constants are the same for all interactions. I will return to the problem where there is more than one elastic constant in the next section but until then, I keep this requirement.

The next problem is to find the average partial lengths  $\langle L_A \rangle$  and  $\langle L_B \rangle$  in the alloys. We start by expressing a particular bond length as

$$\mathbf{L} = \mathbf{R}_i - \mathbf{R}_j = \mathbf{L} + [(\mathbf{u}_i - \mathbf{u}_j) \cdot \hat{\mathbf{R}}_{ij}] \hat{\mathbf{R}}_{ij}, \quad (2.6)$$

where  $\mathbf{u}_j$  is a small displacement and  $\hat{\mathbf{R}}_{ij}$  is a unit vector along an undistorted bond. Replacing this definition in Equation (2.3), it becomes

$$0 = K \sum_i [(\mathbf{u}_i - \mathbf{u}_j) \cdot \hat{\mathbf{R}}_{ij} - (\langle L \rangle - L_{ij}^0)] \hat{\mathbf{R}}_{ij}. \quad (2.7)$$

This equation can be expressed in terms of the dynamical matrix  $D_{ij}$

$$D_{ij}^{\alpha\beta} u_j^\beta = v_i^\alpha, \quad (2.8)$$

where I follow the Einstein's summation index convention and

$$v_i^\alpha = K \sum_j (L_{ij}^0 - \langle L \rangle) \cdot \hat{R}_{ij}^\alpha. \quad (2.9)$$

Inverting Equation (2.8),

$$u_i^\alpha = -G_{ij}^{\alpha\beta} v_j^\beta \quad (2.10)$$

with  $G$ , the Green's function for the perfect triangular lattice. Inserting 2.10 and 2.9 in 2.6,

$$\begin{aligned} L_{ij} &= \langle L \rangle + K \sum_{lm} [\hat{R}_{ij} \cdot (\mathbf{G}_{im} - \mathbf{G}_{jm}) \cdot \hat{R}_{lm}] (L_{lm}^0 - \langle L \rangle) \\ &= \langle L \rangle + 2K \sum_{lm} (\hat{R}_{ij} \cdot \mathbf{G}_{im} \cdot \hat{R}_{lm}) L_{lm}^0, \end{aligned} \quad (2.11)$$

where I used the identity

$$\sum_j \hat{R}_{ij} = 0. \quad (2.12)$$

Equation (2.12) gives the actual length of one particular bond as a function of all the natural lengths. By averaging over all the bonds we obtain an identity. One can find the average partial lengths using a bond variable  $\sigma_{ij}$  equal to plus (minus) 1 when the bond is of type A (B). The average value of this quantity is

$$\langle \sigma_{ij} \rangle = 1 - 2x. \quad (2.13)$$

Using a projection operator on the bond type A

$$\frac{1 + \sigma_{ij}}{4N(1 - x)} \quad (2.14)$$

and re-expressing the natural length as an operator

$$L_{lm}^0 = \frac{1}{2}(L_A^0 + L_B^0) + \frac{\sigma_{lm}}{2}(L_A^0 - L_B^0), \quad (2.15)$$

it becomes

$$\begin{aligned} \langle L_A \rangle = \langle L \rangle &+ \frac{K}{4N(1-x)} \sum_{ijlm} \langle (1 + \sigma_{ij})(1 + \sigma_{lm}) \rangle \\ &\times (\hat{\mathbf{R}}_{ij} \cdot G_{im} \cdot \hat{\mathbf{R}}_{lm})(L_A^0 - L_B^0). \end{aligned} \quad (2.16)$$

Defining

$$a^*(x) = \frac{K}{4Nx(1-x)} \sum_{ijlm} \langle \sigma_{ij}\sigma_{lm} \rangle (\hat{\mathbf{R}}_{ij} \cdot G_{im} \cdot \hat{\mathbf{R}}_{lm}), \quad (2.17)$$

Equation (2.17) becomes simply

$$\langle L_A \rangle = \langle L \rangle + xa^*(x)(L_A^0 - L_B^0) \quad (2.18)$$

and, similarly,

$$\langle L_B \rangle = \langle L \rangle - (1-x)a^*(x)(L_A^0 - L_B^0). \quad (2.19)$$

Now, let's take a closer look at  $a^*(x)$ . If the bonds are distributed randomly on the lattice, the pair-correlation function becomes

$$\langle \sigma_{ij}\sigma_{lm} \rangle - \langle \sigma_{ij} \rangle \langle \sigma_{lm} \rangle = 4x(1-x)\delta_{ij,lm}. \quad (2.20)$$

So Equation (2.17) is no longer  $x$  dependent

$$\begin{aligned} a^* &= 2K [\hat{\mathbf{R}}_{ij} \cdot (G_{ij} - G_{ii}) \cdot \hat{\mathbf{R}}_{ij}] \\ &= 2d/z \\ &= \frac{2}{3}, \end{aligned} \quad (2.21)$$

where  $ij$  is a nearest-neighbor bond,  $d$ , the dimensionality of the network and  $z$ , the coordination number. This result was first found by Feng, Thorpe and Garboczi (1985) in the context of rigidity percolation.

It is also possible to obtain the fluctuations of the bond lengths. One can calculate directly by squaring Equation (2.17). In the random distribution limit,

we find that all the distributions are identical, and have widths

$$\begin{aligned} \langle L_A^{02} \rangle - \langle L_A^0 \rangle^2 &= \langle L_B^{02} \rangle - \langle L_B^0 \rangle^2 \\ &= x(1-x)a^*(1-a^*)(L_A^0 - L_B^0)^2. \end{aligned} \quad (2.22)$$

This result is not as surprising as it may appear. It simply represents the local nature of the relaxation. Since no bond *knows* the total concentration for *A* and *B* bonds on the lattice, on a local scale, bonds from different species see identical configurations and hence have similar distributions. Finally, one can obtain the total strain energy of the bond-mismatched lattice by the back door, using the Feynman-Hellman theorem (Feynman (1939))

$$\frac{\delta}{\delta p} \langle \epsilon(p) \rangle = \left\langle \frac{\delta \epsilon(p)}{\delta p} \right\rangle. \quad (2.23)$$

where  $\epsilon$  is the energy density. From Equation (2.17), we see that only the natural lengths enter in the average bond energy which we can express as

$$\langle \epsilon \rangle = AL_A^{02} + BL_B^{02} + CL_A^0 L_B^0. \quad (2.24)$$

The derivative with respect to  $L_A^0$  gives

$$\frac{\delta \langle \epsilon \rangle}{\delta L_A^0} = 2AL_A^0 + CL_B^0. \quad (2.25)$$

Comparing this result with

$$\left\langle \frac{\delta \epsilon}{\delta L_A^0} \right\rangle = K(\langle L_A \rangle - L_A^0), \quad (2.26)$$

and using similar equations for  $L_B^0$ , one finds easily that the average bond energy is

$$\epsilon = \frac{1}{2}x(1-x)a^*(L_A^0 - L_B^0)^2. \quad (2.27)$$

All these results are shown in Figure 2.3 with a comparison between theory and computer simulations. In all cases, the agreement turns out to be excellent.

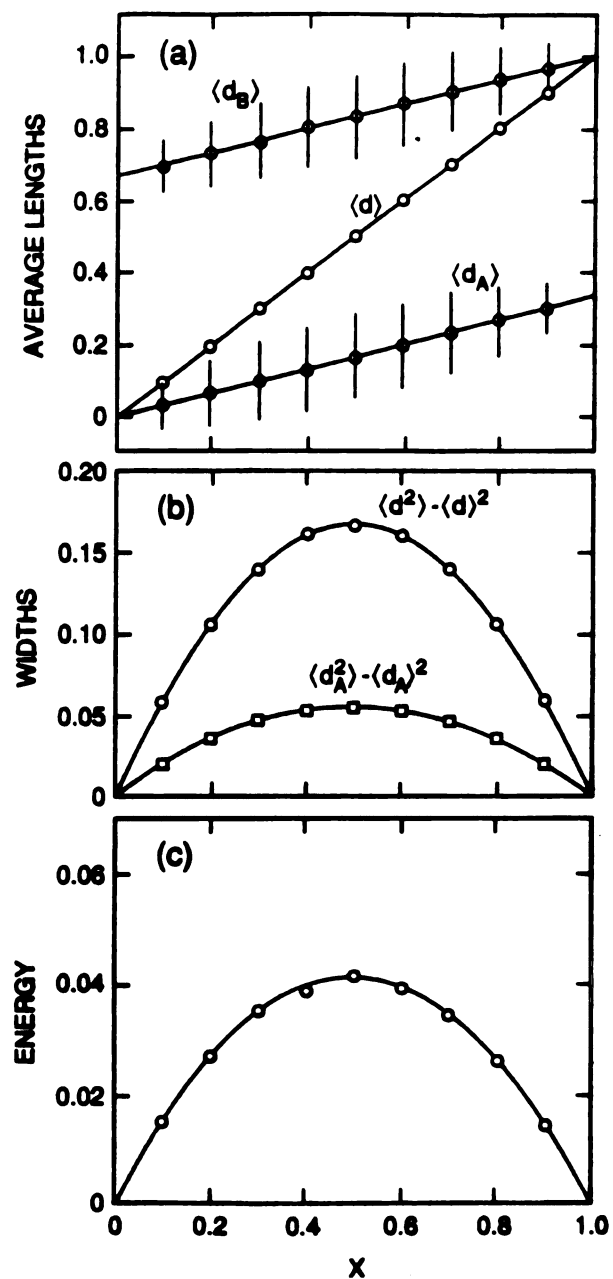


Figure 2.3: Variation of the configurational energy, the width of the partial length distribution and the partial lengths as a function of concentration  $x$  in bond alloy  $A_{1-x}B_x$ . The  $d$ 's are renormalized lengths such that the topological rigidity  $a^*$  is given by the difference  $\langle d_B \rangle - \langle d_A \rangle$  (Thorpe and Garboczi, 1990).

## 2.2 Force constant disorder

The first condition put on the pair potential was to demand that all the force constants be the same. This limitation comes from the form of Equation (2.8). We know how to solve this equation exactly only when the disorder is limited to the vector  $\mathbf{v}$ , on the right hand side, not in the dynamical matrix itself. It is, however, possible to develop an effective-medium theory that will allow a certain understanding of the role of the force-constant disorder in changing the exact solutions presented before. Since I will discuss this problem with more details in chapter 3, I will only add that the main effect of this disorder is to slightly curve the straight lines of the  $Z$ -plot as can be seen in Figure 2.4. In the case of bond disorder, the effective medium theory does a very outstanding job in predicting the correct curvature. Also, the curvature is noticeable only when the difference between the force constants is large ( $K_A = 2K_B$  in Figure 2.4). When the two force constants vary only by 10 or 20 percent, the lines are straight enough that we do not need to bother with this effect given current experimental accuracy.

## 2.3 Site-mismatch

For the site-mismatch problem, the solution is almost the same although the analytical part is a little more difficult. Instead of two partial lengths, there are three. Defining the average length as

$$\langle L \rangle = (1-x)^2 L_{AA}^0 + 2x(1-x)L_{AB}^0 + x^2 L_{BB}^0, \quad (2.28)$$

Chen and Thorpe (1992) have shown that

$$\langle L_{AA} \rangle = \langle L \rangle + a^* x^2 \Delta - x a^{**} [L_{BB}^0 - L_{AA}^0 + (2x-1)\Delta], \quad (2.29)$$

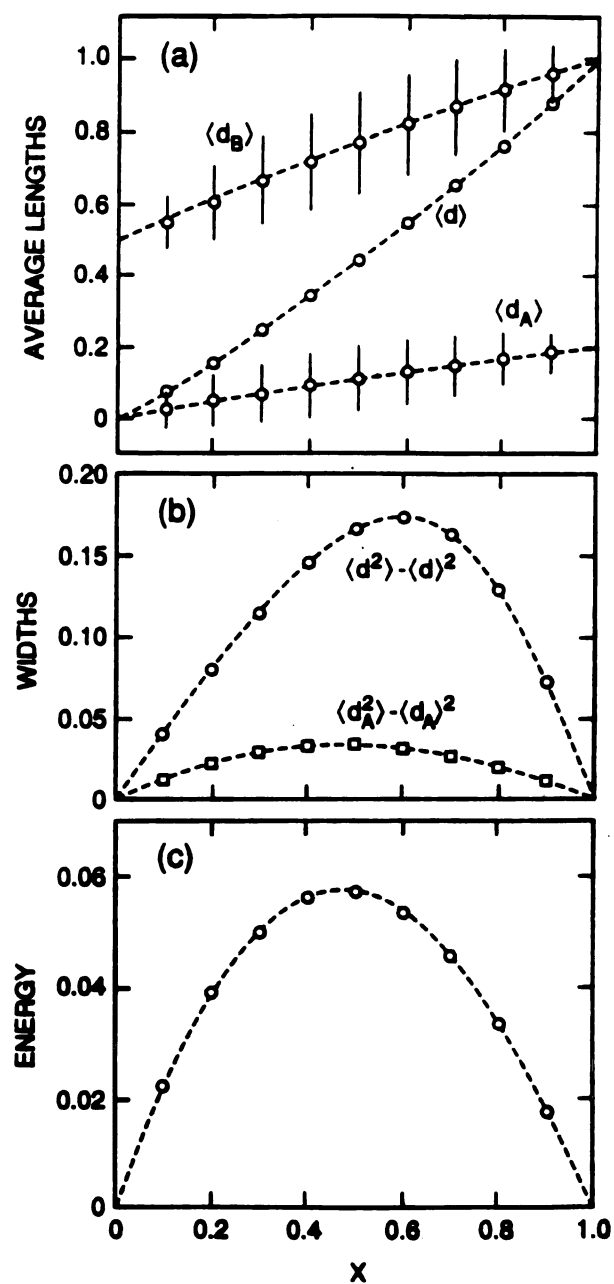


Figure 2.4: Variation of the configurational energy, the width of the partial length distribution and the partial lengths as a function of concentration  $x$  in bond alloy  $A_{1-x}B_x$  and  $K_A = 2K_B$ . The  $d$ 's are renormalized lengths (Thorpe and Garboczi, 1990).

$$\begin{aligned}\langle L_{BB} \rangle &= \langle L \rangle + a^*(1-x)^2\Delta + (1-x)a^{**} [L_{BB}^0 - L_{AA}^0 + (2x-1)\Delta], \\ \langle L_{AB} \rangle &= \langle L \rangle + a^*x(1-x)\Delta - (x-1/2)a^{**} [L_{BB}^0 - L_{AA}^0 + (2x-1)\Delta],\end{aligned}$$

where

$$\Delta = L_{BB}^0 + L_{AA}^0 - 2L_{AB}^0 \quad (2.30)$$

and

$$a^{**} = \frac{K}{16Nx(1-x)} \sum_{ijm} \langle (1+\sigma_i)(1+\sigma_j)(\sigma_l+\sigma_m) \rangle \hat{\mathbf{R}}_{ij} \cdot \mathbf{G}_{im} \cdot \hat{\mathbf{R}}_{lm}. \quad (2.31)$$

The energy density is

$$\begin{aligned}E &= \frac{1}{4}Kx(1-x) \left\{ (1-a^{**}) [1 + \delta(1+2x-1)]^2 \right. \\ &\quad \left. + 2(1-a^*)\delta^2x(1-x) \right\} (L_{BB}^0 - L_{AA}^0)^2,\end{aligned} \quad (2.32)$$

with

$$\delta = \frac{\Delta}{(L_{BB}^0 - L_{AA}^0)}. \quad (2.33)$$

However, the computation of the partial length fluctuations become extremely difficult unless one sets  $\Delta = 0$ , which corresponds to defining  $L_{AB}^0$  as the arithmetic average of the two other lengths. In this case,

$$\begin{aligned}\langle L_{AA}^2 \rangle - \langle L_{AA} \rangle^2 &= \langle L_{BB}^2 \rangle - \langle L_{BB} \rangle^2 \\ &= \langle L_{AB}^2 \rangle - \langle L_{AB} \rangle^2 \\ &= \frac{1}{2}x(1-x)a^{**}(1-a^{**}).\end{aligned} \quad (2.34)$$

Again, and for the reason given before, all the distributions are identical.

## 2.4 $a^*$ and $a^{**}$

In the two previous section, we have encountered two parameters:  $a^*$  and  $a^{**}$ . The first one appears in the bond-mismatch problem and the second one in the

site-mismatch problem —alone if  $L_{AB} = (L_{AA} + L_{BB})/2$ . The knowledge of their value gives a complete understanding of all quantities presented before and some more that I will discuss in the next section. In order to understand the meaning of these parameters, let's take a look at Equations (2.17) and (2.31). We first see that there is no disorder included in their definition. Both parameters depend only on the Green's function of the perfect crystal. Since their value reflects the topology of the system, they are called *topological constants*. Note also that the summation is only on the nearest-neighbors and so its value reflects the *local* connectivity of the lattice.

Even if Equations (2.17) and (2.31) define completely the two topological parameters, it is useful to describe them in a more physical fashion. As mentioned previously,  $a^*$  was previously introduced by Feng *et al.* (1985) when solving a topological rigidity problem. In that paper, the authors obtained the topological parameter by calculating the force needed to pull on a bond with force constant  $K$  but inserted in a lattice. Obviously, this force will be greater than if there was no lattice. It can be described as

$$F = \frac{K}{a^*}u \quad (2.35)$$

where  $u$  is the displacement from the equilibrium value of the bond. When  $a^* = 1$ , it is as if the network was non-existent or floppy. The other limit, extreme rigidity, is achieved for  $a^* = 0$ , where only an infinite force can produce a finite displacement.

Similarly, one can obtain a physical meaning for  $a^{**}$ . In this case, it represents the response of the lattice to trying to open up a cage in order to introduce a larger atom. Figure 2.5 gives a physical representation of the topological parameters. This simple picture works well for bulk alloys. However, it needs

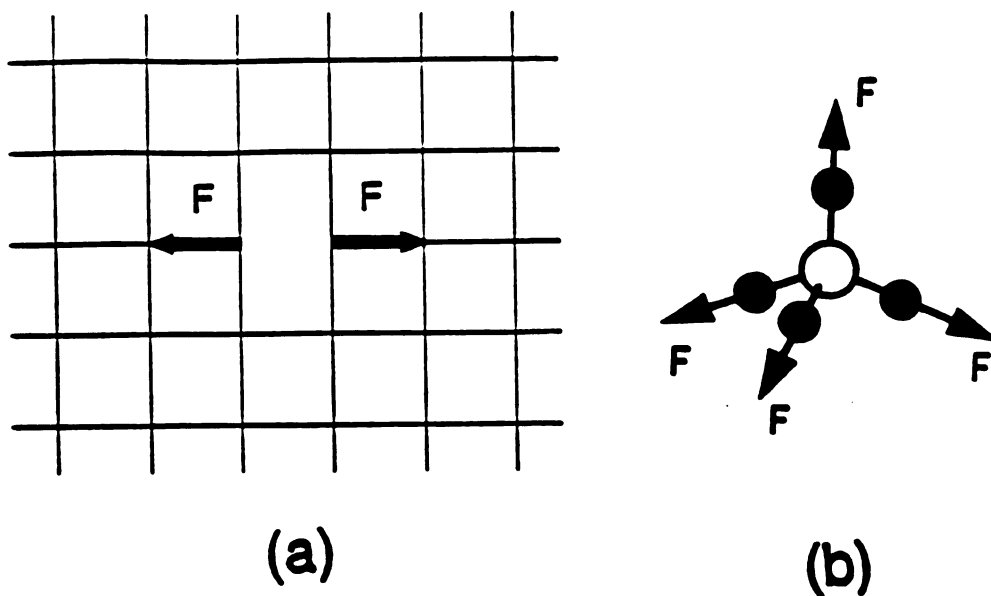


Figure 2.5: Physical representation of the topological rigidity parameters. (a)  $a^*$ ; (b)  $a^{**}$ .

some refinements when one looks at the surface as we will see in chapter 6. From the definition 2.17 for  $a^*$ , for a two-body potential, the more neighbors an atom has, the more rigid is the lattice locally. This relation also applies for  $a^{**}$ . For an unstable lattice, the previous equation is invalid and the topological rigidity parameters are simply 1.

Finally, in many instances, especially those involving angular terms, it is simpler to measure directly the topological rigidity parameter from the  $Z$ -plot, i.e. from the average partial lengths as a function of concentration. From Equation (2.17), one easily sees that by taking the mismatch  $L_B^0 - L_A^0$  as the unit length, then the distance between the two partial lengths is  $a^*$ , for bond mismatch and  $a^{**}$  for site-mismatch with  $\Delta = 0$ .

## 2.5 Semiconductors

In the case of a semiconductor, it is imperative to include an angular term in the potential in order to stabilize the lattice. The Kirkwood potential is preferred over the more usual Keating potential since Kirkwood separates completely the angular term from the stretching term,

$$V = \frac{\alpha}{2} \sum_{\langle ij \rangle} (L_{ij} - L_{ij}^0)^2 + \frac{\beta}{8} L_e^2 \sum_{\langle ijk \rangle} \left( \cos \theta_{ijk} + \frac{1}{3} \right). \quad (2.36)$$

Here, the two force constants  $\alpha$  and  $\beta$  have the same dimension while  $L_e$  is the average length in the system. Using again the first order approximation in the displacement from equilibrium as given by eq. 2.6, it is possible to express the potential energy in a quadratic form

$$V = \frac{1}{2} \mathbf{u}^+ \mathbf{M} \mathbf{u} + \mathbf{u}^+ \Phi + E_0 \quad (2.37)$$

where  $\mathbf{u}$  is the vector displacement from the equilibrium position,  $\mathbf{M}$  is the connectivity matrix and  $\Phi$  contains the internal strain due to disorder. The derivative of this equation with respect to  $\mathbf{u}$  gives us an equation with the same form as Equation (2.8) and hence, can be solved exactly. Cai and Thorpe (1992a) obtained a complete solution for quaternary semiconductors.

In chapter 4, I will present the binary case that is a special case of the general solution. However, a few details should be pointed out here. First, the topological parameters are function of the ratio of the angular force constant to the stretching force constant,  $\beta/\alpha$ . For a zero angular force, the diamond lattice is completely floppy and therefore unstable. The typical range of this ratio, for semiconductors, is between 0.1 and 0.2 with the notable exception of diamond where the ratio is more like 0.6. Second, the solution found by Cai

and Thorpe includes the complete first- and second-neighbor distances for all the partial lengths. For the second-neighbor bond length a new topological parameter is introduced

$$b^{**}(\beta/\alpha) = \alpha \sqrt{\frac{8}{3}} \sum_{j'} G_{i\vec{i}', i\vec{j}'}, \quad (2.38)$$

where  $j'$  is a first neighbor of  $i$  while  $i'$  is one of its next-nearest neighbors. The physical significance of this parameter is related to the opening of the shell associated with the second neighbors. Although, there is no formal relation between  $a^{**}$  and  $b^{**}$ , it has been found numerically that for most of the range of the values  $\beta/\alpha$

$$b^{**} = \frac{a^{**}}{2}. \quad (2.39)$$

Figure 2.6 shows these two topological parameters as a function of the ratio of force constants. Since the edge of the curve on this figure has a large uncertainty, one can not rule out that this relation holds everywhere. We have not been able, however, to provide a formal proof or a physical argument supporting this relation. Nevertheless, since it works numerically, it is possible to use it in order to simplify the second-neighbor equations.

## 2.6 Correlation

It is possible to include correlation effects through the topological constants. Going back to the definition of, say  $a^*$ , the correlation can be included in  $\langle \sigma_{ij} \sigma_{lm} \rangle$ . Thorpe and Garboczi (1990) and Chen and Thorpe (1992) studied correlated systems for bond and site mismatch respectively. This problem is very difficult to solve analytically in all cases except for a handful of special functions.

Using a scheme forcing clustering for the first neighbor interaction, Thorpe

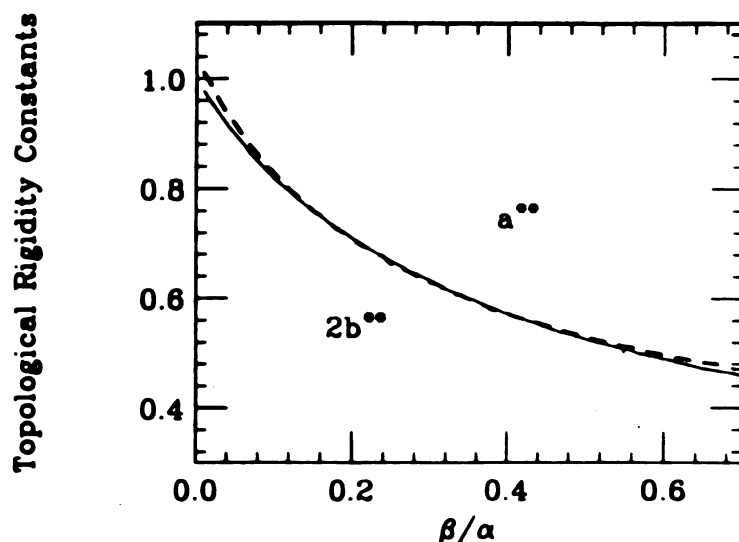


Figure 2.6: The topological rigidity  $a^{**}$  and  $2b^{**}$ , dash and solid line respectively. This data is from a numerical calculation (Cai and Thorpe, 1992a).

and

Garboczi(1990) obtained the results shown in Figure 2.7. In spite of clustering, one could easily fit a straight line through the simulation and conclude that there is no correlation. Because of this, it would be useful to be able to introduce correlation only when the experimental results are precise enough to distinguish between correlated and uncorrelated alloys.

## 2.7 Conclusion

The general theory of mismatched alloys developed during the last five years present a very useful scheme in order to understand the meaning and significance of recent experimental measurements. Although an exact solution is obtainable only in certain limits, it is possible to solve it numerically in more complex situations.

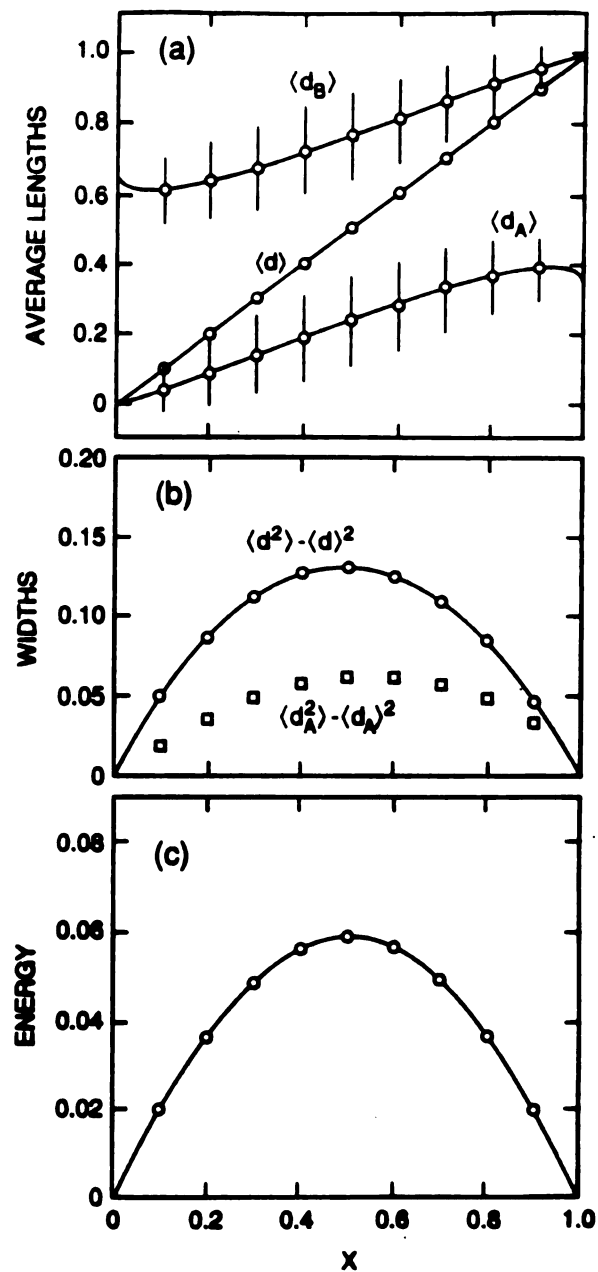


Figure 2.7: Variation of the configurational energy, the width of the partial length distribution and the partial lengths as a function of concentration  $x$  in bond alloy  $A_{1-x}B_x$ . A positive correlation term has been added. The  $d$ 's are renormalized lengths (Thorpe and Garboczi, 1990).

The physical content of the equations is simple and robust since the problem involves only the topology and connectivity of the pure crystal.

It would be feasible to add complexity to the equations by adding force constant disorder and correlation but, as shown here, this does not lead to important changes in the answers but, especially in the latter case, demands a much higher knowledge of the local order that we actually have for most alloys at present.

## Chapter 3

# Metallic Alloys

In the last few years, the problem of length mismatch in alloys has received considerable attention both theoretically and experimentally. As I discussed in the previous chapter, Thorpe and Garboczi (1990) have recently solved this problem analytically for alloys with equal harmonic spring interactions between nearest-neighbor atoms, joined by bonds with different natural lengths. Experimentally, the development of extended x-ray absorption fine-structure spectroscopy (EXAFS) has provided more information concerning the near-neighbor lengths in alloys. These partial lengths are of primary importance for a proper structural characterization and in understanding of the deviations from Végard's law.

From this point of view, the study of fcc binary metallic alloys is very interesting since for these compounds, the deviations from Végard's law are much more significant than for example in semiconductors, as we will see in the next chapter. The development of the embedded-atom-method (EAM) potentials (Daw and Baskes, 1984, and Finnis and Sinclair, 1984) which have given reliable results for the energies of pure metals, with and without impurities, and binary alloys (Daw and Baskes, 1984 and Foiles 1985), makes it possible to take into account, in a

simple way, some of the electronic effects. The EAM potentials are, in general, fast to compute, allowing the use of very large supercells, which is important when trying to extract statistical information from random alloys. The version chosen for the present study is the Johnson EAM potential (Johnson, 1988, 1989, 1990), developed recently and possessing two major advantages over other EAM potentials for this study: 1) it is completely analytic and 2) it requires *no additional parameters* for the alloy once the parameters for the pure metals are fixed. The lack of additional alloy parameters has ultimately proved to be a problem, as there are no adjustable parameters to fit experiment. In this chapter, I show that the Johnson EAM potentials are remarkably good in some cases (e.g.  $\text{Ni}_x\text{Au}_{1-x}$ ) but quite unsatisfactory in others (e.g. alloys containing Pt).

Deviations from Végard's Law for metallic alloys have been known since the beginning of x-ray measurements more than sixty years ago. Until recently, however, Végard's Law was actually nothing more than an *ad hoc* assumption (Végard, 1921), but it has been shown that Végard's Law is to be expected only in those cases where there is length mismatch accompanied by *no* changes in the force constants (Thorpe 1990). As these conditions never occur in reality, the discussion must always be about the magnitude and sign of the deviations from Végard's Law. These deviations are small in semiconductors, but can be much larger in metals. As discussed in the introduction, during the fifties, a few models were proposed to quantify these deviations (Fournet, 1953 and Friedel, 1955), but they all started with the assumption that the solid solution forms a perfect network i.e., all the lengths are identical.

In this chapter, I present computer simulation results from the EAM potential. I also present both analytic and computer simulation results from a much

simpler spring model. This central force model (CFM) uses only nearest-neighbor central forces between an atom and its 12 neighbors. It has the virtue that it can be solved analytically in some cases, and can be used in conjunction with the EAM results to assess the sensitivity of the results to the local environment. The CFM is completely independent of the local configuration and incorporates the transferability of the force constants for a particular type of bond for all environments. On the other hand the EAM effectively modifies the force constants of a particular bond in response to the local environment around that bond. This is accomplished via the embedding function. I shall refer to this effect as *electronic density effects* in the rest of this chapter. I show that the EAM potential gives results in reasonable agreement (better than CFM) with experiment for most of the binary alloys composed of Ag, Au, Cu, Ni and Pd while alloys containing Pt all deviate strongly from the EAM results. In this work, I use EAM to refer to the Johnson EAM, and note that other versions of the EAM for alloys may well give different results. Surprisingly, CFM gives good agreement with experimental diffraction data for the NiCu, PdAg and all Pt alloys. These results suppose, as we shall see in Sec. 3.4, that the electronic density effect is least important for alloys containing Pt where one can treat the atoms as rigid objects connected by elastic springs. I also present some analytic and computer results for the bond-length distributions in alloys. The general features of these distribution are not, in general, very sensitive to the particular model since they depend on topological quantities like the number of nearest neighbors and are found to be remarkably wide, of the order of the length mismatch itself.

Another quantity of interest is the variation of the elastic constants with concentration. I have computed the bulk and shear moduli and found that these

quantities are also rather insensitive to the model used. In particular, both the EAM and the CFM show very similar results for the bulk modulus. As there exists almost no experimental data for the elastic moduli in bulk alloys, the results I present here must be considered as predictions to be confirmed or otherwise by future experiments.

### 3.1 Embedded-atom method

The embedded-atom method was first proposed by Daw and Baskes (1983, 1984) and was based on the quasiatome or effective medium theory (Stott and Zaremba, 1980). In the quasiatome theory, an impurity interacts with a local and almost uniform environment. We can describe the energy as

$$E_{quas} = E_Z(\rho_h(R)) \quad (3.1)$$

with  $E_Z$  the quasiatome energy of an impurity with atomic number  $Z$  at site  $R$  for a host electronic density  $\rho_h$ . One can of course add an elastic deformation term  $E_{lat}$  to take into account the lattice deformation but this technique can only study single and well-defined impurities, not cracks nor surfaces. Daw and Baskes extended this formalism to treat *all* atoms as impurities embedded in the host consisting of the other atoms. Therefore, using simple energetics, it became possible to go much beyond the pair potential without a significant increase in the efforts. At the same time, Finnis and Sinclair (1984) introduced a tight-binding model that turned out to be completely equivalent mathematically to the Daw and Baskes model; only the physical interpretation differs. Since these potentials are empirical, this difference leads to no consequence.

Before discussing further the details of the potential, I want to mention

a few points. The use of a general EAM potential for alloys commands that the function describing the atom and its reaction to the local electronic density be the same for all metallic species involved in the calculation. Recently, Jones (1990) has shown that in general the results for alloys are less accurate with such potential rather than with one expressly developed for that particular alloys. However, when the need comes to compare many different alloys, the EAM remains the most sophisticated method for the study of large scale statistics. In retrospect, the EAM potential is based on the two following approximations:

1. The assumption is made that the charge density of each atom is not changed from the isolated atom density.
2. The background charge density into which the atom is placed is assumed to be adequately represented by the value *at* the nucleus of the atom.

However these approximations are not as crude as they may sound since the potential is largely empirical. Moreover, that the EAM potential has proven to be very accurate in many different situations.

As I already mentioned, the Johnson (1989) version of the EAM potential was used for the simulations, and I will summarize it below. In EAM, the electron-density functions are only determined to within a scaling factor. For pure metals, this factor rescales the embedding function. But the situation is very different in alloys where the relation between the electron density of the two components strongly affects the mixing energies (Foiles, 1985). The interest in the Johnson potential is that it is completely analytic and requires no extra parameter for the alloys. All the parameters are determined using the atomic volume, the cohesive energy, the bulk modulus, the average shear modulus and the vacancy-formation

energy for the pure metals. The approximation used by Johnson is based on the preservation of the invariance of the energy under a gauge transformation involving the embedding function and the pair potential. This choice of constraint is of course as arbitrary as the arithmetic mean used by Foiles (1985), but has the advantage of being fairly *natural* within the EAM formalism. In the notation used by Johnson (1988), the EAM potential is defined by:

$$E_t = \sum_i F^i(\rho_i) + \frac{1}{2} \sum'_{\langle i,j \rangle} \Phi^{ij}(r_{ij}), \rho_i = \sum'_j f^j(r_{ij}), \quad (3.2)$$

where  $E_t$  is the total internal energy,  $\rho_i$  is the total electronic density due to neighbors  $j$  at site  $i$ ,  $F^i(\rho_i)$  is the embedding energy for atom  $i$  and  $\phi(r_{ij})$  is a repulsive ion-ion core pair potential. The prime on the summations indicates that the self terms  $i = j$  are excluded. The functions used in the potential are defined as follows:

$$\Phi^{ij}(r) = \frac{1}{2} \left[ \frac{f^i(r)}{f^j(r)} \phi^j(r) + \frac{f^j(r)}{f^i(r)} \phi^i(r) \right] \quad (3.3)$$

and

$$F^i(\rho) = -E_c^i \left( 1 - \ln \left[ \left( \frac{\rho}{\rho_e^i} \right)^{\alpha'/\beta'} \right] \right) \left( \frac{\rho}{\rho_e^i} \right)^{\alpha'/\beta'} - 6\phi_e^i \left( \frac{\rho}{\rho_e^i} \right)^{\gamma'/\beta'}, \quad (3.4)$$

where

$$f^i(r) = f_e^i \exp \left[ -\beta^i (r/r_e^i - 1) \right] \quad (3.5)$$

and

$$\phi^i(r) = \phi_e^i \exp \left[ -\gamma^i (r/r_e^i - 1) \right]. \quad (3.6)$$

The parameters used in this work are the same as those given by Johnson (1989) and are shown in Table 3.1.

The EAM potential for pure cubic metals is not restricted by the isotropy relation  $C_{11} = 2C_{44} + C_{12}$  of the CFM, which is rarely obeyed in metals. However

Table 3.1: Parameters for the Johnson EAM potential.  $\Omega$  is the atomic volume ( $\text{\AA}^3$ ), only the ratios of the  $f_e$  are relevant and the other parameters are dimensionless.

Atom	$\Omega$	$f_e$	$\phi_e$	$\alpha$	$\beta$	$\gamma$
Cu	11.81	0.30	0.59	5.85	5.85	8.00
Ag	17.10	0.17	0.48	5.92	5.96	8.26
Au	16.98	0.23	0.65	6.37	6.67	8.20
Ni	10.90	0.41	0.74	4.98	6.41	8.86
Pd	14.72	0.27	0.65	6.42	5.91	8.23
Pt	15.06	0.38	0.95	6.44	6.69	8.57

the EAM potential does allow only two independent elastic constants, and as a result imposes the general EAM condition  $C_{11} = C_{44} + C_{12}$  which is reasonably well obeyed for many fcc metals (Jacobsen, 1988). I have found (numerically) that the relation  $C_{11} = C_{44} + C_{12}$  still holds for alloys, so that there are only two, instead of three, independent elastic constants. As the bulk modulus  $B = [C_{11} + 2C_{12}]/3$  and the Voight average shear constant  $G = [3C_{44} + (C_{11} - C_{12})]/5$  are fitted in the EAM potential for the pure metals, I use these as the two independent elastic constants for the alloy.

## 3.2 Central force model

In order to get an idea of the importance of the redistribution of the electronic charges in the alloy, and to gain some perspective on the EAM model, I have compared the results of the EAM potential with a simple nearest-neighbor spring

model (CFM). The total energy for an  $A_{1-x}B_x$  alloy is given by

$$E = \frac{1}{2} \sum_{\langle i,j \rangle} K_{ij} (L_{ij} - L_{ij}^0)^2 \quad (3.7)$$

where the A–A and B–B spring constants and equilibrium lengths are taken from the parameters for the pure metal as given by Johnson (1989), and the additional alloy parameters are chosen to be

$$K_{AB} = \frac{2K_{AA}K_{BB}}{K_{AA} + K_{BB}} \quad (3.8)$$

and the natural (*unstrained*) lengths are

$$L_{AB}^0 = \frac{1}{2} (L_{AA}^0 + L_{BB}^0). \quad (3.9)$$

The angular brackets  $\langle \dots \rangle$  in the summation in Eq. 3.7 indicate that each nearest-neighbor bond is only counted once. The spring constants are functions of the bulk modulus  $B$  and the nearest-neighbor distance  $L^0$  (Feng *et al.*, 1985)

$$K = \frac{3L^0}{2\sqrt{2}}B. \quad (3.10)$$

The mean and variance of the bond length distribution become particularly transparent within the CFM when *all the force constants are equal*, as the model can be solved analytically. The mean lengths and their variances can be expressed as a function of  $a^{**}$ , the topological rigidity parameter defined in terms of the radial force on the 12 nearest neighbors, required to open up a cage. These results have been described in the previous chapter.

It is also possible to find the effective elastic constant  $K_e$  by an effective medium theory (Thorpe and Wang, 1987) when the force constants vary. It can be shown within the CFM that the equations for the lengths and spring constants decouple so that the effective spring constant  $K_e$  is independent of the length

mismatch. From effective medium theory, and using the relation (3.8), we have

$$\frac{(1-x)(K_{AA}-K_e)}{K_e(1-p_I)+K_{AA}p_I} + \frac{x(K_{BB}K_e)}{K_e(1-p_I)+K_{BB}p_I} = 0, \quad (3.11)$$

where  $p_I = \frac{1}{2}(1+a^{**})$  determines the initial slope for the conductance (Thorpe and Wang, 1987, and Cai *et al.*, 1990), which obeys the same effective medium equation as the spring constant. Equation (3.11) is a quadratic for  $K_e$ , which always is sublinear and monotonic in the concentration  $x$ . As we will see in the Sec 3.4, these analytical results are very close to the ones obtained with the EAM. The CFM is a very simple and somewhat crude model, but gives surprisingly good results for some of the alloys, particularly those containing Pt.

### 3.3 Computer simulations

The computer simulation results shown in this paper for both the EAM and CFM have been obtained by statically minimizing the total energy using a conjugate-gradient program developed by Press *et al* (1986) (see appendix A). I have checked this algorithm against the simplex algorithm as well as against analytical results (see next chapter). The conjugate-gradient method is in general faster than the simplex method and at least as accurate. Moreover, it is in almost perfect agreement with the exact analytical results presented for *c*-SiGe alloys. The simulations have been performed with 4000 atoms in an fcc arrangement with a cubic supercell and periodic-boundary conditions. In the relaxation, all the atoms were free to move and the volume of the supercell could change while remaining cubic. The elastic constants are computed by varying the shape and/or size of the unit cell appropriately and re-relaxing the system. This method leads to three figure accuracy, which is comparable or better than the available experimental results.

It was found that the supercell was large enough so that it was not necessary to do any ensemble averaging.

### 3.4 Results

In Figs. 3.1 – 3.6, I compare the EAM and CFM computer simulation results with diffraction data where available, and with EXAFS data for  $\text{Ni}_{1-x}\text{Au}_x$  in Figure 3.6. In Figure 3.1 for AuAg, the EAM results agree extraordinarily well with diffraction data and are clearly superior to the CFM results. Because Au and Ag atoms have very similar sizes, one would expect this case to be quite uninteresting as indeed the results are for the CFM. The experimental data show a minimum in the mean length at about  $x \simeq 0.4$ . Fournet (1953), using an elastic sphere approximation, predicted that the deviation from Végard's law should be maximum for very small length mismatch but gave no number and was working in the virtual crystal approximation. As seen in Figure 3.1, the EAM follows almost *exactly* the experimental data except at low concentration of Au, where the difference is only due to the fact that the lattice parameter of pure Ag has not been taken at the experimental temperature to fit the parameters for the EAM potential. For this alloy only, the simulation results have been obtained using a polynomial potential with a cut-off radius after the third shell of neighbors. This potential is very similar to the one described here, for more details see Appendix B. I used a longer range interaction for this alloy because Johnson (1990) mentioned that it is the only one which shows some change in energy with the range of interaction. All the other alloys studied here are quite stable under such a change. Note that the condition  $C_{11} = C_{12} + C_{44}$  is *not* obeyed in either the pure materials or the alloy due to the further neighbor interactions. It is worth mentioning

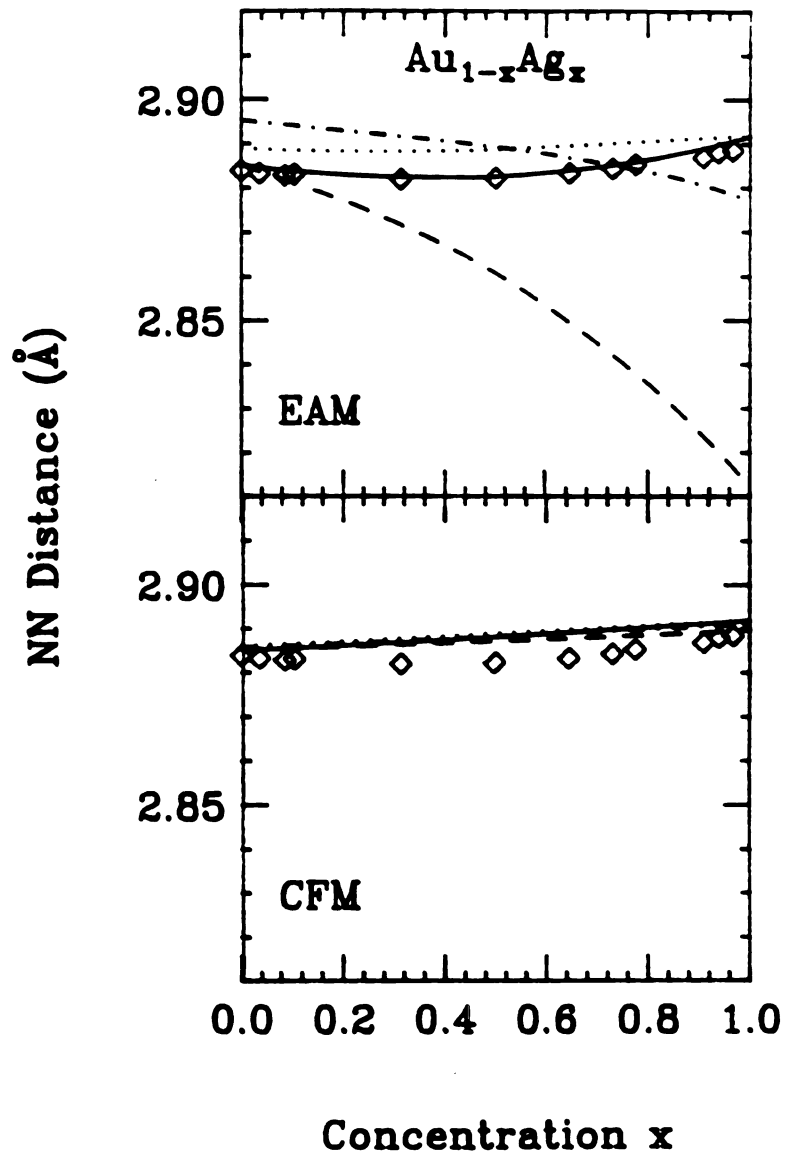


Figure 3.1: The mean A-A, A-B, B-B nearest-neighbor distances and the lattice parameter are shown for the alloy  $A_{1-x}B_x$ . Dashes are for A-A distance; dot-dashes, for A-B distance; dots, for B-B distance; and the continuous line is for the mean distance. The symbols are experimental data. The upper panel is for the embedded atom method (EAM) and the lower panel is for the central force model (CFM). This figure is for  $Au_{1-x}Ag_x$ . The diffraction data for  $Au_{1-x}Ag_x$  (Karmazin, 1969) is shown as diamonds.

that Ackland and Vitek (1990) also see a minimum with their EAM potential but around  $x \simeq 0.5$ . The behavior of the Au–Au bond length in this alloy is quite strange; instead of becoming closer to the length of the Ag–Ag bond, it decreases by more than  $0.07\text{\AA}$  (3%), close to 10 times the length mismatch! This behavior can be explained by looking at the parameters for the potential: the easiest way for the Au atom to satisfy its need for a large electronic density is to become closer to another Au atom. But, besides the mean length which agrees with the experiment, it is impossible to tell whether or not this behavior is real. As this behavior is probably too small to be discerned by EXAFS, only *ab initio* calculations, especially of Au–Au pairs in Ag, can give further insight into this phenomenon.

In Figure 3.2, the results for CuAu alloys show that the EAM and CFM are about equally good, but do show systematic discrepancies with the diffraction results. The results for CuPd in Figure 3.3 give impressive agreement with the diffraction results for both EAM and CFM. The partial mean lengths are also similar, suggesting that electronic density effects do not make much difference here. In contrast the results for PdPt in Figure 3.4, show that the CFM is superior to the EAM in reproducing the diffraction data. The CFM produces a very narrow range of mean lengths in this case with a minimal amount of bowing. The results of EAM and CFM are quite remarkably different in NiAg as shown in Figure 3.5, giving bowing with opposite signs. There is no experimental data on NiAg as it phase separates.

In Figure 3.6, I present the results for NiAu alloys, which are particularly important at the present time, as this is the only fcc metallic alloy for which there is EXAFS data (Renaud *et al.*, 1988). This alloy was chosen for the first EXAFS

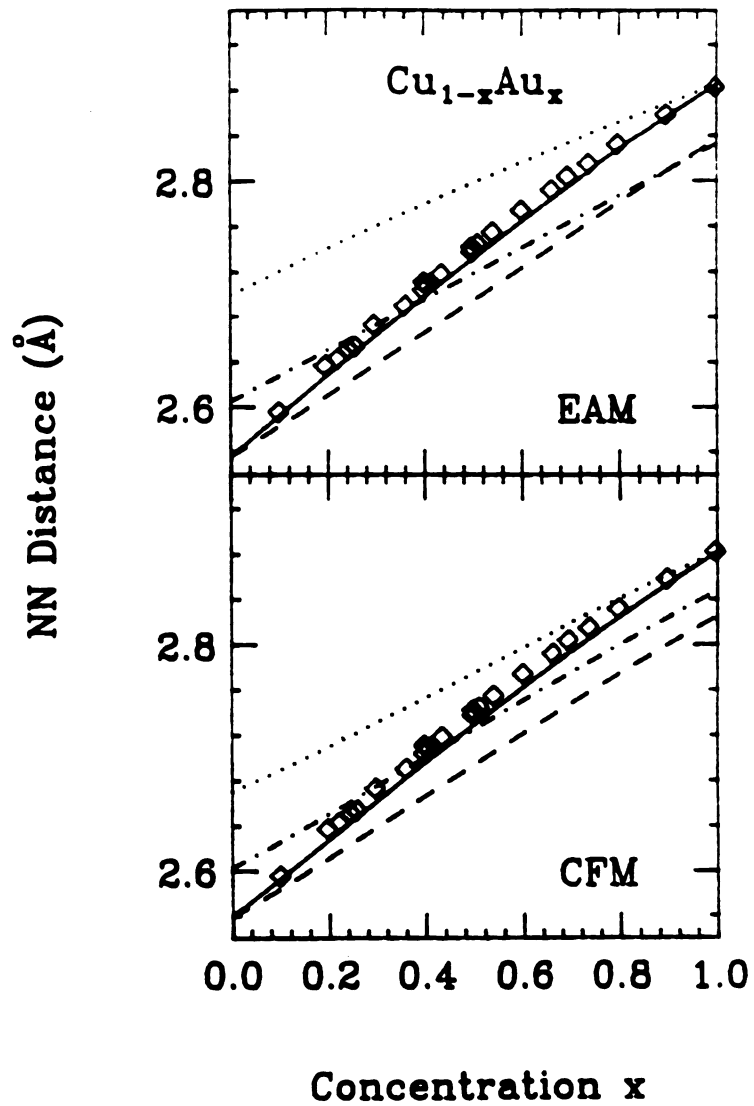


Figure 3.2: Same as Figure 3.1, except for  $\text{Cu}_{1-x}\text{Au}_x$ . The diffraction data for  $\text{Cu}_{1-x}\text{Au}_x$  is shown as diamonds (Linde, 1932; Nix and Macnair, 1941; Newkirk, 1953; and Lihl *et al.* 1971).

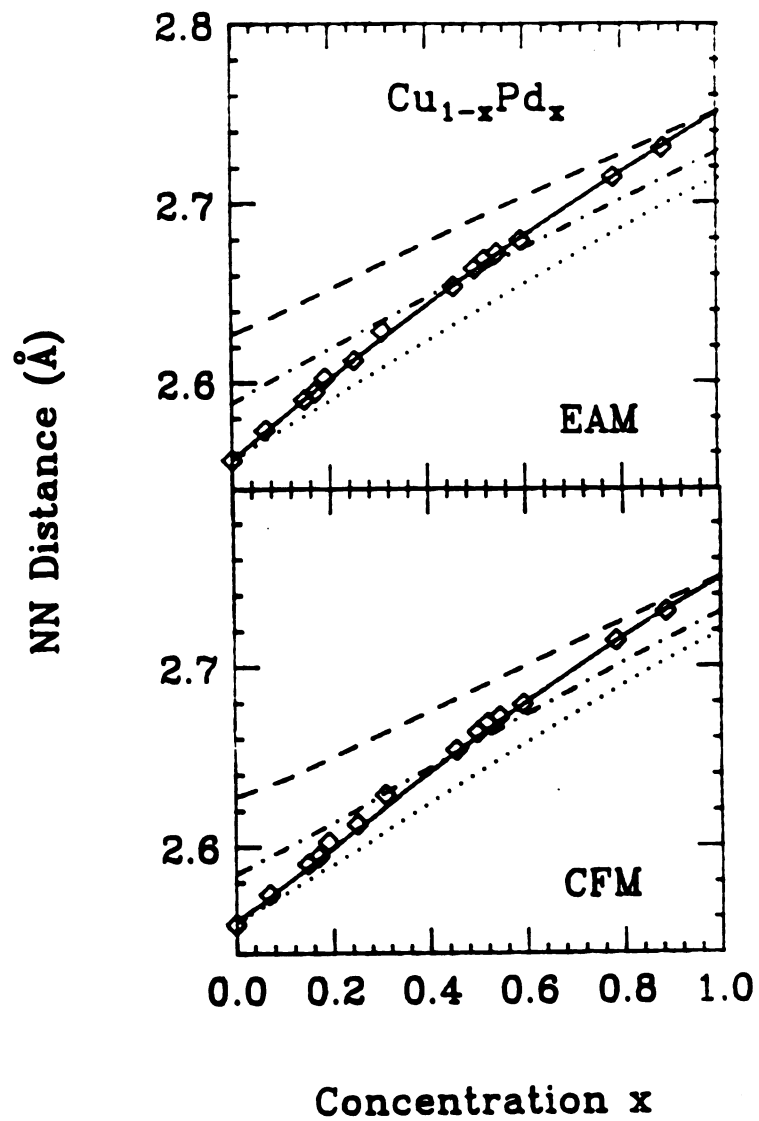


Figure 3.3: Same as Figure 3.1, except for  $\text{Cu}_{1-x}\text{Pd}_x$ . The diffraction data for  $\text{Cu}_{1-x}\text{Pd}_x$  is shown as diamonds (Pearson, 1958).

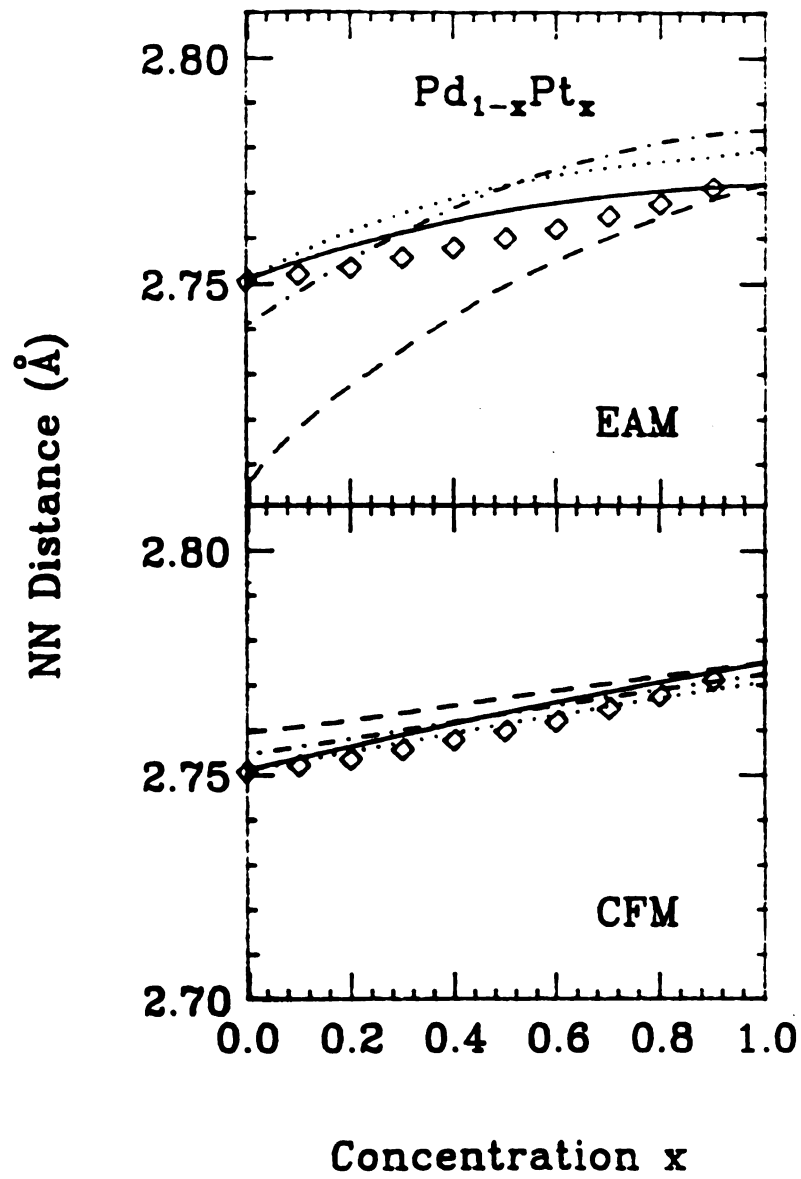


Figure 3.4: Same as Figure 3.1, except for Pd<sub>1-x</sub>Pt<sub>x</sub>. The diffraction data for Pd<sub>1-x</sub>Pt<sub>x</sub> is shown as diamonds (Darby and Miles, 1972).

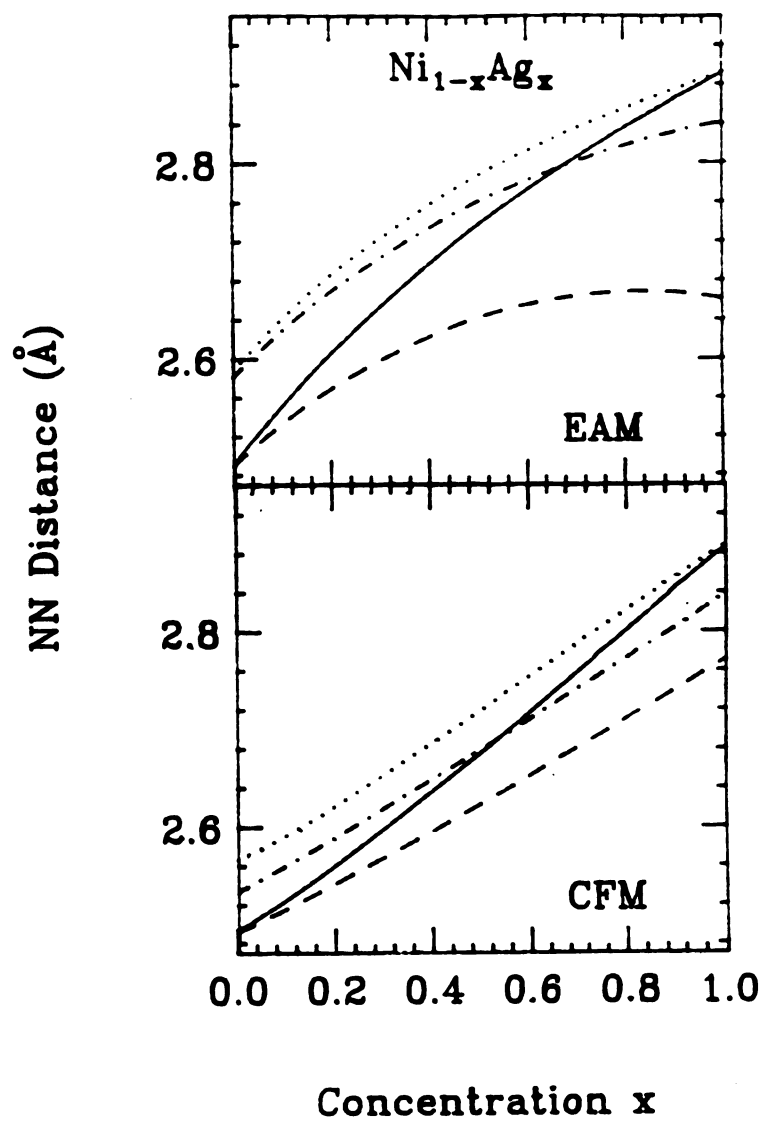


Figure 3.5: Same as Figure 3.1, except for  $\text{Ni}_{1-x}\text{Ag}_x$ .

study because the length mismatch between Ni and Au is about 15%, which is around the upper limit for forming solid solutions (Hume-Rothery, 1948). The EAM results are good for all the partial length distributions and clearly superior to the CFM. Note that some of the error bars on the EXAFS results are quite large. Note also that the EAM and CFM give bowing of *opposite* sign for the mean length. The difference between these two sets of results, suggests that electronic density effects are significant in NiAu alloys. The agreement obtained here between experiment and EAM is good. The large experimental uncertainties at low Ni concentration cannot discriminate between the EAM and the results with the Morse potential, used by Renaud *et al.* (1988), but the Morse potential gives a crossing of the Ni-Ni and Ni-Au curves which is perhaps less acceptable than the results presented here. Comparing with earlier EAM simulations by Ackland and Vitek (1990), using the Finnis-Sinclair model for CuAu and AuAg, and Foiles (1985) using the Daw-Baskes model for CuNi, we see that the overall behavior of the Johnson EAM potential produces a smoother variation of the lattice constant with concentration.

In Figs. 3.7-3.9, I show only the more successful of the EAM and CFM results for each alloy, as determined by comparison with the diffraction data. In all nine cases shown, one method was clearly superior to the other. Surprisingly, when examining results in Figs. 3.1-3.9, the CFM is superior to the EAM in at least as many cases as the EAM is superior to the CFM. Table 3.2 also shows that there is no clear preference for one approach over the other, which was of considerable surprise to us. With alloys containing platinum, the Johnson EAM potential does not give the right curvature for the mean length. Johnson already showed that his potential is weaker for Pt. It seems that the crude electronic

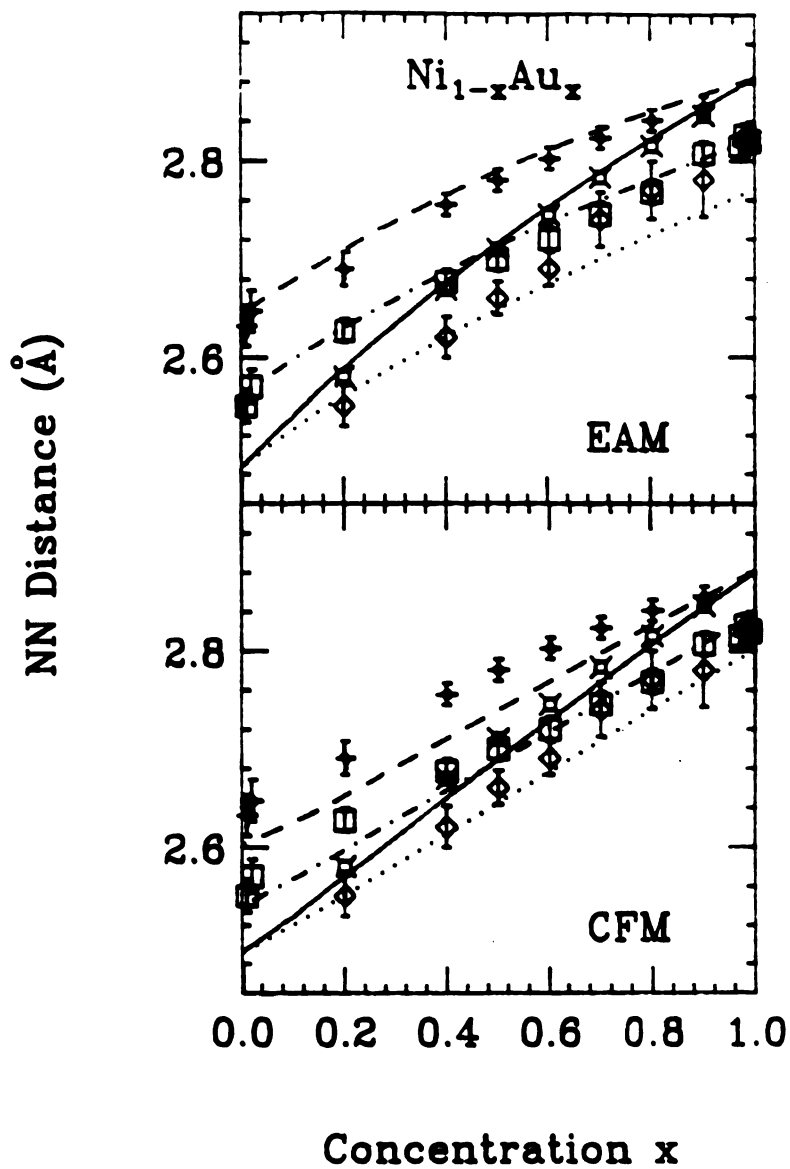


Figure 3.6: Same as Figure 3.1, except for  $\text{Ni}_{1-x}\text{Au}_x$ . The diffraction data for  $\text{Ni}_{1-x}\text{Au}_x$  is shown as stars (Renaud *et al.*, 1988). The EXAFS data, with error bars, is also taken from Renaud *et al.*. The diamonds, squares and small circles refer to the Ni-Ni, Ni-Au and Au-Au nearest-neighbor distances respectively.

model used in the embedded-atom method is not sufficient for platinum. But surprisingly, the CFM (with no adjustable parameters) is in very good agreement with the mean experimental nearest-neighbor distance for all but one alloy for which the embedded-atom potential fails (see Table 3.2). In Figs. 8 and 9, the simulations using the CFM and the diffraction results for the PtAg, PtAu, CuPt and NiPt are shown. There are small discrepancies for the NiPt alloy, although the curvature is negative, the same as in the experimental results. For PdPt, shown in Figure 3.4, the CFM does *not* give better agreement with experiment than the EAM potential, both having the *wrong* sign for the deviation from Végard's law. Figure 3.8 shows CFM simulations for NiCu and PdAg, which, as one can see, agree with the experimental data. In the next chapters, we will see that semiconductors can be described analytically by a simple harmonic spring model (with angular forces) because they approximately obey Pauling's rule of additivity of atomic radii, as expressed in Eq. (8). The results of simulations would suggest that platinum alloys also respect the Pauling rule with no or little anharmonicity in the potential.

A selection of results for the elastic constants is shown in Figure 3.9; experimental elastic data for alloys are virtually non-existent. But the smooth, rather uninteresting, behavior in every case might lead us to suppose that they are not too far from the real behavior, especially as the CFM and EAM give very similar results. The relation  $C_{11} = C_{44} + C_{12}$  holds for every concentration  $x$  within the limits of the precision on the numerical calculations using EAM for the alloys. In Figure 3.10, I present the bulk modulus and the Voight average shear modulus, computed using the EAM. The results for the pure metals are exact as they were used as input in determining the parameters in the EAM. Computing

**Table 3.2:** Alloys for which the EAM or the CFM gives the lattice parameter in agreement with experimental diffraction results (shown by a bullet). The crosses indicate disagreement with experimental results, and the blanks indicate that no experimental data was available. The third column refers to the Figure number(s) in this paper where the results are shown.

Alloy	EAM	Central Force	Figure
AuAg	•	×	1, 10
CuAg	•	×	7
PdAg	×	•	8
CuAu	•	•	2
NiAu	•	×	6, 10, 11
PdAu	•	×	7
NiCu	×	•	8
CuPd	•	•	3
NiPd	•	×	7
PtAg	×	•	8, 10
PtAu	×	•	9
CuPt	×	•	9
NiPt	×	•	9
NiAg			5
PdPt	×	×	4

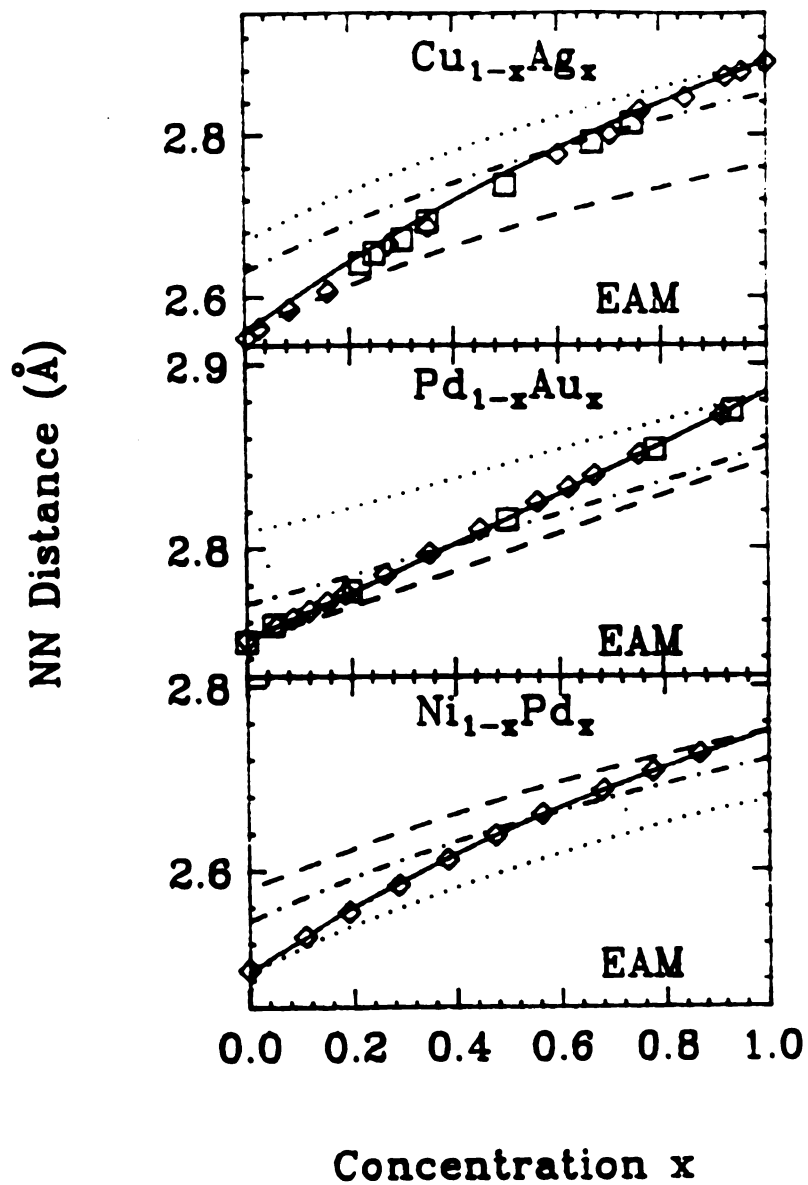


Figure 3.7: Showing the EAM results for  $\text{Cu}_{1-x}\text{Ag}_x$ ,  $\text{Pd}_{1-x}\text{Au}_x$  and  $\text{Ni}_{1-x}\text{Pd}_x$  in the three panels. In all cases, I show only the EAM results which were clearly better than the CFM results when compared with diffraction data (Pearson, 1958; Nagakura *et al.*, 1966; Mealand and Flanagan, 1964; and Bidwell, 1964).

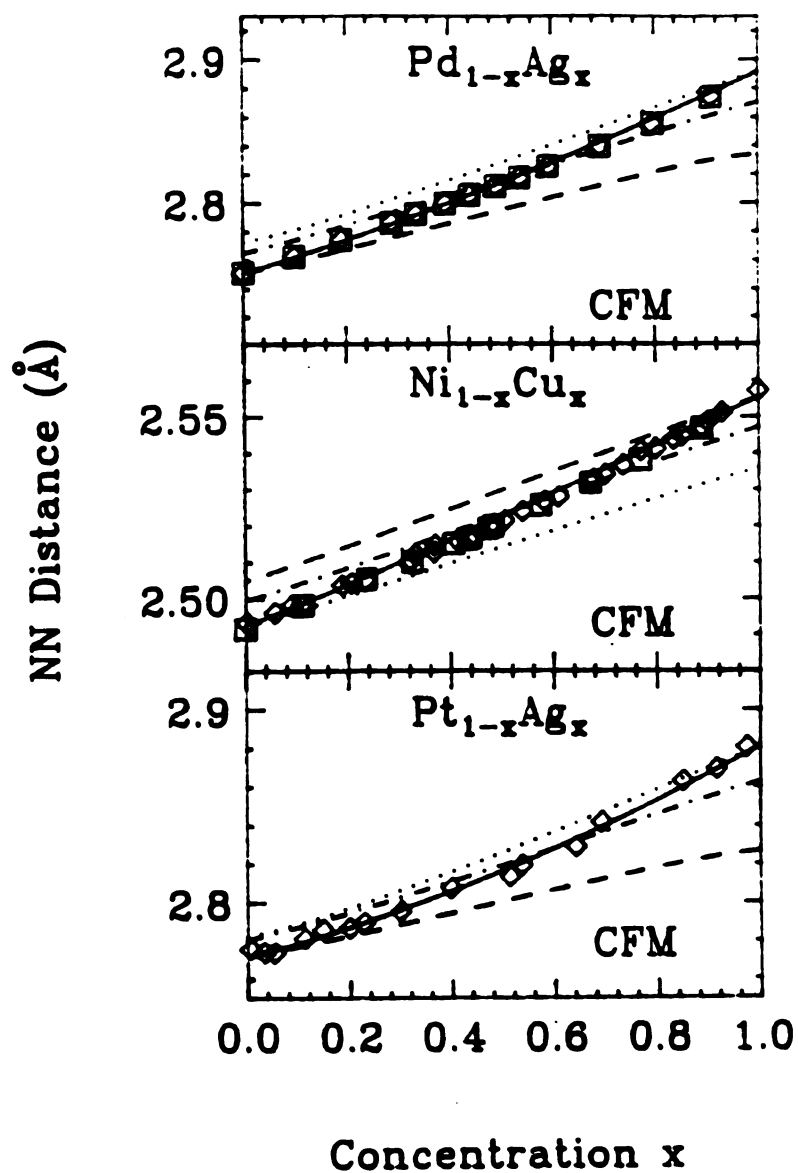


Figure 3.8: Showing the CFM results for  $\text{Pd}_{1-x}\text{Ag}_x$ ,  $\text{Ni}_{1-x}\text{Cu}$  and  $\text{Pt}_{1-x}\text{Ag}_x$  in the three panels. In all cases I show only the CFM results which were clearly better than the EAM results when compared with diffraction data (Coles, 1956 ; Owen and Pickup, (1934); Lihl *et al.*, 1971; Johansson and Linde, 1930, Novikava and Rudnitskii, 1957, Klement and Lui, 1963; and Ebet *et al.*, 1983).

the bulk modulus with both the spring model and the EAM potential, I find that its behavior is not very sensitive to the model used, and well described by the simple effective medium theory as given by (16). This effective medium approach must be applied separately to the bulk and shear moduli by fitting the end points via  $K_{AA}$  and  $K_{BB}$ . Note that the effective medium theory is designed to get the correct initial slope for small  $x$  and  $1 - x$  (Thorpe and Wang, 1987). I find also that the behavior of the elastic constant is very different from that determined by Ackland and Vitek (1990). The calculation shows no change of curvature with the concentration in any of the alloys studied in this paper, as they observed for CuAu. Some experiments would be useful here.

Figure 3.11 shows the bond-length distribution for the CFM with *all the force constants equal* and for the EAM potential. The CFM with equal spring constants can be solved exactly to give the result 2.22 for the widths, in agreement with the simulation results shown in Figure 3.11. The widths for the three peaks for the CFM in Figure 11 are all equal and indeed the shapes are all similar apart from a vertical scale factor. The CFM results are rather different from the EAM results, but have the important common feature that the widths are comparable to the peak separation. The full width at half the maximum, compared to the peak separation  $\langle L_{BB} \rangle - \langle L_{AA} \rangle$  is given by

$$2\sqrt{x(1-x)\ln 2 \frac{(1-a^{**})}{a^{**}}} \quad (3.12)$$

where I have used the relations given in chapter 2 (Eqs. 2.29 and 2.34). The lattice enters through the topological rigidity  $a^{**}$ . At  $x = \frac{1}{2}$  the ratio (3.12) is much larger for metals,  $\simeq 1.48$ , than for semiconductors,  $\simeq 0.18$ , where a similar relation exists, so that the length distributions are wide in the metal alloys studied here as seen in Figure 11. In semiconductors the component peaks are more

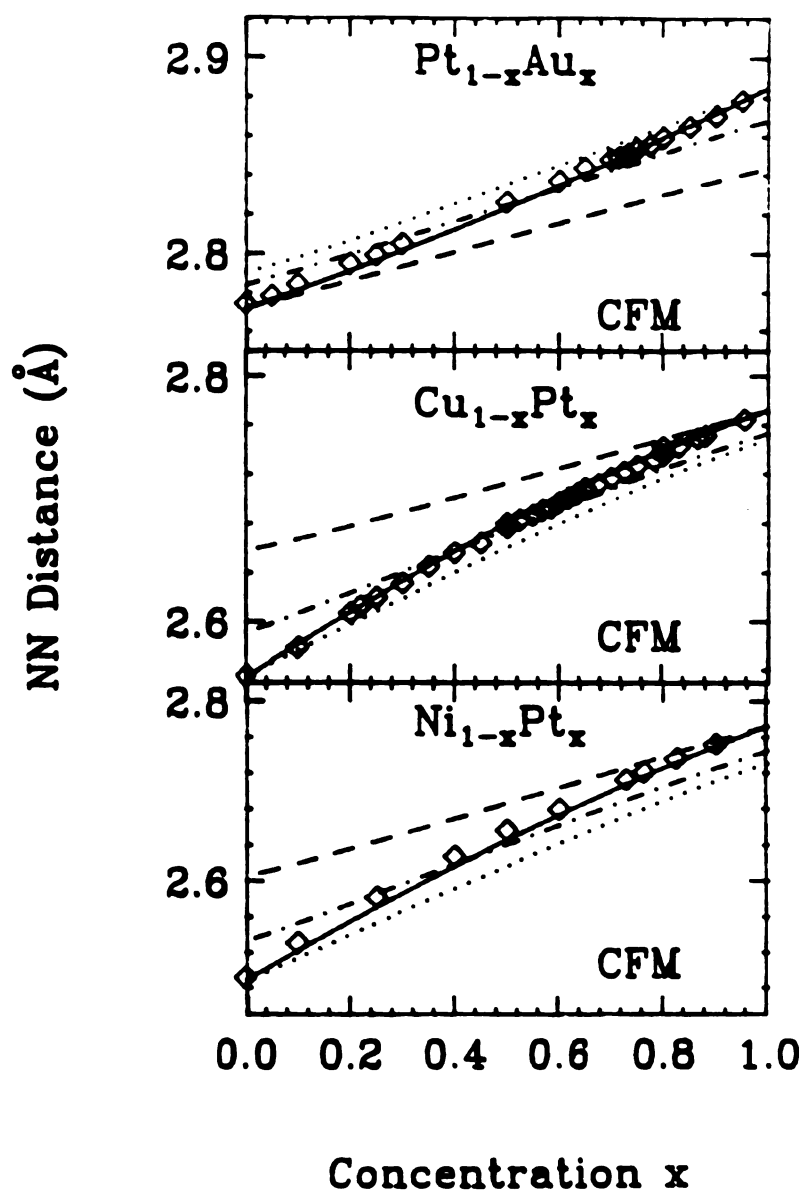


Figure 3.9: Showing the CFM results for  $Pt_{1-x}Au_x$ ,  $Cu_{1-x}Pt_x$  and  $Ni_{1-x}Pt_x$  in the three panels. In all cases I show only the CFM results which were clearly better than the EAM results when compared with diffraction data (Pearson, 1958).

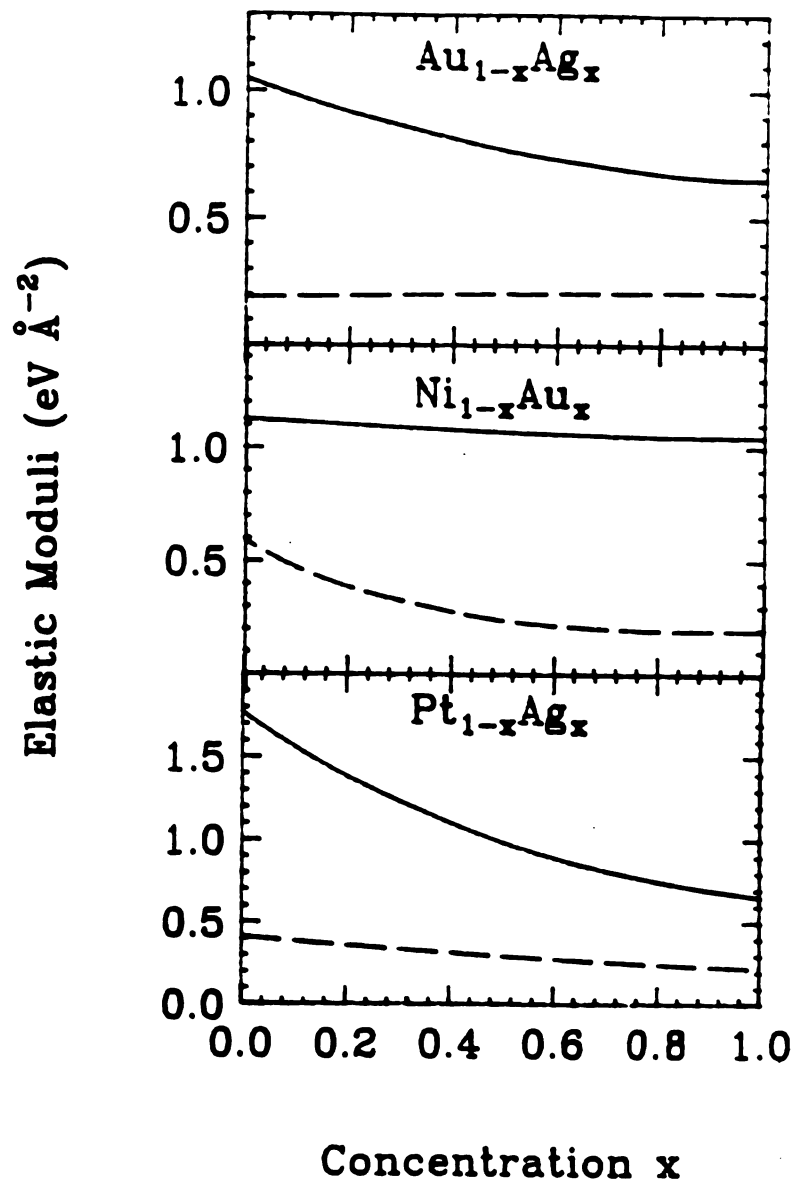


Figure 3.10: The bulk modulus (solid line) and the Voigt shear modulus (dashed line) for three different alloys obtained from the computer simulation with the EAM potential as described in the text.

separated. These results make it very hard to justify using any virtual crystal type of approximation for the electronic properties of alloys, even at the crudest level.

### 3.5 Conclusion

This work gives no clear result in determining as to whether the central force model (CFM) or the embedded-atom method (EAM) is superior. For platinum alloys and a few others, the CFM is clearly superior, but in all other cases the EAM is better. This may be related to the amount of electronic density effects in the alloy. The Johnson EAM is very successful in NiAu alloys; the only case in which EXAFS data is available. The surprising contraction of the Au-Au bond in Ag rich AuAg alloys within the EAM, points out that more *ab initio* calculations are needed for both single and pair *defects* in metals. Armed with this information, it will be possible to construct EAM potentials that will interpolate over the whole concentration range. In the absence of such calculations, the present results can be taken as a guide, but with a good deal of skepticism. The CFM explains why the widths of the length distributions are so wide, when compared to semiconductor alloys. This is because the fcc metal lattices have a topological rigidity parameter  $a^{**} \simeq 0.24$  as compared with semiconductors where  $a^{**} \simeq 0.8$ . The width of these distributions means that the virtual crystal approximation is particularly inappropriate in metallic alloys.

The effect of variation of electronic density is important in many cases and is taken into account by the embedded-atom-method potential and is sufficient in many cases to give the correct variation of the lattice parameter with the concentration for most alloys, not containing Pt. The elastic constants show

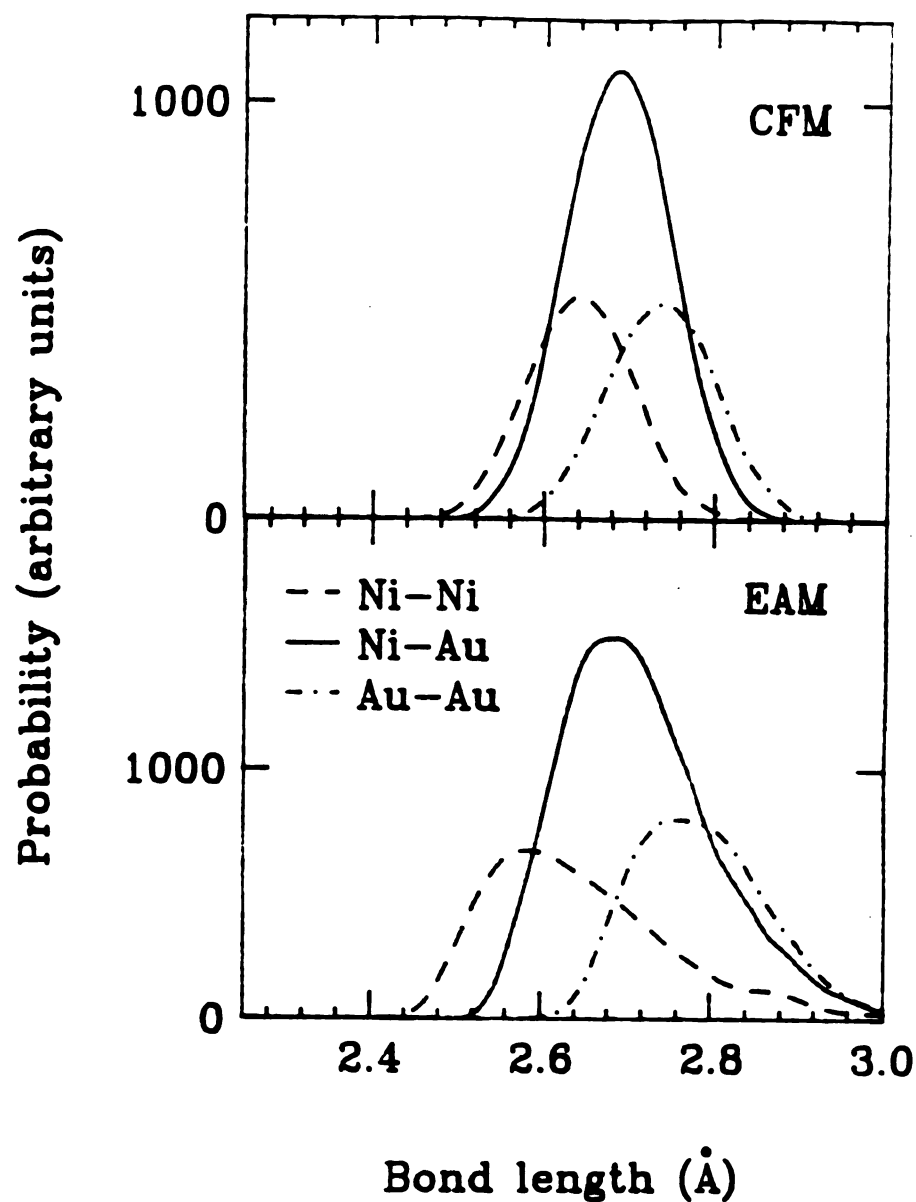


Figure 3.11: The bond length distributions for Ni-Ni, Ni-Au and Au-Au nearest-neighbor distances in an  $\text{Ni}_{0.5}\text{Au}_{0.5}$  alloy, computed using both the CFM (with no variation in the force constants) and the EAM.

monotonic behavior with the concentration, and seem to be insensitive to the model used.

## Chapter 4

# Crystalline and Amorphous SiGe

The SiGe alloys represent an important opportunity for the micro-electronic industry because of their opto-electronic properties when deposited as a multilayer alternating with Si. To fully understand their properties, it is necessary to obtain a good knowledge of the effect of length mismatch, which is about 4%, on the strain. Recently, a few experimental and simulational papers have been published on this topic (de Gironcoli, *et al.*, 1991; Matsuura *et al.*, 1991; Weidmann and Newman, 1992; Incoccia *et al.* 1985; and Nishino *et al.*, 1988). In this chapter, I examine the mismatch problem in bulk semiconductor binary alloys, which are a special case of the general theory for quaternaries, presented in Cai and Thorpe (1992a, 1992b). I will concentrate on studying the effect of length mismatch for the SiGe alloys and show that it is possible to understand most of the important structural features with the help of simple analytic results.

Amorphisation is also a very important phenomenon in semiconductor technology, as amorphous materials often share similar electronic properties with crystals while being much easier to grow (Stutzmann *et al.*, 1989; and Mackenzie *et al.*, 1985). Very little work has been done to date to study the effect of amor-

phisation on the length mismatch problem. Incoccia *et al.* (1985) and, a few years later, Nishino *et al.* (1988) have measured the Ge-Ge and Si-Ge nearest-neighbor distances in hydrogenated amorphous silicon (*a*-SiGe) but I am not aware of any computational or analytical work. Schemes for constructing a *perfect* tetrahedral amorphous structure (i.e. *every* site is fourfold coordinated) with periodic boundary conditions were introduced a few years ago (Wooten *et al.*, 1985; and Wooten and Weaire, 1987). When studying amorphous systems, analytical results for structural properties are usually difficult to obtain since one cannot generally use expressions valid in the pure crystal limit. However, the situation in *a*-SiGe is made tractable because the length mismatch in SiGe is small and therefore the strain induced by the alloying can be treated as a perturbation on the ideal amorphous network. Such behavior allows us to use the theory developed for the crystalline case without any major modifications. Végard's law is again predicted and the topological rigidity parameter  $\alpha^{**}$  is *unchanged* by the amorphisation such that the mean partial length equations are still valid and shown to be independent of the amorphisation. For the next-nearest-neighbor distances, one must include some effects due to the amorphisation and we will see that all the length *distributions* are completely dominated by the amorphisation, which leads to much larger angular distortions between the tetrahedral bonds, than does the alloying.

In section 4.1, I describe the theory for a binary alloy of the form  $A_{1-x}B_x$  for  $Si_{1-x}Ge_x$  with results for the nearest and next-nearest neighbors. In section 4.2, I compare the analytical results with computer simulations using the Kirkwood model and with some *ab initio* results recently obtained by de Gironcoli *et al.* (1991). In section 4.3, I examine the effect of amorphisation on the strain energy by substituting Ge for Si atoms in a *a*-Si supercell constructed by Wooten

Table 4.1: The force constants  $\alpha$  and  $\beta$  in N/m for the Keating and Kirkwood models obtained from the elastic modulus  $C_{11}$  and the bulk modulus  $B = \frac{1}{3}(C_{11} + 2C_{12})$  (Bublik *et al.*, 1974).

	Kirkwood		Keating	
	$\alpha$	$\beta$	$\alpha$	$\beta$
Si	53.09	13.81	48.49	13.81
Ge	42.28	11.30	38.51	11.31

(1991) using the Wooten, Winer and Weaire algorithm (1985). I compare the results with EXAFS experiments performed on *hydrogenated* amorphous silicon-germanium alloys by Incoccia *et al.* (1985) and by Nishino *et al.* (1988).

## 4.1 Solution for binary alloys

As discussed in chapter 2, analytical results have been obtained using the Kirkwood potential,

$$V = \frac{\alpha}{2} \sum_{\langle ij \rangle} (L_{ij} - L_{ij}^0)^2 + \frac{\beta}{8} L_e^2 \sum_{\langle ijk \rangle} \left( \cos \theta_{ijk} + \frac{1}{3} \right)^2, \quad (4.1)$$

where  $\alpha$  and  $\beta$  are taken to be the *same* for all bonds. This is a reasonable assumption in the case of semiconductor alloys since the topological rigidity constants are not very sensitive to changes in the elastic constants and, as can be seen in Table 4.1, differ only by about 20% between pure Si and pure Ge (Bublik *et al.*, 1974). As there is no evidence for any appreciable bowing in the partial lengths, there is no reason to go beyond this assumption for SiGe alloys. The mean length  $L_e$  is introduced in (4.1) so that the ratio  $\beta/\alpha$  is dimensionless. For the potential (4.1), the mean length follows Végard's law.

The natural (unstrained) lengths  $L_{SiSi}^0$  and  $L_{GeGe}^0$  are obtained from the pure crystals while the mixed length  $L_{SiGe}^0$  is taken to be the arithmetic average

$$L_{SiGe}^0 = \frac{1}{2}(L_{SiSi}^0 + L_{GeGe}^0). \quad (4.2)$$

Although inappropriate for most metal alloys, the additivity of the atomic radii (Pauling, 1967) has been found to hold generally for semiconductors. Martins and Zunger (1986) obtained a value very close to sum of the radii of Si and Ge in a first-principles self-consistent calculation of an ordered zincblende SiGe structure.

The solution for binary alloys can be obtained directly, as mentioned earlier, as a special case of the general solution for quaternaries presented in Cai and Thorpe (1992a) where  $A = C = Si$  and  $B = D = Ge$  in  $A_{1-x}B_xC_{1-y}D_y$ . The mean lengths are then given by

$$\begin{aligned} L_e &= (1-x)L_{SiSi}^0 + xL_{GeGe}^0 \\ \langle L_{SiSi} \rangle &= L_e - xa^{**} (L_{GeGe}^0 - L_{SiSi}^0) \\ \langle L_{GeGe} \rangle &= \langle L_{SiSi} \rangle + a^{**} (L_{GeGe}^0 - L_{SiSi}^0) \\ \langle L_{SiGe} \rangle &= \frac{1}{2} (\langle L_{GeGe} \rangle + \langle L_{SiSi} \rangle). \end{aligned} \quad (4.3)$$

The topological rigidity parameter,  $a^{**}$ , is defined by a lattice integral and is related to the ratio of force constants  $\beta/\alpha$  by an interpolation formula (Cai and Thorpe, 1992b):

$$a^{**} = \frac{1 + 1.249(\beta/\alpha)}{1 + 3.600(\beta/\alpha) + 1.171(\beta/\alpha)^2}. \quad (4.4)$$

that is valid for any reasonable value of  $\beta/\alpha$ .

The second moments of the three length distribution functions about their centers are given by

$$\langle L_{SiSi}^2 \rangle - \langle L_{SiSi} \rangle^2 = \langle L_{GeGe}^2 \rangle - \langle L_{GeGe} \rangle^2$$

$$\begin{aligned}
&= \langle L_{SiGe}^2 \rangle - \langle L_{SiGe} \rangle^2 \\
&= \frac{1}{2}x(1-x)a_1^{**} \left( L_{GeGe}^0 - L_{SiSi}^0 \right)^2 \quad (4.5)
\end{aligned}$$

where  $a_1^{**}$  is defined as

$$a_1^{**} = \frac{\partial(a^{**}y)}{\partial y}. \quad (4.6)$$

where  $y = \beta/\alpha$  The third moments can also be computed; they are all identical for the three distributions and vanish at  $x = 0.50$  (Cai *et al.*, 1990). Using supercells of up to 125 000 sites relaxed with a Kirkwood potential, Weidmann and Newman (1992) confirmed numerically that the bond length distributions are identical for Si-Si, Si-Ge and Ge-Ge at all concentrations.

The strain energy per atom can also be written as a function of the topological rigidity parameter

$$\epsilon = \frac{\alpha}{2}x(1-x)(1-a^{**})(L_{GeGe}^0 - L_{SiSi}^0)^2. \quad (4.7)$$

From the general theory for quaternaries, one can obtain all the next-nearest-neighbor distances,

$$\begin{aligned}
\langle L \rangle_{i\alpha j}^{\epsilon_1 \epsilon_2 \epsilon_3} &= L_e^{nnn} \\
&+ \frac{(L_{GeGe}^0 - L_{SiSi}^0)}{2} \left[ \sqrt{\frac{8}{3}} a^{**} \left( \frac{2x-1+\epsilon_2}{2} \right) + \sqrt{\frac{3}{8}} b^{**} \left( 2x+1 - \frac{\epsilon_1+\epsilon_3}{2} \right) \right] \quad (4.8)
\end{aligned}$$

where  $L_e^{nnn} = \sqrt{8/3}L_e$  is the mean next nearest neighbor distance and  $\epsilon$  is +1 for Si, and -1 for Ge. It is easy to see that all the distances are, contrary to the results obtained for pseudobinary alloys (Cai and Thorpe, 1992b), a *translation* of the same straight line. Here, as the two sublattices contain the same atoms, one cannot distinguish between them and the slope for the six curves is the same. There are two groups of curves, corresponding to the type of atom sitting at

the center of the triplet. Using results from Cai and Thorpe (1992a), the mean next-nearest neighbor distances can be written explicitly as

$$\begin{aligned} \langle L_{SiSiSi} \rangle &= L_e^{nnn} - \frac{(L_{GeGe}^0 - L_{SiSi}^0)}{2} \left[ \sqrt{\frac{8}{3}} a^{**} x + \sqrt{\frac{3}{8}} b^{**} 2x \right] \\ \langle L_{SiSiGe} \rangle &= L_e^{nnn} - \frac{(L_{GeGe}^0 - L_{SiSi}^0)}{2} \left[ \sqrt{\frac{8}{3}} a^{**} x + \sqrt{\frac{3}{8}} b^{**} (2x - 1) \right] \\ \langle L_{GeSiGe} \rangle &= L_e^{nnn} - \frac{(L_{GeGe}^0 - L_{SiSi}^0)}{2} \left[ \sqrt{\frac{8}{3}} a^{**} x + \sqrt{\frac{3}{8}} b^{**} 2(x - 1) \right] \end{aligned}$$

and

$$\begin{aligned} \langle L_{SiGeSi} \rangle &= L_e^{nnn} - \frac{(L_{GeGe}^0 - L_{SiSi}^0)}{2} \left[ \sqrt{\frac{8}{3}} a^{**} (x - 1) + \sqrt{\frac{3}{8}} b^{**} 2x \right] \\ \langle L_{SiGeGe} \rangle &= L_e^{nnn} - \frac{(L_{GeGe}^0 - L_{SiSi}^0)}{2} \left[ \sqrt{\frac{8}{3}} a^{**} (x - 1) + \sqrt{\frac{3}{8}} b^{**} (2x - 1) \right] \\ \langle L_{GeGeGe} \rangle &= L_e^{nnn} - \frac{(L_{GeGe}^0 - L_{SiSi}^0)}{2} \left[ \sqrt{\frac{8}{3}} a^{**} (x - 1) + \sqrt{\frac{3}{8}} b^{**} 2(x - 1) \right]. \end{aligned} \tag{4.9}$$

The topological rigidity parameter  $b^{**}$  is also defined by a lattice integral and describes the opening of the second-neighbor shell when applying a force on the first neighbors. As explained in chapter 2, it is found numerically that  $b^{**} = a^{**}/2$ , with the Kirkwood potential (Equation 4.1) (for all values of  $\beta/\alpha$ ).

Therefore all the partial nearest and next-nearest-neighbor lengths depend on only *a single parameter*,  $a^{**}$ . This parameter can be obtained from the  $Z$  plot via

$$a^{**} = \frac{\langle L_{GeGe} \rangle - \langle L_{SiSi} \rangle}{L_{GeGe}^0 - L_{SiSi}^0} \tag{4.10}$$

where the partial lengths are taken at the same concentration. One can then predict the width of the nearest-neighbor bond length distribution (4.5) and all

the next-nearest-neighbor distances using (4.9). The slopes of the set of parallel lines for the mean next-nearest-neighbor lengths (4.9) is given by (since  $L_e^{nnn}$  is also  $x$  dependent)

$$\sqrt{\frac{8}{3}} (L_{GeGe}^0 - L_{SiSi}^0) \left[ 1 - \frac{11}{16} a^{**} \right] \quad (4.11)$$

and the distance between the curves in the same group is  $\sqrt{3/128} a^{**} (L_{GeGe}^0 - L_{SiSi}^0)$ , while the distance between the two groups is  $\sqrt{2/3} a^{**} (L_{GeGe}^0 - L_{SiSi}^0)$ .

## 4.2 Results

To ascertain the quality of this theory, as applied to binary semiconductor alloys, I performed simulations using the Kirkwood model from which the analytical model has been developed. I statically relax unit cells of  $8(12)^2 = 13824$  atoms with periodic boundary conditions using the conjugate gradient method.

From Figure 4.1, we can see that the analytical results and the simulations performed using the Kirkwood potential correspond closely. This agreement was expected from previous studies of similar systems which showed that the approach used holds to a very good accuracy up to a mismatch much greater than the one studied here (Thorpe and Garboczi, 1990; Cai *et al*, 1990). Also shown in this figure are results obtained recently by de Gironcoli, Giannozzi and Baroni (1991) who have computed the structural (and thermodynamic) properties of a relaxed random solid solution of  $Si_{1-x}Ge_x$ , by expanding the pseudopotential to second order about the virtual crystal. In order to compare our respective simulations, I adjusted  $a^{**} = 0.707$  from their results, which corresponds to fixing the ratio  $\beta/\alpha$  at 0.20 using Equation (4.4). By so choosing  $a^{**}$ , one determines the mean bond lengths for Si-Si, Ge-Ge and Si-Ge in Figure 4.1.

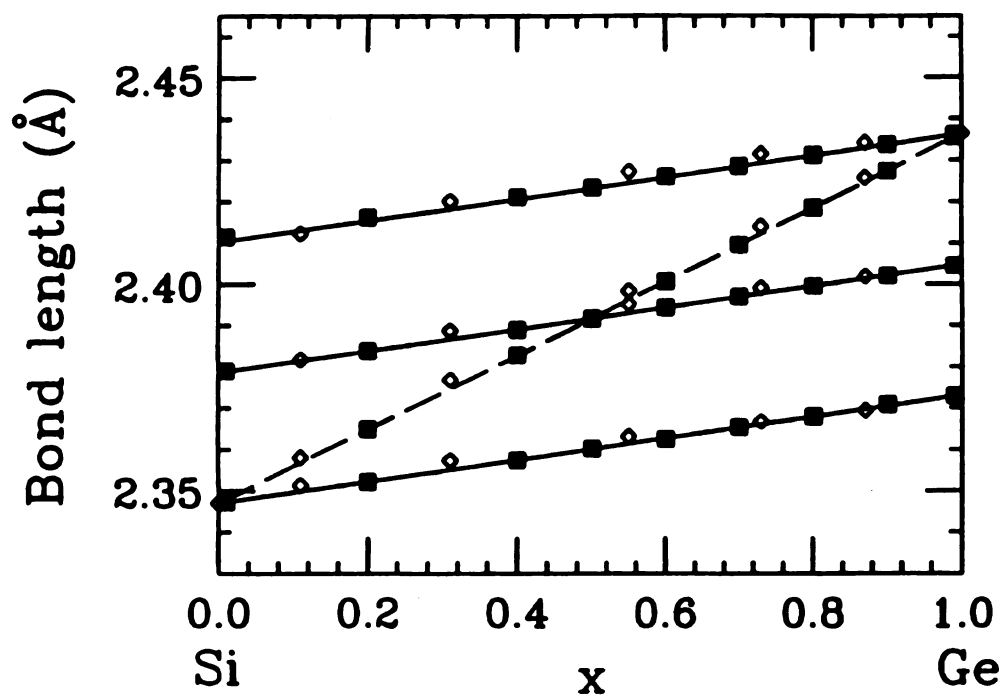


Figure 4.1: Mean nearest-neighbor bond lengths for  $\text{Si}_{1-x}\text{Ge}_x$ . The solid line is the analytic theory compared to simulations for the Kirkwood model shown as the solid symbols. The open symbols are from de Gironcoli *et al.* (1991).

It is also possible to compare the nearest-neighbor distribution predicted by the theory with the data computed by de Gironcoli and collaborators as shown in Figure 4.2(a). Around  $x = 0.50$ , the third moment of the distribution is small and the distribution is well described by a gaussian with the width given by Equation (4.5). De Gironcoli's length distributions are wider than predicted by this model. This difference lies in the fact that they obtained their results with constant chemical potential instead of constant concentration, broadening the distribution. In Figure 4.2(b), the same peaks are shown but they have been moved to place their center at the origin. The heights have been rescaled but not the widths. As predicted by the theory, all the peaks are identical. In Figure 4.3, we see the distribution for  $x = 0.11$  with the gaussian second moment predicted by the theory. The small asymmetry is explainable by higher order moments. Note that again the three peaks scale perfectly as expected. It is particularly surprising that this scaling still holds in the dilute limit of small  $x$  or  $(1 - x)$ .

The length for the Si-Ge bond lies within the experimental error limits of a recent EXAFS experiment performed on silicon-rich SiGe/Si(100) films by Matsuura, Tonnerre and Cargill III (1991) where they obtain (for low concentration of Ge),  $2.375 \pm 0.02 \text{ \AA}$ . This error is much too big to eliminate any model of  $\text{Si}_{1-x}\text{Ge}_x$ . To distinguish between models, an experiment would have to have an error of no more than  $\pm 0.002 \text{ \AA}$ .

This theory gives the exact Vegard's law while we know from X-ray diffraction that there is a downward bowing with a maximum deviation of about 4% (Dismukes *et al.*, 1964). It would be possible to implement this bowing by changing the length of the heterobond (see Appendix A). The causes of this small effect are subtle and would require much more advanced simulations to understand

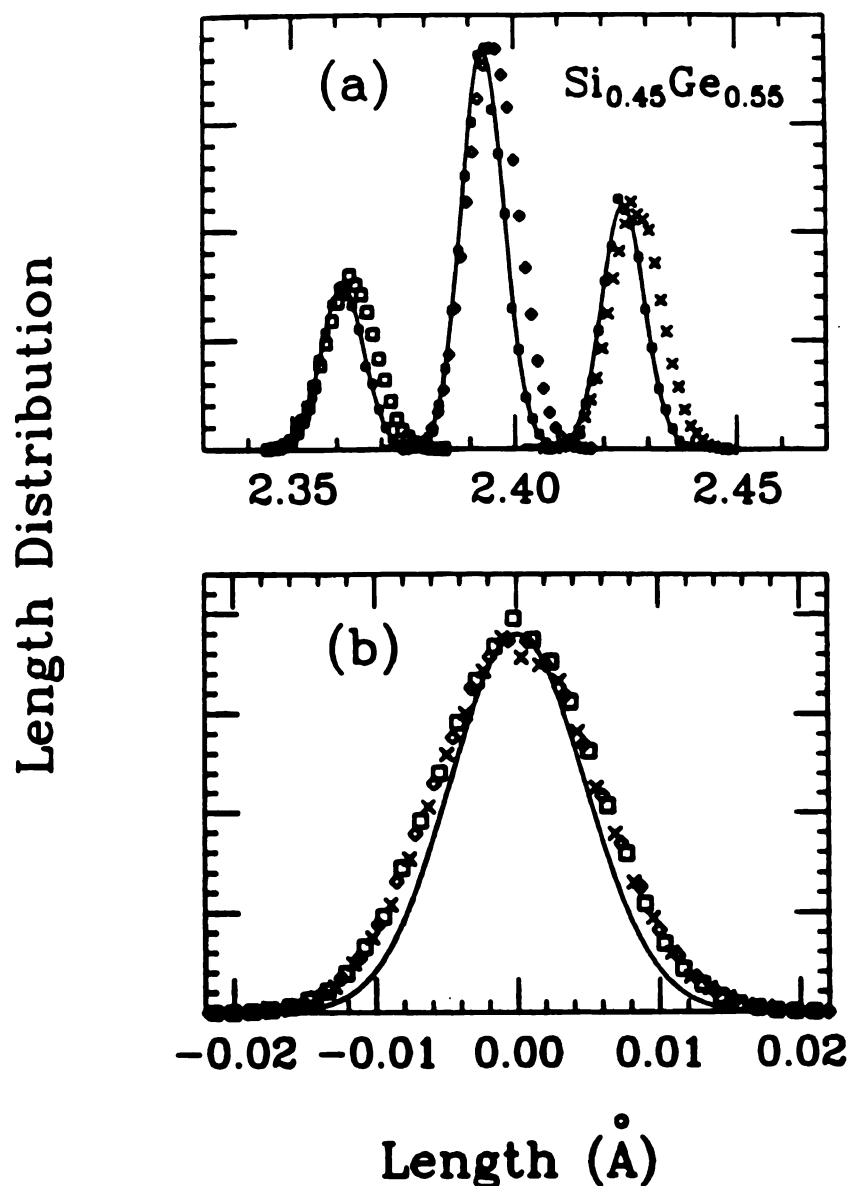


Figure 4.2: (a) The nearest-neighbor length distribution for  $\text{Si}_{1-x}\text{Ge}_x$  at  $x = 0.45$ . The solid lines are gaussians using the correct weights, centers (3) and widths. The solid symbols are from simulations using the Kirkwood potential. The open symbols are from the simulation by de Gironcoli *et al.*, with squares: Si-Si; triangles: Si-Ge; diamonds: Ge-Ge. (b) The three peaks have been moved to have their maxima at the same position and their height has been rescaled. Symbols have the same meaning as in (a). The solid line is a gaussian obtained with the parameters from the analytic theory (5).

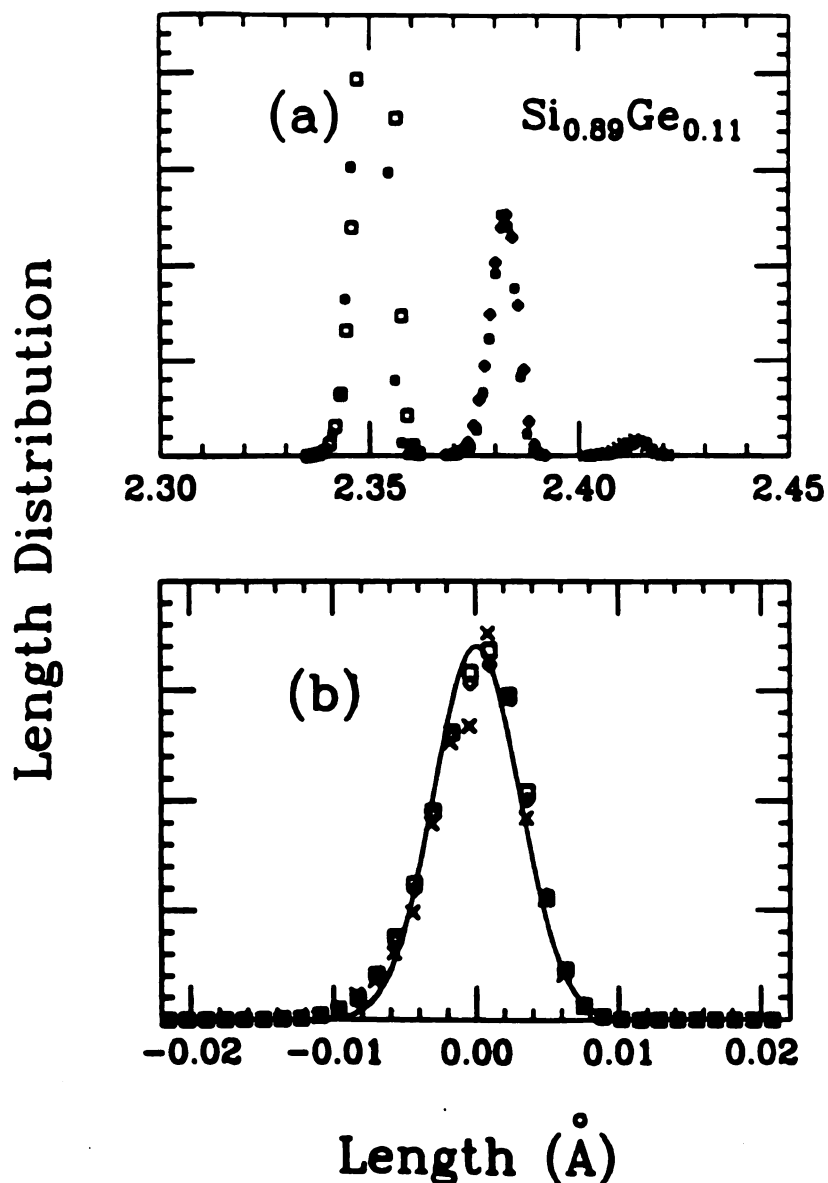


Figure 4.3: (a) The nearest-neighbor length distribution for  $\text{Si}_{1-x}\text{Ge}_x$  at  $x = 0.11$ . The solid lines are gaussians using the correct weights, centers (3) and widths. The solid symbols are from simulations using the Kirkwood potential. The open symbols are from the simulation by de Gironcoli *et al.*, with squares: Si-Si; triangles: Si-Ge; diamonds: Ge-Ge. (b) The three peaks have been moved to have their maxima at the same position and their height has been rescaled. Symbols have the same meaning as in (a). The solid line is a gaussian obtained with the parameters from the analytic theory (5).

them. In their calculations, de Gironcoli *et al.* (1991) obtained a 4% upward bowing from their *ab initio* calculations.

In Figure 4.4, I show the next-nearest-neighbor distance for all the possible triplets where the solid lines are the theory, obtained from Equation (4.8), and the solid symbols are from the simulation. As noted in section 4.1, all the curves have the same slope and divide in two groups. I have not found any experimental data on these quantities nor any other calculations. But as calculations and experiments performed on  $Ga_xIn_{1-x}As$  are in very good agreement with this theory (Thorpe and Cai, 1992b), one expects the same in the binary semiconductor alloys.

### 4.3 Effect of amorphisation

To understand the effect of amorphisation on the length-mismatch problem, one notes that the strain energy introduced by the length mismatch between Si and Ge is much smaller than the strain energy due to the amorphisation. One would therefore expect the two phenomena to be largely independent of each other since the tetrahedral topology is conserved. The effects of each kind of disorder can then be simply added, at least to a first order approximation. We can see that there is no correlation between the two effects by computing the strain energy due to the length mismatch in the amorphous network. Figure 4.5 compares this energy with the one predicted by Equation (4.7). I subtracted the strain energy due to amorphisation, leaving only the term due to the length-mismatch distortions. The latter is about two orders of magnitude lower than the strain energy due to amorphisation.

It is useful to compare the magnitude of the disorder induced by the

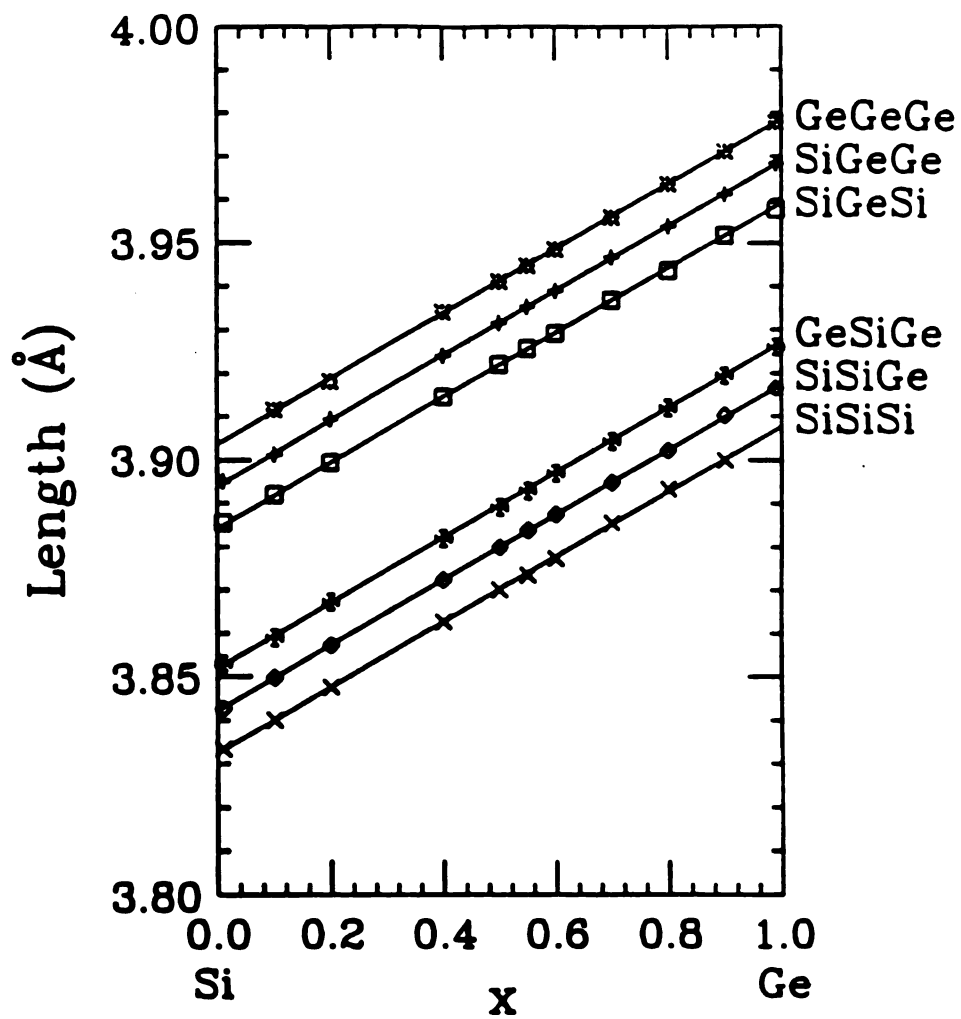


Figure 4.4: The next-nearest-neighbor distance in  $\text{Si}_{1-x}\text{Ge}_x$ . Solid lines are the analytical results using the theory and the symbols are from computer simulations using the Kirkwood potential.

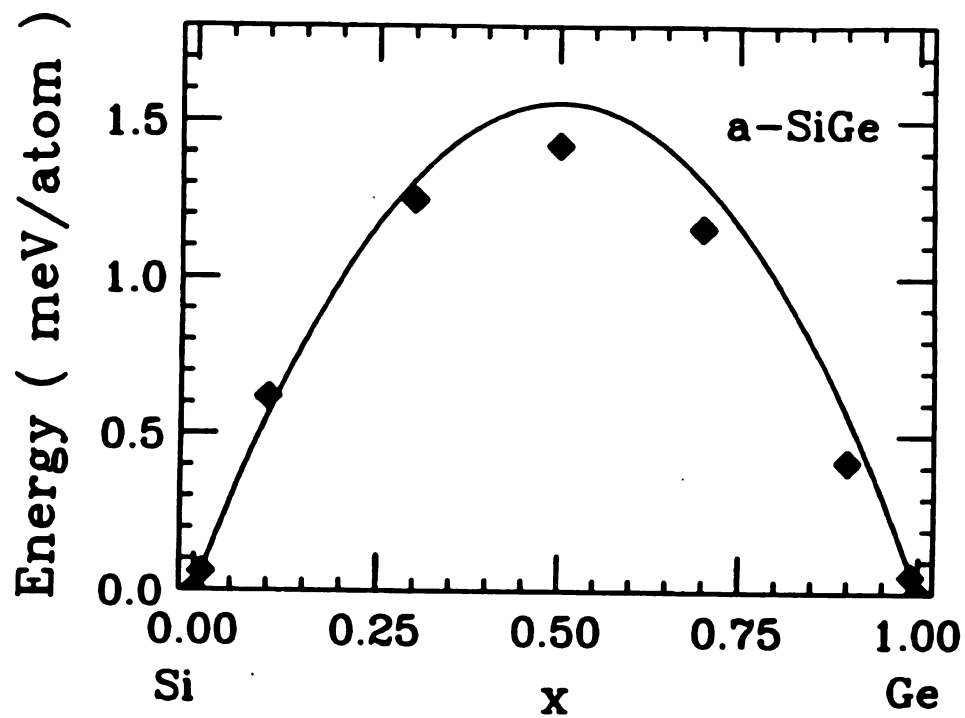


Figure 4.5: The strained energy due to length mismatch in  $a\text{-Si}_{1-x}\text{Ge}_x$ . The (large) component due to amorphisation has been subtracted. The symbols are from computer simulation using the Kirkwood potential and the line is the analytic result.

length-mismatch and the amorphisation. The comparison is made for  $\alpha$ -Si<sub>1-x</sub>Ge<sub>x</sub> and the numbers are obtained from the relaxation of a giant supercell containing eight times the 4096 atom amorphous supercell recently constructed by Wooten using the Wooten, Winer and Weaire algorithm (1985; and Wooten and Weaire, 1987). I used a giant supercell to increase the probabilities of finding specified triplets at low  $x$  and  $(1 - x)$ . This structure is perfectly tetravalent and can be considered as a *perfect* amorphous structure, containing no dangling bonds. The cell has been relaxed with the Kirkwood potential using the parameters described in the previous section. Because the length mismatch in SiGe is small, about 4%, and the network is relatively floppy, the values of the structural quantities in crystalline SiGe random alloy do not have a large variance. On the other hand, the amorphisation entails considerable disorder leading to wide distributions. For example, in Table 4.2 we see that the deviation of the bond length Si-Si in crystalline Si<sub>0.5</sub>Ge<sub>0.5</sub> is 0.2% while it is ten times larger (2.0%) in the pure  $\alpha$ -Si. Similarly, the standard deviation for the bond angle is 11° in the amorphous network and only 0.77° in crystalline Si<sub>0.5</sub>Ge<sub>0.5</sub>.

What effects should the amorphisation process have on the theory presented in section 4.1? Because the equations for the partial nearest-neighbor distances are linear, depending only on the average lengths, they remain valid here and the mean nearest-neighbor distance in  $\alpha$ -Si is identical to the crystalline one. The only question to settle is whether or not  $\alpha^{**}$  will remain the same. From the definition, the topological rigidity constant represents the force needed to open up a cage in the equilibrium structure. In the harmonic approximation which constitutes the basis for this theory,  $\alpha^{**}$  should remain essentially unchanged as long as the coordination stays fourfold. Indeed, Figure 4.6 shows that the theoretical

predictions are well supported by the simulation.

The next-nearest-neighbor distances must be examined carefully since they involve second-order equations. In the pure length-mismatch problem, one can neglect the deviations from the perfect tetrahedral angle and obtain a very good agreement with simulations and experiments. In the amorphous material, the angular deviations are important and one cannot neglect them.

For a triplet  $ijk$  in pure  $\alpha$ -Si, the next-nearest-neighbor distance is given by

$$L_{ik}^{nnn} = L_{ij} \sin \phi^A + L_{jk}^{nn} \sin \phi^B \quad (4.12)$$

where  $L_{ij}$  and  $L_{jk}$  are nearest-neighbor distances and the angles  $\frac{\pi}{2} - \phi_A$  and  $\frac{\pi}{2} - \phi_B$  are the angles between the nearest-neighbor vectors and the next nearest bond  $ik$ .

Taking the average over all the triplets and neglecting correlations between angle and bond length, we obtain

$$\langle L^{nnn} \rangle = 2L_{SiSi}^0 \langle \sin \phi \rangle \quad (4.13)$$

since in a tetravalent amorphous system to first order the mean length is the ideal length in this problem. Using the fact that, in this system, the distribution of tetrahedral angles is almost gaussian (Mousseau and Lewis, 1990), we need only the first two moments:

$$\langle \phi \rangle = \frac{\langle \theta \rangle}{2} \quad (4.14)$$

where  $\theta$  is the bond angle. If the angular distortions are large enough, we cannot approximate  $\langle \sin \phi \rangle$  by  $\sin \langle \phi \rangle$ , and we must include higher order terms. Expanding around  $\langle \phi \rangle$ , we obtain

$$\langle \sin \phi \rangle = \sin(\langle \phi \rangle + \delta\phi)$$

Table 4.2: Values of various quantities in the  $\alpha$ -Si network and in the crystalline binary semiconductor  $\text{Si}_{0.5}\text{Ge}_{0.5}$ .

	$\text{Si}_{0.5}\text{Ge}_{0.5}$	$\alpha$ -Si
$\Delta r_{\text{Si:Si}}$ (Å)	0.005	0.050
$\langle \theta \rangle$ (deg)	110.05	109.17
$\Delta\theta$ (deg)	0.77	11.

$$= \sin \langle \phi \rangle \cos(\delta\phi) + \cos \langle \phi \rangle \sin(\delta\phi). \quad (4.15)$$

Averaging over all angles, the second term on the right-side vanishes and we can expand the cosine:

$$\begin{aligned} \langle \sin \phi \rangle &= \sin \langle \phi \rangle \langle \cos(\delta\phi) \rangle \\ &= \sin \langle \phi \rangle e^{-\frac{1}{2}\langle (\delta\phi)^2 \rangle} \\ &= 0.9954 \sin \langle \phi \rangle \\ &= 0.9935 \sin \phi_0 \end{aligned} \quad (4.16)$$

taking the mean angle and the deviation for  $\alpha$ -Si values of  $\alpha$ -Si given in Table 4.2.  $2\phi_0$  is the tetrahedral angle in a perfect diamond lattice. Using (13), we obtain  $\langle L^{nnn} \rangle = 3.807$  instead of  $L^{nnn} = 3.833$  given by  $\sqrt{8/3} L_{\text{Si:Si}}^0$ . This change can seem insignificant but it is easily perceived in computer simulations as shown in Figure 4.6, which should be compared with the crystalline result in Figure 4.1.

When the length mismatch is superposed on the amorphisation, Equation (4.9) remains valid except that the average next-nearest-neighbor distance is now given by Equation (4.13) where the bond length  $L_{\text{Si:Si}}^0$  is replaced by  $L_e^{nn}$  obtained from Végard's law,

$$L_e^{nn} = 0.9935 \sqrt{8/3} \left( (1-x)L_{\text{Si:Si}}^0 + xL_{\text{Ge:Ge}}^0 \right), \quad (4.17)$$

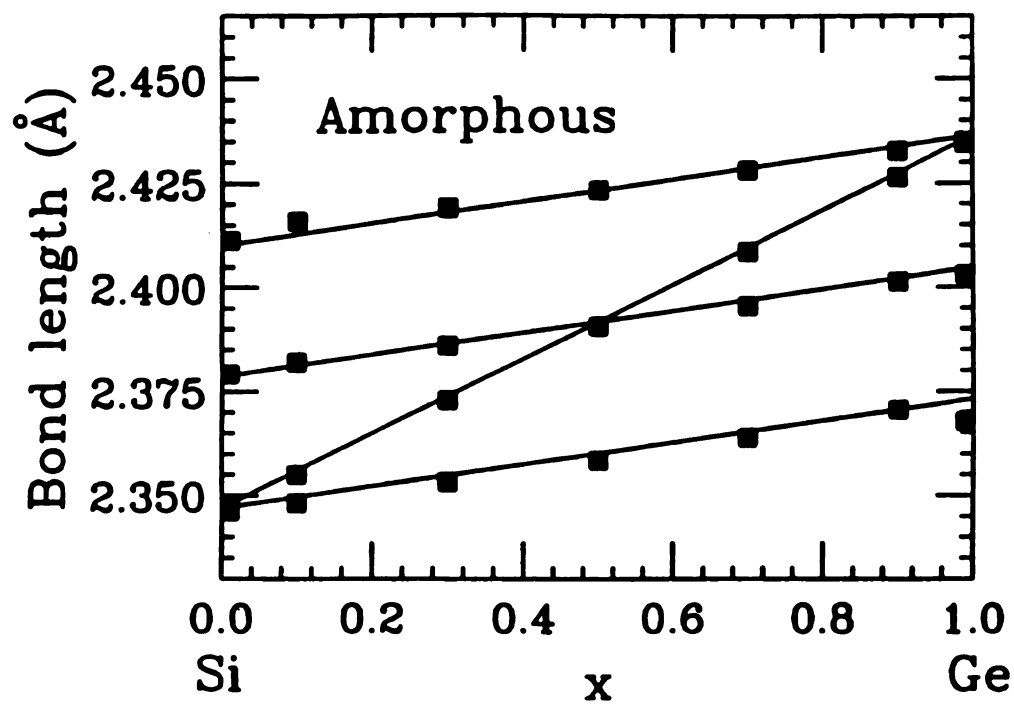


Figure 4.6: The nearest-neighbor distance for  $a\text{-Si}_{1-x}\text{Ge}_x$ . The symbols are from simulations using the Kirkwood potential and the lines are the analytic theory.

leading essentially to a downward displacement of the six next-nearest-neighbor curves for a small mismatch. We can also neglect the corrections in the second term on the right-hand side of (4.8) since they are already very small compared with the average next-nearest-neighbor distance. Figure 4.7 shows the simulation and theoretical results. There is some noise in the computer data, due to the wide distribution but the agreement with the theory is excellent.

These results *contradict* EXAFS experiments performed on  $a\text{-Si}_{1-x}\text{Ge}_x\text{:H}$  by Incoccia *et al.* (1985) and repeated using a different analysis method but with the same results by Nishino *et al.* (1988). Both groups observed that the Ge-Ge and Si-Ge bond lengths remained *unchanged* as the composition  $x$  changes. Such a behavior is highly surprising and not believable. In order to follow Végard's law, the Si-Si nearest-neighbor distance would also have to remain constant, indicating a topological parameter  $a^{**} = 1$ , meaning a completely floppy network. The only way to bring such freedom to the amorphous network is via the introduction of large amounts of hydrogen. By saturating dangling bonds, the hydrogen atoms decrease the effective coordination of the network. The next chapter will examine this problem in more detail; besides, more recent experiments have shown that the uncertainties in the measurement are much too wide presently to challenge this theory (Matsuura *et al.*, 1991)

## 4.4 Conclusion

The simple analytical model presented here gives results which are in general agreement with *ab initio* calculations. For the random crystalline solid solution, the calculations by de Gironcoli *et al.* (1991) give even the wrong curvature for the mean length emphasizing that it would require a more sophisticated theory

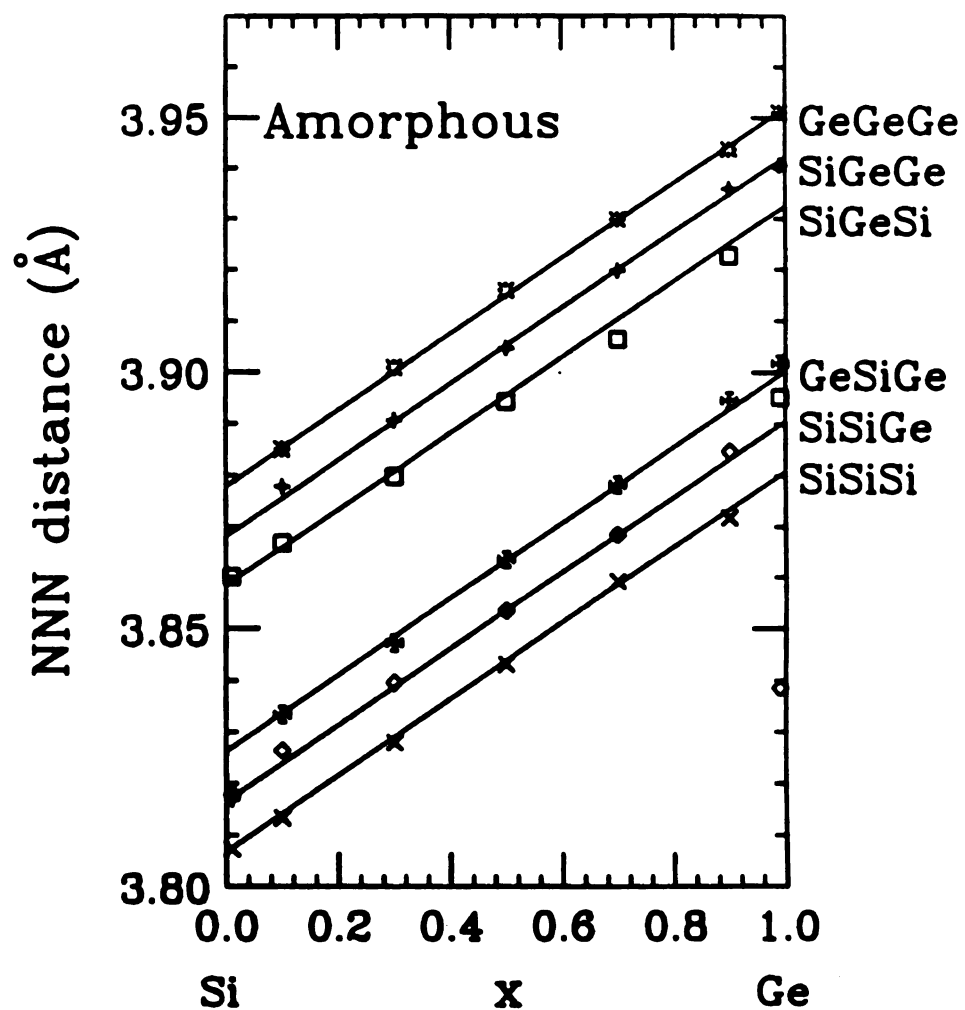


Figure 4.7: The mean next-nearest-neighbor distances in  $a\text{-Si}_{1-x}\text{Ge}_x$ . The solid lines are the analytic results and the symbols are from simulations using the Kirkwood potential.

than is presently available to obtain the small deviations away from Végard's law.

This theory provides a simple understanding of the mean partial nearest and next nearest-neighbor lengths, in the absence of bowing. To go beyond this and to be able to predict the bowing with any confidence is a formidable task. This theory predicts that the width of the distributions of nearest-neighbor distances will be all identical; a prediction which is robust when compared with parameter-free simulations and I also show that all the next-nearest-neighbor distances have the same slope. There are very few experimental results on these alloys; the calculations and theory are consistent with (Matsuura *et al.*, 1991).

Finally, contrary to experimental results obtained a few years ago (Incoccia *et al.*, 1985; Nishino *et al.*, 1988), I predict that the amorphisation will have *no* effect on the length mismatch problem, when all the atoms are tetravalently bonded. The strain energy produced by the amorphisation is larger by two orders of magnitude, compared to the strain energy produced by the alloying. The length mismatch disorder can be treated as a perturbation on top of the disorder already present in the amorphous network. This leads to very similar results for the mean lengths to those found in the corresponding crystalline alloy. The widths of the length distributions, for nearest neighbors, is dominated by the distortions produced by the amorphisation.

# Chapter 5

## About EXAFS Results

With the development of EXAFS techniques, there has been a renewed interest on the part of experimentalists to examine the local structure of disordered materials. Some of the most exciting work in the past decade has been on crystalline semiconductor alloys (Balzarotti, 1987; Podgorny *et al.*, 1985); both III-V and II-VI compounds. Many different materials have been examined at various compositions and a very consistent picture emerges. The mean bond length of chemically specific pairs, for example Ga-As bonds in  $\text{Ga}_x\text{In}_{1-x}\text{As}$ , is composition dependent but much less strongly so than the *overall* mean bond length. The overall mean bond length, or unit cell size, can be obtained independently from X-ray diffraction experiments, and is always found to be close to linear (Végar's law, 1921) in agreement with the result expected if a weighted average of the different bond lengths is found using the EXAFS results. The weaker composition dependence of the chemically specific mean bond lengths is due to the soft nature of the zincblende lattice.

The situation is very different for binary semiconductor alloys made from the group IV elements Si, Ge and Sn. Recent experimental EXAFS results involv-

ing the alloy  $\text{Si}_{1-x}\text{Ge}_x$  have shown that the Ge–Ge and Ge–Si mean bonds lengths are *independent* of the composition  $x$ , for *both* crystalline and amorphous alloys. Similar composition independent bond lengths results have also been reported for SiC and GeSn alloys, but these systems are more complex because of the likelihood of some local graphitic bonding of the C in SiC, and the possibility of local metallic bonding associated with the Sn in GeSn. This chapter will therefore try to understand the divergence between experiment and theory for Si–Ge alloys.

## 5.1 Assumptions

In the previous chapter, I have extended the theoretical description of the local structure of crystalline, and with minor changes, amorphous binaries to group IV alloys. Recent EXAFS measurements on *a*-SiGe and *c*-SiGe compounds (Kajiyama *et al.*, 1992; Incoccia *et al.*, 1985; Nishino *et al.*, 1988) have shown quite severe disagreement with both CT theory and simulation predictions. The goal of this paper is to examine these discrepancies between experimental EXAFS work on one side and theoretical and simulation work on the other, as well as to propose a new structural model that may resolve these discrepancies.

In order to solve the set of equations for the partial lengths, using a Kirkwood potential (see chapters 2 and 4), I have used two major assumptions that are worth repeating here:

(A) The elastic constants are the same for all interactions. The topological rigidity parameter  $\alpha^{**}$  is not very sensitive to changes in the local force constants, and the elastic constants for the pure Si and Ge differ by about 20%, which will only produce a hardly perceptible bowing of the Z-plots to be discussed later.

(B) The length  $L_{\text{SiGe}}^0$  is the arithmetic average of the two other partial lengths.

The additivity of atomic radii is found to hold generally in the case of semiconductors.

## 5.2 Comparison between theory and experiment

The theory predicts an average length following Végard's law, and the three parallel partial lengths varying linearly with the concentration  $x$ . As I have commented earlier, similar straight line behavior is predicted and has been seen experimentally in ternary III-V and II-VI compounds (Balzarotti, 1987). For the binaries, there exists a few experimental papers on SiGe alloys, using either X-ray measurements or EXAFS on the Ge atoms. Kajiyama *et al.* (1992) measured the mean Ge-Ge and Ge-Si bond lengths in bulk  $c$ -SiGe alloys; Incoccia *et al.* (1985) and Nishino *et al.* (1988), in bulk  $a$ -SiGe alloys; and Matsuura, Tonnerre and Cargill (1991) measured these lengths in SiGe/Si(100) films. There has also been some work on  $a$ -GeSn and  $a$ -SiC alloys; both by the same group (Pascarelli *et al.*, 1992a and 1992b). However, since Sn and C can have variable bonding (Sn can have local metallic bonding and C can have local graphitic bonding), conclusions in these cases are more difficult to draw and will not be directly addressed here. Moreover, because the CT theory applies only to the bulk, I will concentrate on the three first papers (Kajiyama *et al.*, 1992; Incoccia *et al.*, 1985; and Nishino *et al.*, 1988). Nevertheless note that *all* these experiments cited above on SiGe, SiC and GeSn alloys are consistent with the result that there is *no* composition dependence of the chemically specific bond lengths, for *both* crystalline and amorphous samples. In the three papers on SiGe, both the Ge-Ge and the Ge-Si mean nearest-neighbor bond lengths have been measured using Ge EXAFS, but *not* the Si-Si bond length. All of these experiments agree on the fact that the measured

mean bond lengths do *not* vary with composition. The exact bond length varies only slightly and within a  $0.02\text{\AA}$  error bar from one paper to the other, but the conclusions are the same: the Ge-Ge and Si-Ge nearest-neighbor distances are independent of concentration. Since the maximum variation from the length predicted by the theory is  $0.026\text{\AA}$ , the predictions of this theory are at the limit of the error bars.

Looking at Equation (4.3), we see that the only way to obtain flat curves for Ge-Ge and Ge-Si bond lengths is for the network to be *floppy*, i.e. to have  $a^{**}$  very close to 1. Even relaxing the condition where I have used the same force constants for the three different kinds of pair interactions, one finds in the low concentration (single defect) limit (Thorpe, Jin and Mahanti, 1989).

$$\langle L_{SiGe} \rangle = L_{SiSi}^0 + x \left[ \frac{(1 - a^{**})\alpha_{SiGe}}{(1 - a^{**})\alpha_{SiSi} + a^{**}\alpha_{SiGe}} \right] (L_{SiGe}^0 - L_{SiSi}^0), \quad (5.1)$$

where I have introduced different central force constants  $\alpha_{SiSi}$  and  $\alpha_{SiGe}$  for the Si-Si and Si-Ge bonds. Different angular force constants can be incorporated by adjusting  $a^{**}$ . I have also *not* assumed that  $L_{SiGe}^0 = (L_{SiSi}^0 + L_{GeGe}^0)/2$ . So, independently of the values of the force constants, we can only obtain a flat EXAFS curve (i.e. independent of composition  $x$ ) with  $a^{**} = 1$ . The first way to achieve this result is to affect the value of  $a^{**}$  by varying the ratio  $\beta/\alpha$ . From Equation (2.31), we have the behavior of  $a^{**}$  as a function of the ratio of the angular force  $\beta$  to the bond stretching force  $\alpha$  from CT. To obtain  $a^{**} = 1$ , we need a ratio  $\beta/\alpha$  that is essentially zero, and certainly much smaller than the usual range 0.1 - 0.2. In order to explain their results, Kajiyama *et al.* (1992) suggested that the angular term  $\beta$  is anomalously small compared to the stretching term  $\alpha$  but for this explanation to be valid would require a ratio  $\beta/\alpha$  of less than 0.05 which would lead to a much weakened shear modulus. Direct

measurements of the elastic constants in SiGe solid solutions grown by evaporation in the absence of hydrogen show no such weakening (Bublik *et al.*, 1974). It would be interesting to repeat these experiments on hydrogenated samples. Also indirect measurements like Raman spectra can be well reproduced theoretically using the same force constants for all bonds and taking into account only the mass differences (Yndurain, 1978). The Raman peak at about  $470 \text{ cm}^{-1}$  in pure silicon can be rescaled using only the appropriate reduced mass to the Ge peak at  $280 \text{ cm}^{-1}$  and to the new Si-Ge peak centered at about  $380 \text{ cm}^{-1}$ , all to within 5 percent, confirming that the force constants are close for the three kinds of bonds. The samples used for the Raman scattering were polycrystalline and should not contain hydrogen. It is therefore very unlikely that any appreciable change in the ratio  $\beta/\alpha$  occurs, and I dismiss this possibility. One does however expect a softening of the elastic constants in hydrogenated samples —not due to the weakened angular forces— but due to the mechanical degradation of the network caused by the presence of large amounts of hydrogen.

In their paper on *c*-SiGe alloys, Kajiyama *et al.* (1992) measured the lattice constant as a function of the composition  $x$  using X-ray diffraction. It is worth mentioning that previous measurements showed a small deviation from Végard's law of less than 4% (Dismukes, Ekstrom and Paff, 1964) compared with the much larger 16% presented in Kajiyama's paper. Using the (exact) sum rule

$$\langle L \rangle = (1 - x)^2 \langle L_{SiSi} \rangle + 2x(1 - x) \langle L_{SiGe} \rangle + x^2 \langle L_{GeGe} \rangle, \quad (5.2)$$

and the values for  $\langle L_{Si-Ge} \rangle$  and  $\langle L_{Ge-Ge} \rangle$  obtained by EXAFS, it is possible to predict the expected value of  $\langle L_{SiSi} \rangle$ . If Végard's law is exactly obeyed, then (5.2) gives  $\langle L_{SiSi} \rangle = L_{SiSi}^0$  which is also concentration independent. However

the measured X-ray diffraction data (Kajiyama *et al.* 1992) can be fit with

$$\langle L \rangle = (1 - x)L_{SiSi}^0 + xL_{GeGe}^0 - \theta x(1 - x), \quad (5.3)$$

where  $\theta$  is the *bowing* parameter. From (5.2)

$$\langle L_{SiSi} \rangle = L_{SiSi}^0 - \theta \frac{x}{1 - x} \quad (5.4)$$

showing that the composition dependence of  $\langle L_{SiSi} \rangle$  will become large as the Ge composition  $(1 - x)$  increases, as shown in Figure 5.1. I emphasize that the result (5.4) is exact and independent of any model. It would be useful to have EXAFS experiments on the Si available so that this quantity would be available to provide an important internal consistency check. It would be quite unusual if the length of the Si-Si bond decreased upon the introduction of the larger Ge. Theoretically this behavior has been predicted in some metallic alloys (e.g. AuAg) where it is attributed to the effects of variation of electronic charge density. However, we cannot use the same argument here since Si and Ge are in the same column of the periodic table and charge transfer effects are negligible. It is difficult to justify the Ge-Ge and Si-Ge bond lengths remaining so constant compared with such a marked change in Si-Si bond length, although such an occurrence would not violate any geometrical constraints.

Another way to increase floppiness in the alloy, would be to *decrease* the average coordination number of the atoms. This is a likely explanation since in all three experiments (Kajiyama *et al.*, 1992; Incoccia *et al.*, 1985; Nishino *et al.*, 1988), the sample preparation took place in the presence of *hydrogen*. Hydrogen is a network terminator, and attaches itself to one (or more) of the four bonds formed by the Si and Ge ions. As a consequence its main effect on the network is to decrease the effective coordination and hence the rigidity of the network.

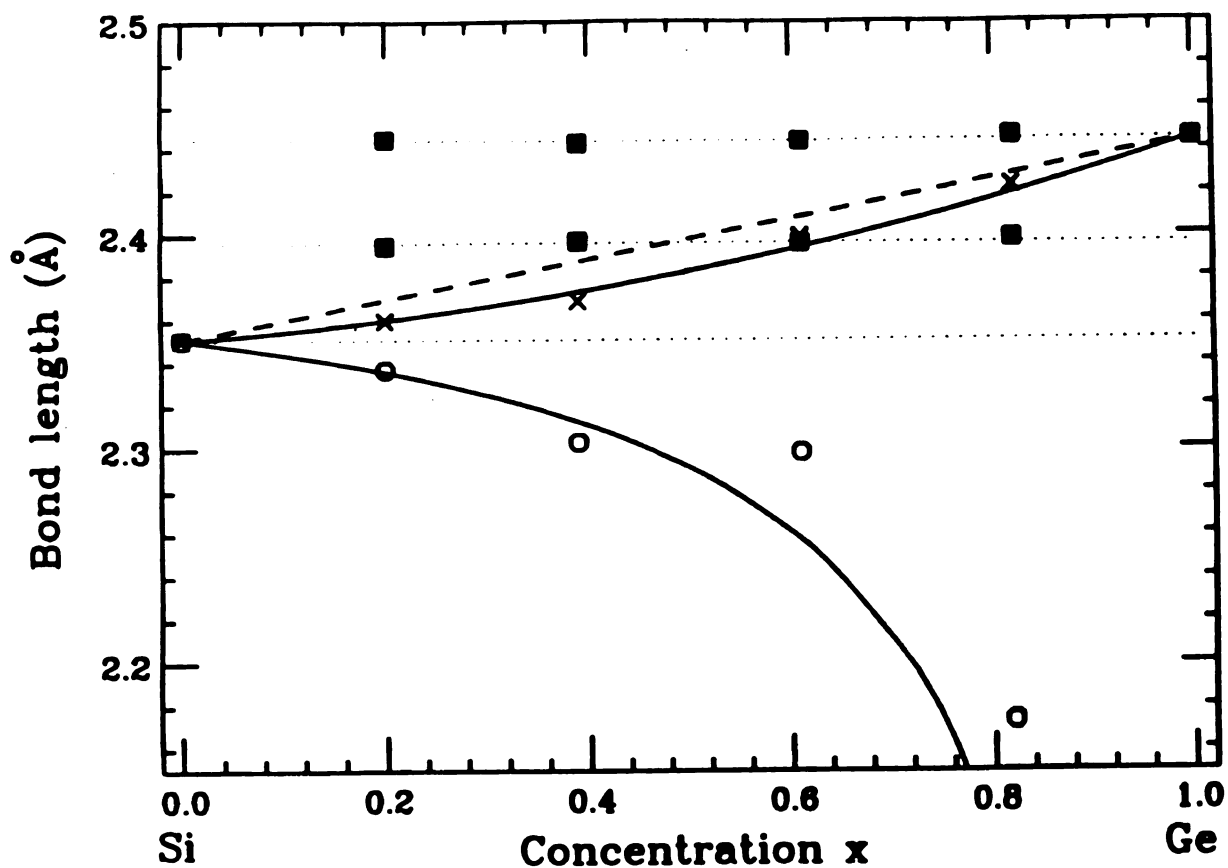


Figure 5.1: A  $Z$ -plot from the Kajiyama *et al.* (1992) experiments. The Ge-Ge and Si-Ge bond lengths measured by EXAFS are shown by full squares and the average length obtained by X-ray diffraction, by crosses and the dashed line is Végard's law. The Si-Si bond length (empty circles) was deduced using the definition of the average lengths. The solid line is the quadratic relation given in the text and using  $\theta = 0.06\text{\AA}$ . The horizontal dotted lines are guides to the eye.

### 5.3 Structural model

I have examined the effect of the inclusion of hydrogen on the topological rigidity of the network. Hydrogen is a terminator that makes a single bond to either Si or Ge, both of which remain four-fold coordinated. Hydrogen that goes in interstitially or as molecular hydrogen is irrelevant to the mechanical properties of the network and will be ignored here. The method used here gives an estimate for the variation of  $\alpha^{**}$  with the degree of hydrogenation. The numerical method used is the same as the one presented in the previous chapter where the Kirkwood potential is used and the static relaxation is accomplished using a conjugate-gradient algorithm. I have introduced hydrogen into the network by cutting a bond and inserting *two* hydrogens. This is an unphysical procedure as the Si-H and Ge-H bonds lengths are too large (about 1.5Å) compared with 2.35 and 2.43Å for Si-Si and Ge-Ge bonds respectively, for this to occur. Nevertheless, since I consider the hydrogenated bond as absent, this procedure does encompass the main effects of hydrogen which is to act as a terminator and hence lower the mean coordination of the network (He and Thorpe, 1985). In the simulations, the bonds are removed randomly, but never attach more than two hydrogens to a Si or Ge atom. This procedure can be accomplished with equal computational facility for both the crystalline and amorphous networks.

It is possible to obtain the limits of  $\alpha^{**}$  analytically, i.e. the fully coordinated and the floppy limit when the rigidity vanishes. In between these two limits, one has to resort to computer simulations. The four-fold coordination limit of  $\alpha^{**}$  is found from Equation (4.4) to be 0.707 for a ratio  $\beta/\alpha = 0.20$ . The floppy limit is obtained by looking at the rigidity percolation transition, using a mean field approach. This has been used elsewhere (Thorpe, 1983) and has been shown to be

very accurate. The network becomes floppy when  $F$ , the number of zero frequency modes is greater than zero (Thorpe, 1983). The number of zero frequency modes is equal to the number of degrees of freedom minus the number of constraints. Because I don't allow more than two hydrogens per Si or Ge, the whole network remains fully connected. Counting 4/2 central force and 5 angular constraints per Si and/or Ge, and 1/2 central force constraint for each H in  $\text{Si}_{1-x}\text{Ge}_x\text{H}_y$ , one gets

$$\begin{aligned} F &= 3N(1+y) - N[2+5] - Ny \left[ \frac{1}{2} \right] \\ &= N \left( \frac{5}{2}y - 4 \right). \end{aligned} \quad (5.5)$$

For  $F = 0$ ,

$$y_p = \frac{8}{5} = 1.6 \quad (5.6)$$

which corresponds to a  $y_p/(1+y_p) = 8/13 = 62\%$  atomic fraction of hydrogen.

The essential idea is that each hydrogen atom terminates a bond and has no other interactions. Since hydrogen does not participate in connecting the network together, being a terminal bond, one can consider it as being absent for most purposes. The simulation procedure consists then in removing bonds at random in  $c$ -SiGe or  $a$ -SiGe solid solutions to obtain the topological rigidity parameter  $a^{**}$  associated with a certain concentration  $x$  and  $y$ . This is done by computing the various mean distances, as in Figure 5.2 and fitting the resulting straight line  $Z$ -plot found with the single unknown parameter  $a^{**}$ . This is a somewhat indirect procedure, but appropriate in the present context. Indeed it is probably the best way to obtain the topological rigidity parameter in amorphous networks. The quantity of hydrogen needed to take the topological rigidity  $a^{**}$  of the lattice to unity (i.e. the floppy limit) would be extremely large (62% atomic fraction) and it is difficult to imagine such amounts of hydrogen distributed evenly throughout the sample.

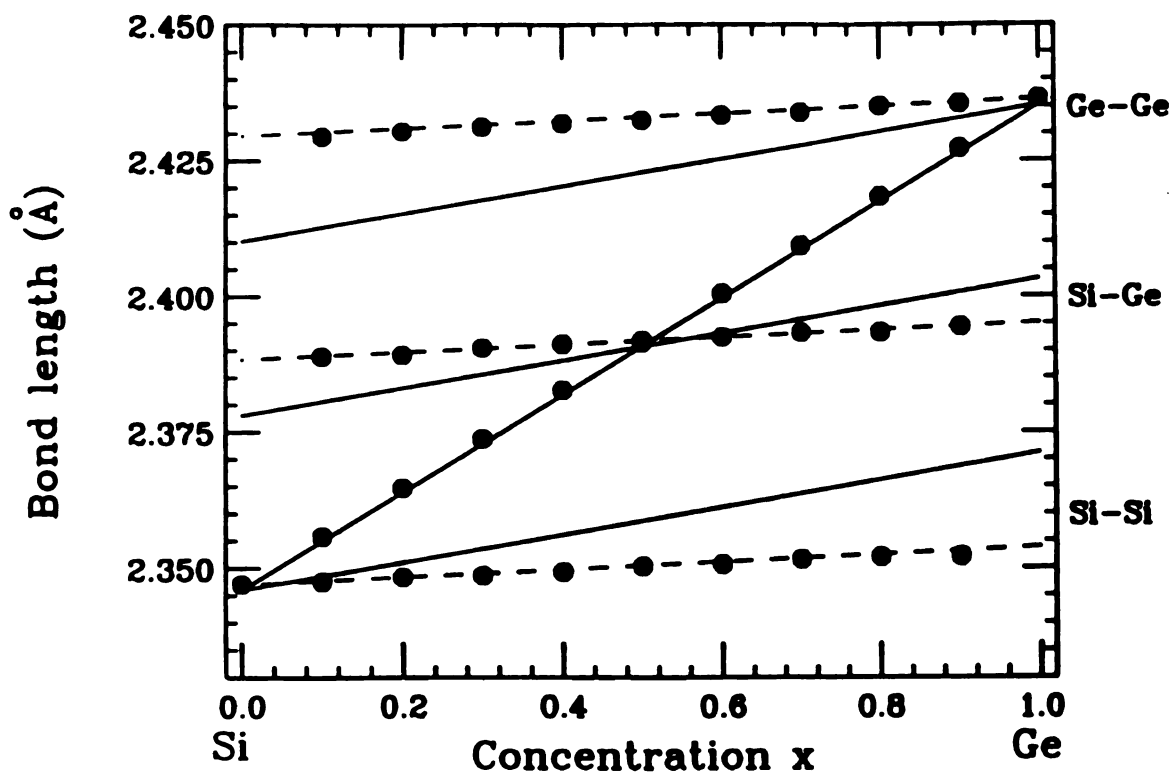


Figure 5.2: A  $Z$ -plot for  $c\text{-Si}_{1-x}\text{Ge}_x\text{:H}_\gamma$ , from a computer relaxation of a crystalline alloy. The solid lines correspond to a topological rigidity parameter  $a^{**} = 0.707$  and the dashed lines are a fit to the simulation results (shown by solid circles) where  $y = 1.0$  and  $a^{**} = 0.923$ . The fraction of hydrogen is determined by assigning two hydrogens to each removed bond.

The bulk calculations for Figure 5.3 have been made for randomly removed bonds in crystalline as well as amorphous cells of  $2^{15} = 32,768$  atoms with periodic boundary conditions, constructed by Wooten (1991) following the Wooten, Winer and Weaire algorithm (1985). The Wooten sample contained  $2^{12} = 4,096$  atoms but was replicated 8 times to form a larger cube. I then decorated the full lattice randomly with Si and Ge atoms following the procedures described in chapter 3. In the previous chapter I have shown, using computer simulations, that since the connectivity is the same in the crystalline and *perfect* amorphous Si structure, the topological rigidity  $a^{**}$  is identical in both systems. Moreover, as the strain due to alloying is about two orders of magnitude smaller than the strain due to amorphisation, one can treat the former as a perturbation and use the CT theory developed for crystalline alloys. The results for all the partial lengths in both the amorphous and crystalline structures are always the expected set of three parallel straight lines that can be fit with the single parameter  $a^{**}$ . From computer simulations, I find that the topological rigidity parameter  $a^{**}$  is linear in the mean coordination  $\langle r \rangle$  of the network and so can be written

$$a^{**} = \frac{5}{8}[(4 - \langle r \rangle) + a_0^{**}(\langle r \rangle - 2.4)] \quad (5.7)$$

where  $\langle r \rangle = 4 - y$  is the mean coordination of the network (ignoring the hydrogen), and the topological rigidity parameter  $a^{**} = a_0^{**} = 0.707$  when no hydrogen is present.

The precise way in which the hydrogen is distributed in the network is irrelevant as far as the topological rigidity is concerned, as long as it is homogeneous on some reasonable length scale. It is therefore possible to think of a physically more plausible model that could result in the same amount of floppiness in the network. I have studied the topological rigidity for *finite* pieces of crystalline

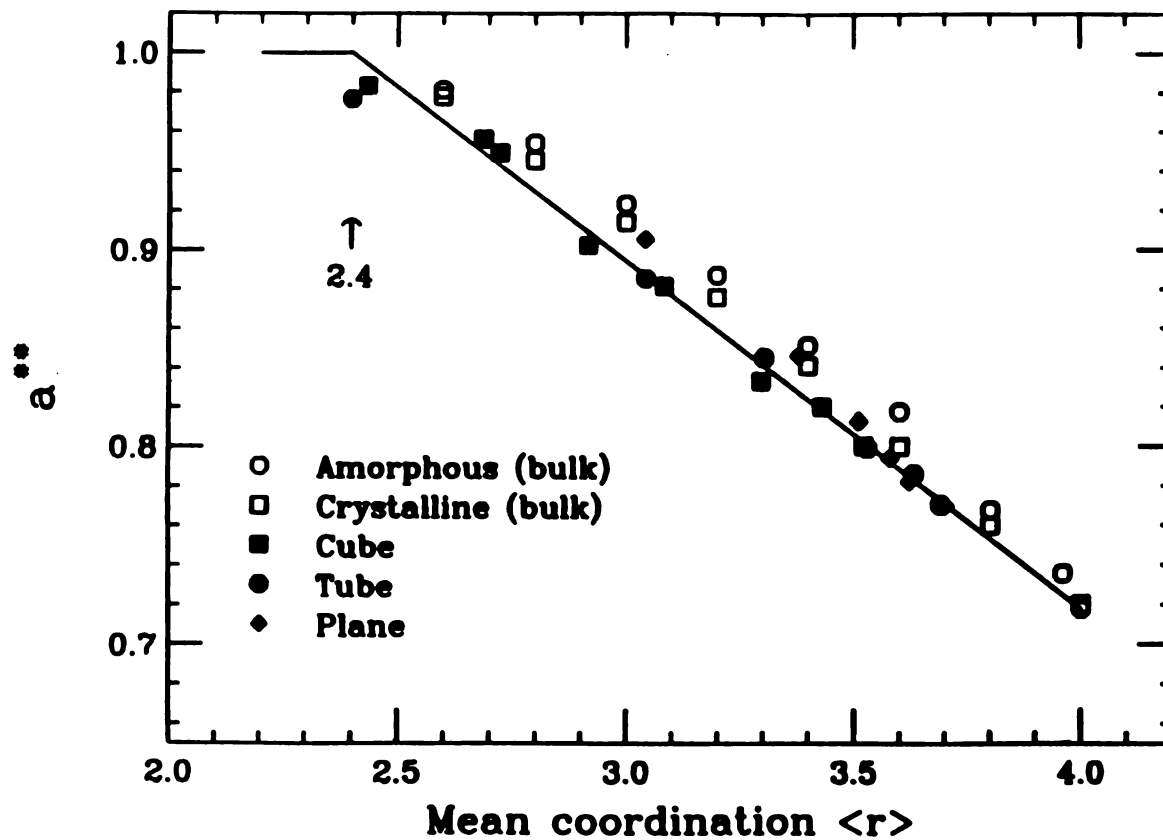


Figure 5.3: The variation of the topological rigidity parameter  $a^{**}$  with the mean coordination  $\langle r \rangle$  in SiGe alloys. The open symbols are for simulations with periodic boundary conditions (bulk) and the solid symbols for (clusters) with free boundary conditions. The solid line is a linear interpolation between the floppy limit  $a^{**} = 1$  and the  $a^{**} = 0.707$  for the perfect network, given in the text.

$\text{Si}_{1-x}\text{Ge}_x$  alloys of different sizes and shapes with free surfaces. The three shapes I used were cubic ( $l \times l \times l$ ), tubular ( $l \times l \times L$ ) and planar ( $l \times L \times L$ ), where  $l$  is a variable and  $L$  was fixed at  $54\text{\AA}$  which one can regard as infinite (Figure 5.4). There is no hydrogen implanted in these pieces. A physical realization of this situation would be that all the dangling bonds at the surface of these pieces are saturated with hydrogen. Again the topological rigidity parameter is extracted from the computer simulations by fitting the three parallel lines in the  $Z$ -plot like that in Figure 5.2 with the single unknown parameter  $a^{**}$ . We do indeed always obtain simple straight line  $Z$ -plots from the simulations on cubes, tubes and planes. The results in Figure 5.3 shows that the *geometry* of the defects is almost irrelevant to the topological rigidity  $a^{**}$ ; the mean coordination of the system uniquely determines its topological rigidity.

For these structures shown in Figure (3), the open surfaces are saturated with hydrogen. One is therefore free to choose any geometry, for a given concentration of dangling bonds, without affecting the mechanical rigidity of the network. A probable structural model would be one with a high density of thin planar cracks with a typical size of the two regions between cracks being about  $10\text{\AA}$  as deduced from Figure 5.5. A sketch of this model is presented in Figure 5.6. These cracks will be filled with hydrogen saturating the dangling bonds of the surfaces. Such a structure would be almost completely free of strain due to the alloying, resulting in an almost flat  $Z$ -plot, and would also respect the random proportion of Si-Ge to Ge-Ge bonds found experimentally from EXAFS (Kajiyama *et al.*, 1992; Incoccia *et al.*, 1985; Nishino *et al.*, 1988).

From this model, it is also possible to find the softening of the elastic constants. This is done by applying an external strain to the model and then

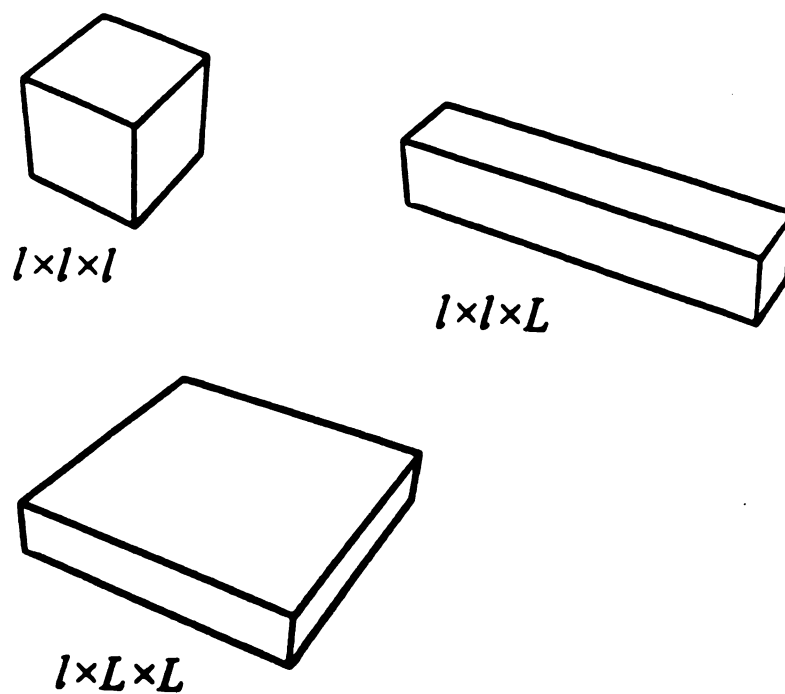


Figure 5.4: A sketch of the cube, tube and plane, where the long dimension  $L = 54\text{\AA}$  and the short dimension can be varied. The results obtained were not sensitive to the length  $L$  which can be regarded as infinite.

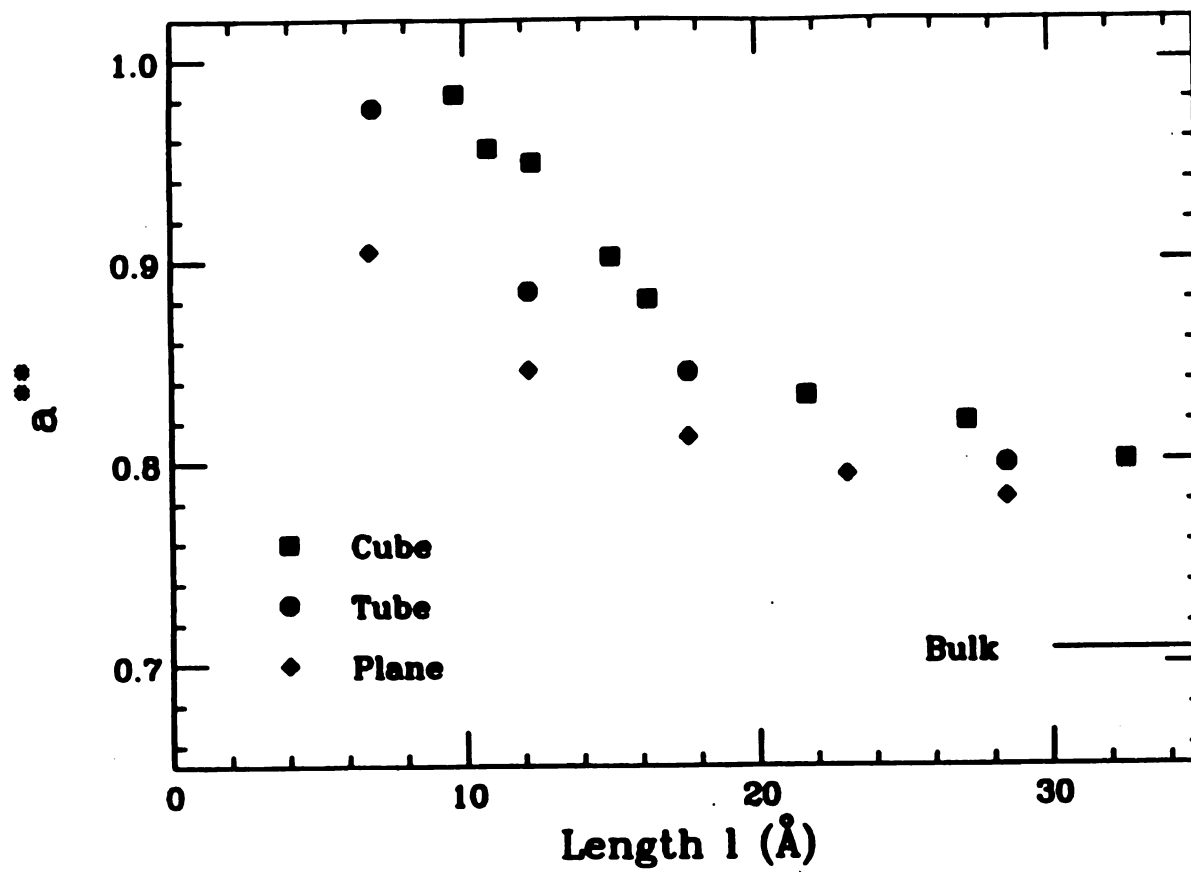


Figure 5.5: The variation of the topological rigidity parameter  $a^{**}$  with the length scale  $l$  for the cubes, tubes and planes shown in Figure 5.4. Here the large dimension  $L = 54 \text{ \AA}$  can be regarded as infinite.

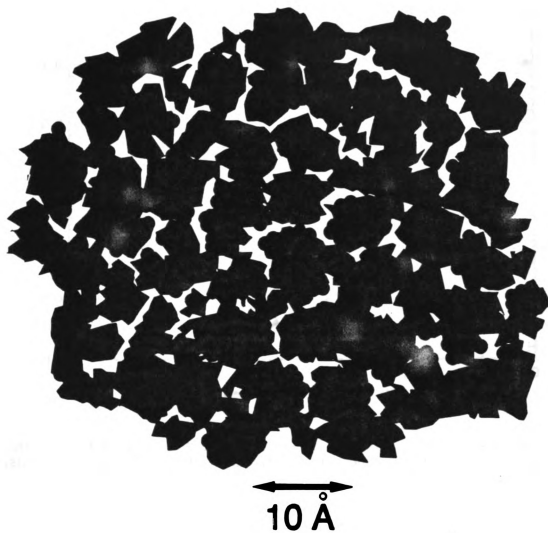


Figure 5.6: A sketch of the proposed structural model for SiGe alloys. The dark region is network and the open cracks are saturated with hydrogen to tie off the dangling bonds.

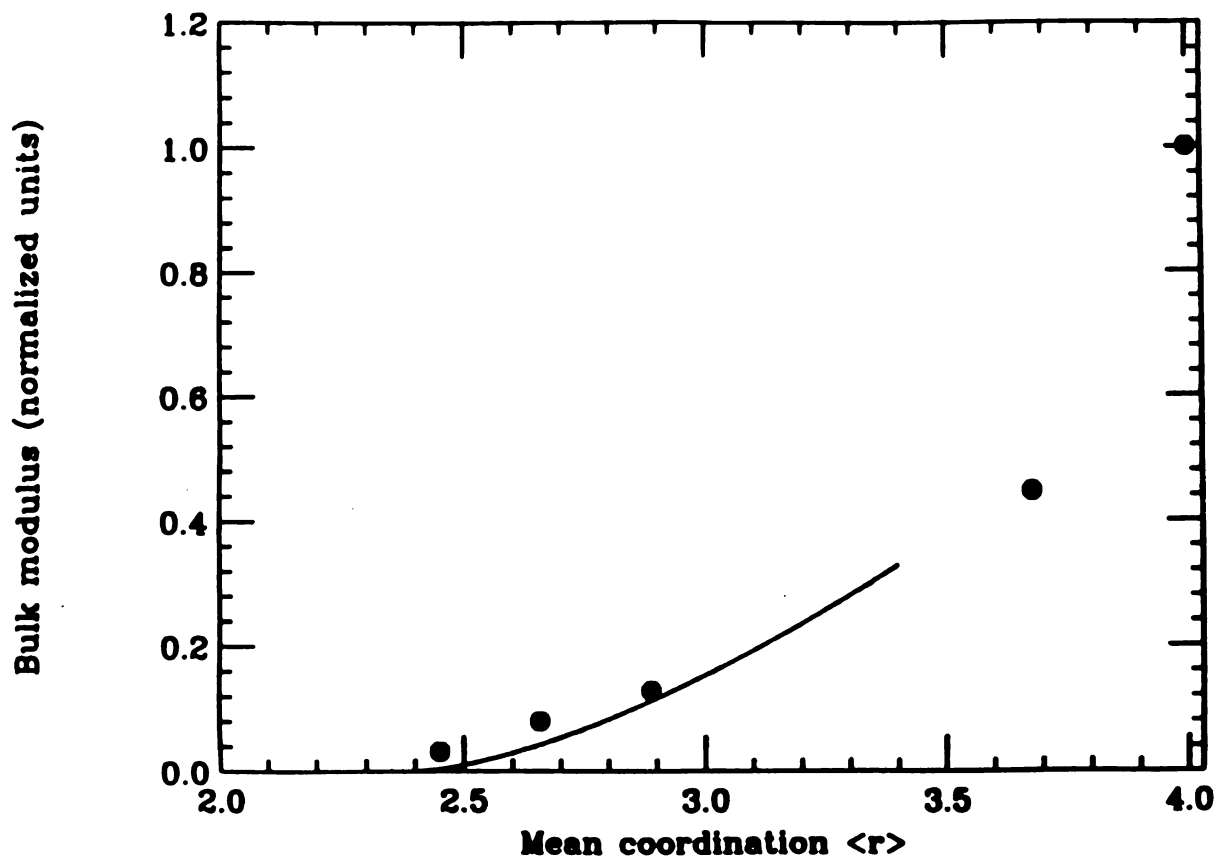


Figure 5.7: The variation of the bulk modulus  $B$  as a function of the mean coordination  $\langle r \rangle$  in  $c$ -SiGe:H. The solid symbols are from a simulation on a sample with planar cracks like that shown in Figure 5.6 and the solid line is Equation (5.8).

again minimizing the energy as before. The difference in the relaxed energy leads to the elastic moduli (He and Thorpe, 1985). Figure 5.7 shows how the bulk modulus varies with the effective coordination  $\langle r \rangle$ , in a bulk  $c$ -Si where *planar cracks* were introduced. These cracks were created the following way: in a crystalline cell of  $2^{15} = 32,768$  Si atoms, the position and direction of a plane were chosen at random; all the bonds that crossed the plane in a square area of side 2 unit cells around the origin of the plane were removed.

I can compare these results with an expression found by He and Thorpe

CE

(1)

th

in

nu

th

m

pr

w

ar

Se

th

E

**5**

H

ex

fo

G

th

II

un

th

by

(1985) for removing bonds at random. This expression is valid around the rigidity threshold, but is not supposed to be critical behavior,

$$B = 0.328 (\langle r \rangle - 2.4)^{1.5} \quad (5.8)$$

in units where the bulk modulus is 1 at full coordination ( $\langle r \rangle = 4$ ). Within the numerical accuracy, we see that the *distribution* of the hydrogen does not effect the bulk modulus either. We see once again that the mean coordination is much more important than the detailed geometry in determining the mechanical/elastic properties of the system. For hydrogenated samples near the rigidity threshold, which are required to explain the EXAFS results, the elastic constants should be an order of magnitude lower than in SiGe alloys that do not contain hydrogen. Sample annealing, allowing for the removal of cracks and hydrogen, would increase the rigidity of the lattice, and hence produce more composition dependence of the EXAFS results and larger elastic moduli.

## 5.4 Discussion

How does one account for these fundamental disagreements between theory and experiment in crystalline and amorphous alloys? It is possible that the angular forces  $\beta$  become anomalously small in the alloy: much smaller than in pure Si or Ge. This could be due to some complicated charge transfer effects of the kind that are known to occur in metals. However no such effects have been seen in any III-IV or II-VI compounds and so this possibility has to be regarded as extremely unlikely. It is possible that the presence of hydrogen might substantially weaken the angular force  $\beta$ , but no evidence of such a phenomenon has been seen in hydrogenated amorphous silicon. For example Maley and Lannin (1987) showed

with Raman scattering that the *position* of the peaks remains the same in *a*-Si with or without hydrogen.

A second possibility is that the EXAFS data has been incorrectly interpreted. While some theory is necessary to extract the number and distance associated with the various nearest neighbor pairs, the EXAFS technique has been very successful in other semiconducting alloys for nearest neighbor distances and it is difficult to see why it would fail here. However, although these results are all consistent with a flat curve, we must not forget that the error bars on the measurements are around 0.02Å. It is true that the size mismatch between Si and Ge is only 5% but this is comparable with the 8% bond length mismatch in for Ga-As and In-As bonds GaInAs for example. One should also note that all the experiments cited agree that SiGe forms a good random solid solution, as evidenced by the relative weights in the EXAFS components. It is true that if the Si and Ge were phase separated, this would account for the observed composition independence of the Ge-Ge and Si-Ge bond lengths. However this would lead to very little weight in the Si-Ge component, as these bonds would only occur along the interfaces between the two phases.

Finally we have the possibility that there is a very large, between 45% and 65% atomic fraction of hydrogen. Although this is a huge amount, we can find proportions of hydrogen in *a*-Si and *technological a*-Si that contain typically between 10 and 30 atomic %H (Pankove and Johnson, 1991). Such material would be mechanically weakened and show very soft elastic behavior. when compared with crystalline Si and Ge (see Figure 5.7). I have been unable to find any measurements of the elastic constants for hydrogenated material. Maley and Lannin (1987) also pointed to a marked sharpening of the TO peak associated with hy-

drogen and due the improvement of the local structure in  $\alpha$ -SiGe:H alloys with up to 40 atomic %H. Also the same results are obtained experimentally for both crystalline and amorphous SiGe alloys and it is even harder to envisage how so much hydrogen could be incorporated uniformly into the crystalline alloys. However, the presence of planar cracks on a very short length scale can apply to both crystalline and amorphous alloys and is compatible with the preparation method used to obtain these samples.

## 5.5 Conclusion

EXAFS is a very powerful technique that has opened up a new field of measurements i.e. the local structure of disordered systems. However, because this technique is an indirect one, one has to remain very careful in interpreting the results. The curious results for SiGe alloys open up many questions which will require more experiments to sort out. In particular, I would suggest EXAFS measurements on SiGe samples not containing hydrogen.

# Chapter 6

## Surface of semiconductors

The development of tools to observe directly the surface with an accuracy of about  $0.01 \text{ \AA}$  vertically has opened a whole new field of observation which is very important in order to sustain the rapid technological inventions in the field of semiconductors. The surface effects, for example, will become noticeable when trying to construct thinner and thinner samples. The study of surface can also provide, indirectly, some information on the nature of the bulk disorder which would complement results obtained from other experimental methods like EXAFS.

In this chapter, I propose to expand the theory used in the preceding chapters to cover the surface problem. I will study the surface relaxation of 2D triangular lattices as a test case, as well as surfaces of zincblende binary alloys. I will show that the successful theory developed previously by Thorpe, Garboczi and Cai (Thorpe and Garboczi, 1990; Cai and Thorpe, 1992a and 1992b) is portable to this problem and is very helpful in putting together a clear image of the results. This theory predicted correctly distortions of the lattice for the ternary semiconductors although there are still conflicts between it and experimental results regarding the binary semiconductor SiGe. I am, however, confident that the

theory will prove to be accurate also in the latter case. In section 6.1, I present the theory adapted to the surface problem and in section 6.2, I discuss different methods to obtain the topological rigidity parameters in lattices. I then present, in section 6.3, the triangular lattice results and in section 6.4, the diamond lattice, SiGe crystalline alloy with (100) and (111) surfaces.

## 6.1 Theory

The formalism developed and presented in chapter 2 was applied to crystalline and amorphous bulk alloys. However, this formalism can be extended to solve the problem of surface relaxation in semiconductor alloys. I will repeat a few steps from chapter 2 in order to show that the existence of a surface does not preclude the application of this theory and that the formalism is general enough to include the loss of symmetry due to the surface.

I can start directly from the demand that fully relaxed structure must have no net force,

$$\sum_i K_{ij}(L_{ij} - L_{ij}^0)\mathbf{R}_{ij} = 0. \quad (6.1)$$

Therefore, if one draws a plane across layers  $l$ , along any direction, the total force must also vanish:

$$(1-x)^2 K_{AA}(\langle L_{AA} \rangle_l - L_{AA}^0) + 2x(1-x)K_{AB}(\langle L_{AB} \rangle_l - L_{AB}^0) \quad (6.2)$$

$$+ x^2 K_{BB}(\langle L_{BB} \rangle_l - L_{BB}^0) = 0. \quad (6.3)$$

If the elastic constant  $K_{AA} = K_{AB} = K_{BB} = K$  then, using the general definition

$$\langle L \rangle_l = (1-x)^2 \langle L_{AA} \rangle_l + 2x(1-x) \langle L_{AB} \rangle_l + x^2 \langle L_{BB} \rangle_l, \quad (6.4)$$

with  $l$  being a layer index, one obtains

$$\langle L \rangle_l = (1-x)^2 L_{AA}^0 + 2x(1-x)L_{AB}^0 + x^2 L_{BB}^0. \quad (6.5)$$

On any layer, as well as between them, Végard's law is therefore obeyed. I can now address the question of partial length average. Assuming small displacements in the solid, one gets, as in chapter 2,

$$\begin{aligned} \mathbf{L}_{ij} &= \mathbf{R}_i - \mathbf{R}_j \\ &= \mathbf{L}_l + [(\mathbf{u}_i - \mathbf{u}_j) \cdot \mathbf{R}_{ij}^0] \mathbf{R}_{ij}^0 \end{aligned} \quad (6.6)$$

where  $\mathbf{L}_l = \langle L \rangle_l \mathbf{R}_{ij}^0$  and  $\mathbf{R}_{ij}^0$  is the unit vector of a perfect lattice and  $\mathbf{u}_i$  is the displacements from this lattice. Using the previous equation in the force equation

$$0 = \sum_i \mathbf{L}_l + [(\mathbf{u}_i - \mathbf{u}_j) \cdot \mathbf{R}_{ij}^0 - L_{ij}^0] \mathbf{R}_{ij}^0 \quad (6.7)$$

one can write

$$\mathbf{D}\mathbf{u} = \mathbf{v}, \quad (6.8)$$

where  $\mathbf{D}$  is the dynamical matrix of the system or the inverse Green function

$$\mathbf{u} = -\mathbf{G}\mathbf{v} \quad (6.9)$$

and

$$\mathbf{v} = \sum_i (\mathbf{L}_l - L_{ij}^0 \mathbf{R}_{ij}^0), \quad (6.10)$$

so that

$$\mathbf{L}_{ij} = \langle L \rangle_l + K \sum_{lm} \mathbf{R}_{ij}^0 \cdot (\mathbf{G}_{im} - \mathbf{G}_{jm}) \cdot \mathbf{R}_{lm}^0 (L_{lm}^0 - \langle L \rangle_l). \quad (6.11)$$

This equation is exactly the same as the one presented in chapter 2 except that the value of  $\langle L \rangle_l$  can vary from layer to layer. In a homogeneous solid, we can

drop the layer index. In the case of a bulk solution, one can easily obtain  $G_{im}$  and from there solve exactly for the partial lengths. By the surface, however, each layer will present a different average and the case is not so simple. For example, close to the surface, the relation

$$\sum_i \mathbf{R}_{ij} = 0 \quad (6.12)$$

no longer holds and  $i$  and  $j$  indices are not symmetric anymore.

### 6.1.1 Bond mismatch

The previous arguments are identical for both bond and site mismatch; only during the averaging does the nature of the disorder, and hence, the correlations, appear. And one would not expect, a priori, to obtain the same form at the surface as in the bulk. Nevertheless, by doing the complete algebra one finds that the bond mismatch problem leads to the same solution as previously found regarding the average lengths

$$\begin{aligned} \langle L_A \rangle_l &= \langle L \rangle_l - x a_l^* (L_B^0 - L_A^0) \\ \langle L_B \rangle_l &= \langle L \rangle_l + (1 - x) a_l^* (L_B^0 - L_A^0) \end{aligned} \quad (6.13)$$

where the topological rigidity parameter  $a_l^*$  now varies through the layers

$$a_l^* = \frac{K}{N} \sum_{ij} \mathbf{R}_{ij}^0 \cdot (G_{ii} - 2G_{ij} + G_{jj}) \cdot \mathbf{R}_{ij}^0. \quad (6.14)$$

In this equation, the summation over  $i$  and  $j$  is restricted over their respective layers defined by  $l$ . With the loss of symmetry across the surface, the Green's function cannot be obtained through the reciprocal space. In the real space, the equations are non-linear and direct calculation can become very cumbersome. I use  $a^*$  from the definition of Equation (6.14).

### 6.1.2 Site mismatch

For the site-mismatch problem, the situation is similar to the bond problem. After averaging over the different partial lengths, one obtains

$$\langle L_{AA} \rangle_l = \langle L \rangle_l + x a_l^{**} (L_{AA}^0 - L_{BB}^0) \quad (6.15)$$

and

$$\langle L_{BB} \rangle_l = \langle L \rangle_l - (1 - x) a_l^{**} (L_{AA}^0 - L_{BB}^0) \quad (6.16)$$

where

$$a_l^{**} = \frac{K}{2N} \sum_{ijklm} \mathbf{R}_{ij} \cdot (\mathbf{G}_{im} - \mathbf{G}_{jm}) \cdot \mathbf{R}_{km} (\delta_{ik} + \delta_{im} + \delta_{jk} + \delta_{jm}). \quad (6.17)$$

In the bulk, the symmetries are recovered and the equation becomes identical to the one described in chapter 2.

In site-mismatch alloys, another quantity becomes interesting at the surface: the average displacement  $u_i$  from a reference position. In the bulk, for symmetry reasons, this quantity vanishes everywhere. At the surface, however, the symmetry is broken along  $z$  and should reflect in this quantity. Averaging  $u_i$  over the sites  $A$  of a particular layer, from Equation (6.9),

$$u_i^\alpha = -K \sum_{jk\beta} G_{ij}^{\alpha\beta} R_{jk}^\beta (L_{jk}^0 - \langle L \rangle_l) \quad (6.18)$$

we obtain

$$\langle u_A^z \rangle_l = \frac{Kx}{2N} (L_{BB}^0 - L_{AA}^0) \sum_{ij} (G_{ii}^{zz} - G_{ij}^{zz}) R_{ij}^z, \quad (6.19)$$

and

$$\langle u_B^z \rangle_l = \frac{K(1-x)}{2N} (L_{BB}^0 - L_{AA}^0) \sum_{ij} (G_{ii}^{zz} - G_{ij}^{zz}) R_{ij}^z. \quad (6.20)$$

Because of symmetry,

$$\langle u_A^x \rangle_l = \langle u_A^y \rangle_l = \langle u_B^x \rangle_l = \langle u_B^y \rangle_l = 0. \quad (6.21)$$

However, the interesting quantity is the difference between the two displacements

$$\langle u_B^z \rangle_l - \langle u_A^z \rangle_l = \frac{K}{2N} (L_{BB}^0 - L_{AA}^0) \sum_{ij} (G_{ii}^{zz} - G_{ij}^{zz}) R_{ij}^z, \quad (6.22)$$

i.e., it is independent of the concentration and varies only with the layer and the size mismatch. If one also adds the difference in radius, defining the maximum height at the surface, the total distance between the two peaks in an alloy is

$$\Delta u_S^z = \left[ 1 + \frac{K}{N} \sum_{ij} (G_{ii}^{zz} - G_{ij}^{zz}) R_{ij}^z \right] \frac{(L_{BB}^0 - L_{AA}^0)}{2}. \quad (6.23)$$

One can easily verify that the average over all the species indeed vanishes. Moreover, in the bulk, the partial average displacements  $\langle u_A \rangle_l$  and  $\langle u_B \rangle_l$  vanish due to the symmetries of the Green's function and the lattice.

## 6.2 Topological rigidity parameters

There are many methods to obtain the topological rigidity parameters of a system. One would be to solve directly Equations (6.14) and (6.17), using the Green's functions of the system. For a bulk crystal, this method can be useful, providing for exact analytical result; however, for non-symmetric systems, like surfaces, clusters or glasses, obtaining the Green's functions can require huge efforts.

Another method is to use Equations (6.14) or (6.16). If one replaces a bond of length  $L_e$  by one of length  $L'_e$  in a perfect crystal, the energy changes by

$$\Delta E = K(L - L'_e)^2 - K(L - L_e)^2. \quad (6.24)$$

The force of the bond on the lattice is

$$F = \frac{d(\Delta E)}{dL} = K(L'_e - L_e). \quad (6.25)$$

But the force can also be expressed by

$$F = \frac{K}{a^*}(L - L'_e) \quad (6.26)$$

and so

$$\Delta L = L - L'_e = a^*(L'_e - L_e) \quad (6.27)$$

which is simply Equation (6.14). It is therefore possible to obtain the topological rigidity parameters by applying forces on atoms of a pure system or by alloying a lattice and relaxing the whole network. In most cases, the latter method is used because it allows a better comparison with experiment. However, for the local calculation of the topological rigidity constants (i.e., for a kink, an edge or a cluster), it is often simpler to use forces. For  $a^*$ , a force must be applied at both ends of a bond while it must be applied on all neighbors of a particular atom, radially, to obtain  $a^{**}$  for each bond around the central atom.

I have verified numerically the equivalence between using alloying or local forces to obtain the topological rigidity. In two dimensions, the local force method is unstable under relaxation close to the surface. As discussed in the next section, there is nothing surprising about this since there are problems with fluctuations in two dimensions. I have also verified this equivalence for  $a^*$  and  $a^{**}$  on a diamond structure and it works perfectly within the numerical error. It is therefore possible to extend the concepts and formalism developed in the previous section to almost any configuration.

Although the application of the force is direct for a bond case, it becomes trickier when trying to obtain  $a^{**}$  at the surface. In the bulk, one can pull on all bonds symmetrically thus involving only the pair term. At the surface, the symmetry is broken and if one pulls only on the neighbors, a net force would result, moving the system as a whole. A solution can be to add a counter force on

the central atom to compensate and keep the total force zero. Since full symmetry is lost, there could also be a contribution of the three-body term to the energy. Happily, this term vanishes to first order with a Kirkwood potential and the relation between the force and alloying described here is recovered.

### 6.3 Triangular lattice

The first system looked at is the triangular lattice. Although it does not exist in nature, it provides a useful test for the theory both because of its simplicity and of its two dimensionality which allows a simple graphical representation. For this lattice, I have used the harmonic potential described in chapter 2.

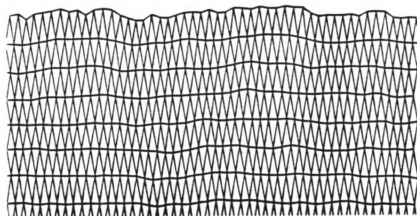
I have done the simulation using slabs with periodic boundary conditions along  $x$  and surfaces perpendicular to  $y$ . The relaxation was performed using a conjugate-gradient method presented in Numerical Recipes (see Appendix I). In the triangular network, there are two important directions, (10) and (01). Figure 6.1 (a) and (b) shows these two surfaces in a disordered state. The (10) surface has a low coordination number, three nearest-neighbors, while the sub-layer has five. This very low coordination leads to an unstable surface. On the other hand, the (11) surface, which is closer the (111) surface of semiconductors and of most interest, is more stable due to its higher coordination: the (11) surface has a fourfold coordination and all the sub-layers are perfectly coordinated.

In this chapter, I have used the experimental definition of the topological rigidity

$$a_i^* = \frac{\langle L_A \rangle_l - \langle L_B \rangle_l}{L_A^0 - L_B^0}. \quad (6.28)$$

This definition has the merit of being simple to implement and remains valid

(11)



(10)

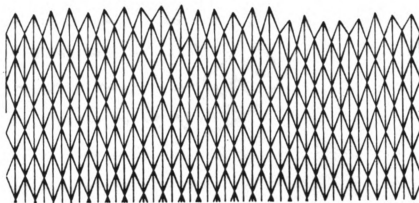


Figure 6.1: Triangular network cut along (a) (10) and (b) (11) direction. Mismatched bonds have been distributed at random with a 50-50 % probability.

in almost any geometry. Figure 6.2 shows the value of  $a_l^*$  as a function of the layer index  $l$  in a  $100 \times 100$  slab, averaged over 100 configurations. As expected, the surface presents a much floppier relaxation than the bulk; from  $a^* = 2/3$ , in the bulk, it reaches 0.82 for the first interlayer and 0.80 for the top intralayer along the (11) surface. So, we obtain an enhancement of the topological rigidity of about 25%. The difference in topological rigidity between the first inter and intralayer can be understood in the following manner. Inside the top layer, bonds are confined along  $x$  because of the periodic boundary conditions. Note that the problem would be the same for an infinite slab. However, interlayer bonds have an important component along  $y$ , which is almost free of topological constraint close to the surface. It is therefore easier for a bond in the first interlayer to keep its natural length than for an intralayer bond.

Besides the topological constant, it is important to look at the fluctuations in height at the surface. Since we are interested in probing the surface itself, such a quantity should provide us with useful information. However, the position fluctuations diverge in two dimension as was first demonstrated by Landau (1937) and Peierls (1934) in the 1930s. We can see the effect of fluctuations in the large averaging needed to obtain an accurate value for the topological rigidity. This peculiarity brings many new questions to the surface of a 2D configuration. I will not elaborate more on this problem in this chapter, delaying the discussion until the next chapter which is strictly concerned with 2D phenomena.

## 6.4 Silicon-Germanium alloy

I have also studied the surface relaxation for SiGe alloys using the Kirkwood potential described in chapter 2. As shown previously, the use of different elastic

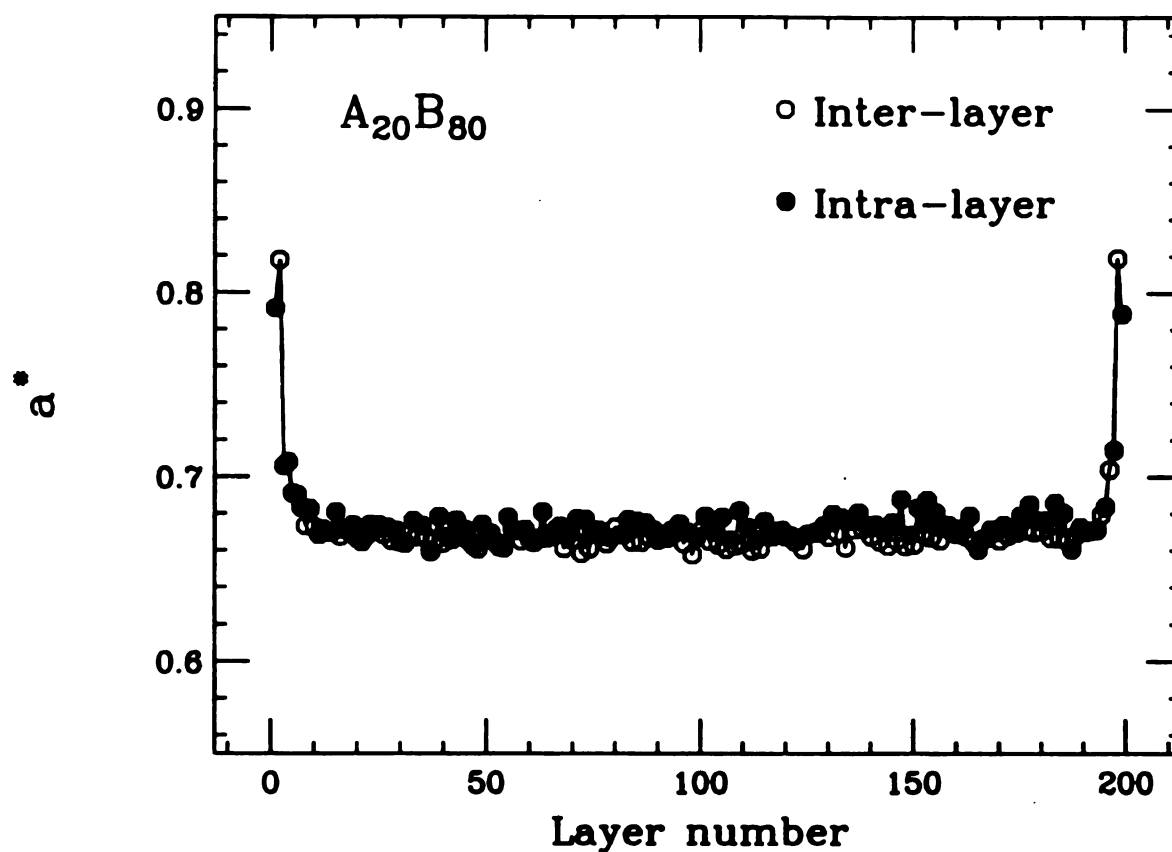


Figure 6.2: Variation of the topological rigidity parameter  $a^*$  as a function of depth in a triangular slab cut along (11) direction. The results are an average over 100 configurations of a  $200 \times 200$  sites cell with a 2% mismatch.

constants for the three different interactions (Si-Si, Ge-Ge and Si-Ge) leads to almost identical results since they differ by only 20%. To remain closer to the analytical calculations, the same elastic constants are used for all interactions.

I used periodic boundary conditions along  $x$  and  $y$ , leaving the two surfaces perpendicular to  $z$ . The two simplest directions are the (100) and (111) surfaces. As for (10) in the triangular network, the atoms at the surface (100) have few neighbors (only two), they are relatively unstable and hence, reconstruct easily. One method to inhibit surface reconstruction is to satisfy the surface dangling bonds with hydrogen. With only two bonds attached to the bulk, the surface Si atoms are etched away during this process. The atoms at the surface (111), on the other hand, have three neighbors and form a relatively stable structure (Schulze, 1983; Ancilotto, 1992; Itaya, 1992; and Steinmetz, 1990). The hydrogenation process leaves a perfect surface with no reconstruction and should allow measurement that can compare with the theory and simulations presented here. All the results can be understood in terms of the formalism developed in section 6.1

The relaxation process is much faster in 3D than in 2D. Without averaging over many configurations, the  $a^{**}$  value of the bulk shows only very small oscillations. Because of that, the averaging has been made over 20 configurations and the cell contained 31,250 atoms ( $25 \times 25 \times 25$  unit cells). The relaxation has been done using a conjugate-gradient method.

As predicted by the theory, the average bond length on each layer  $\langle L \rangle_l$  remains constant throughout the slab  $\langle L \rangle_l \equiv \langle L \rangle$ . Because the subsurface atom is tied to the bulk by only one bond, we expect, and indeed get,  $a^{**}$  to be very floppy at the surface and even more in the subsurface layer. Figure 6.3 shows

the variation of  $a^{**}$  as one moves closer to the surface. For the first two interlayers,  $a^{**}$  is about 17% larger than in the bulk. The surface effect decreases very fast, the third interlayer already gives a  $a^{**}$  value about 1% only larger than the bulk value; even at a few layers under the surface, it becomes difficult to distinguish the environment from that of a deep bulk. Figure 6.4 presents the topological rigidity as a function of the distance from a (100) surface. Since the coordination at the surface is lower than for (111), the variation of  $a^{**}$  is greater by about 27%. The same results are obtained for  $a^{**}$  using the local forces method instead of alloying, as discussed in section 6.2.

Table 6.1 shows the value of  $\Delta u$  along different directions and for two concentrations 15–85 and 50–50. As predicted by Equation (6.22), the partial displacement vanishes in the bulk and are non-zero only for the layers close to the surface, along the  $z$  direction. As predicted from the symmetry of the system,  $\Delta u$  vanishes along  $x$  and  $y$ . The difference between the average height of each species is independent of the concentration which is very similar to the difference  $\langle L_{BB} \rangle_l - \langle L_{AA} \rangle_l$  is also concentration independent.

The height at the surface is described by Equation (6.23) where the radius of species is also included. From Table 6.1, and considering a mismatch of  $0.09\text{\AA}$  for SiGe, the separation between the centers of height distribution at the surface should be around  $0.085\text{\AA}$ . However, it would be possible to determine locally the species only if the partial distributions were completely separated. Figure 6.5 shows the density distribution at the surface; it also presents the partial distributions. As one can see, these partial distributions are gaussian like (Figure 6.6) where the width of the distribution follows more or less  $a^{**}$ . The overlap between the peaks is too large to permit an atom by atom distinction between species at

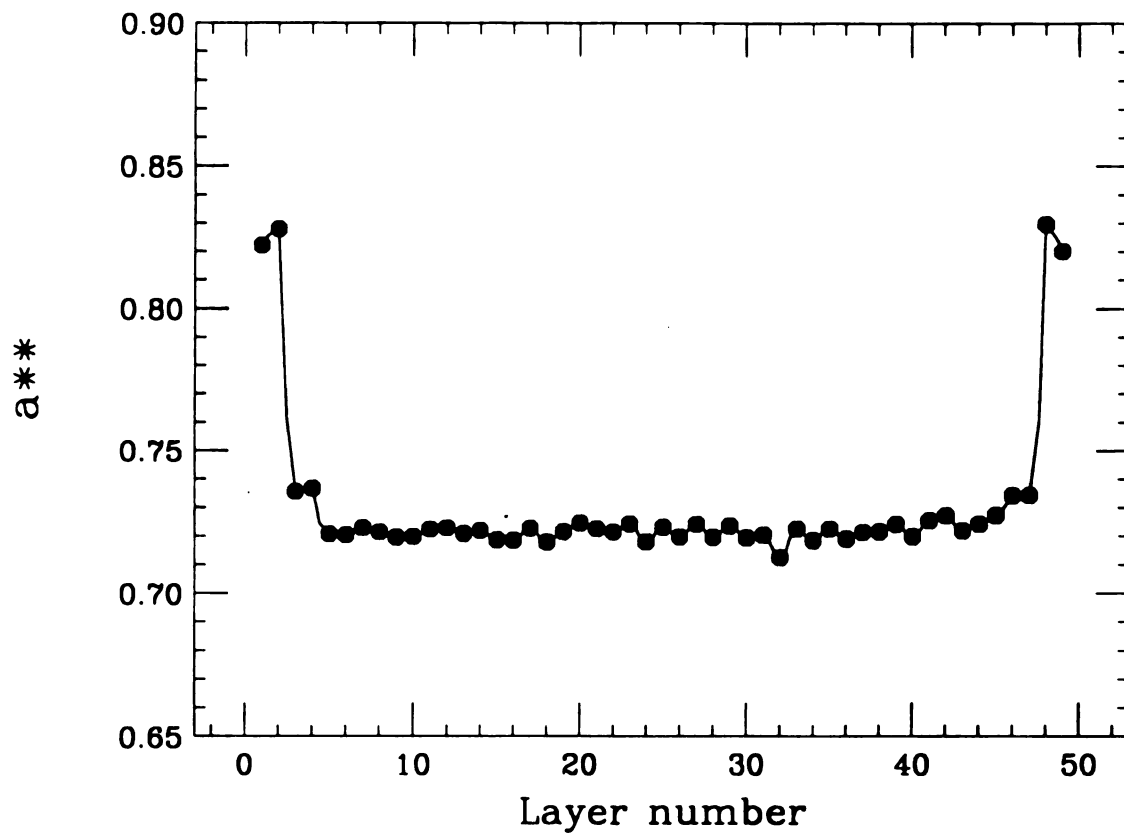


Figure 6.3: Topological rigidity parameter  $a^{**}$  as a function of the layer number from a surface (111) in SiGe alloy, averaged over 5 configurations.

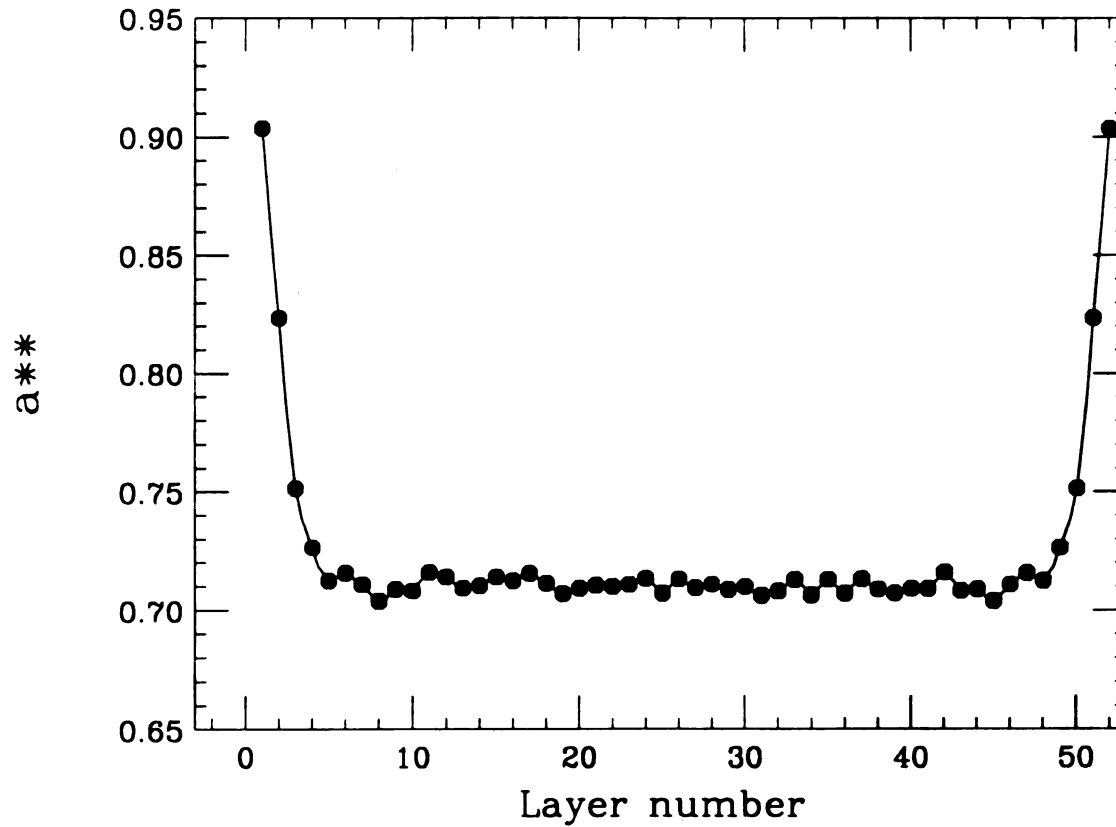


Figure 6.4: Topological rigidity parameter  $a^{**}$  as a function of the layer number from a surface (100) in SiGe alloy.

Table 6.1: Partial displacements and their difference perpendicular ( $z$ ) and parallel ( $x$  and  $y$ ) to the surface at various depths for two concentrations of SiGe alloys.

	Si <sub>50</sub> Ge <sub>50</sub>	Si <sub>15</sub> Ge <sub>85</sub>
Surface		
$\langle u_x \rangle$	-0.0010	-0.0014
$\langle u_y \rangle$	-0.0017	-0.0011
$\langle u_z \rangle$	0.0434	0.0446
Bulk		
$\langle u_z \rangle$	-0.0011	-0.0018

the surface.

Although the floppiness is isotropic in the bulk, it is not at the surface, as we could expect (Figure 6.7 and 6.8). On the top layer, the width of displacement along  $x$ ,  $y$ , and  $z$  is almost the same, with  $z$  being only slightly larger. However, on the sub-surface layer, the difference is very important. The values of the width of distribution along  $x$  and  $y$  is bulk-like while along  $z$ , it retains almost the surface value. The effect of the layer directly over it does not seem to have any noticeable effect on the  $z$  relaxation. It is easy to understand this phenomenon directly from the geometry of the layers. The bond between the second and third layers is initially only in the  $z$  direction, because there is not much push from the top layers, it relaxes almost fully by disturbing the second layer which is almost free, not the third one which has all the bulk behind it.

As seen in the theory section, all the quantities described previously are

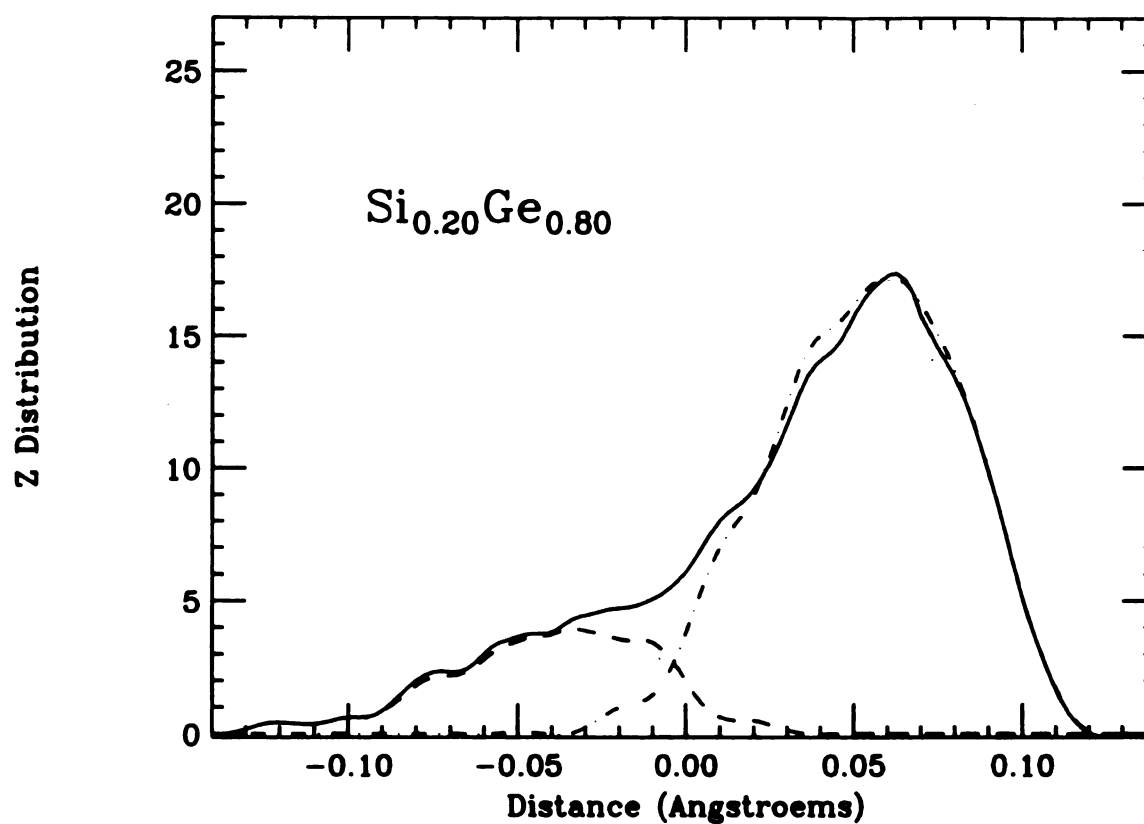


Figure 6.5: Height distribution at the surface (111) of Si<sub>20</sub>Ge<sub>80</sub> (solid line). The dashed and dot-dashed lines are the Si and Ge height distributions respectively. The curves are smoothed results from a 35,152 atom cell.

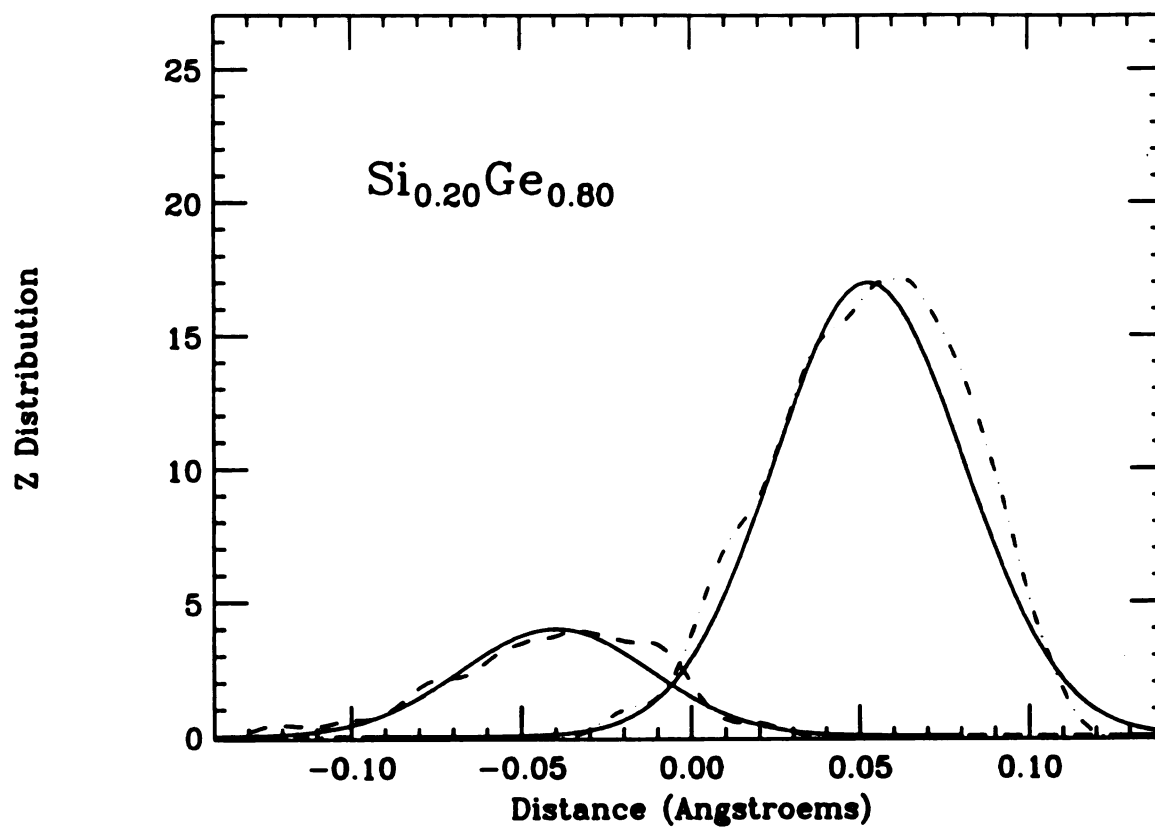


Figure 6.6: Gaussian fit (solid line) for partial  $z$  displacement distribution in  $\text{Si}_{20}\text{Ge}_{80}$  (a). The dashed and dot-dashed lines are the smoothed Si and Ge distributions respectively, the solid lines are two Gaussians with identical width.

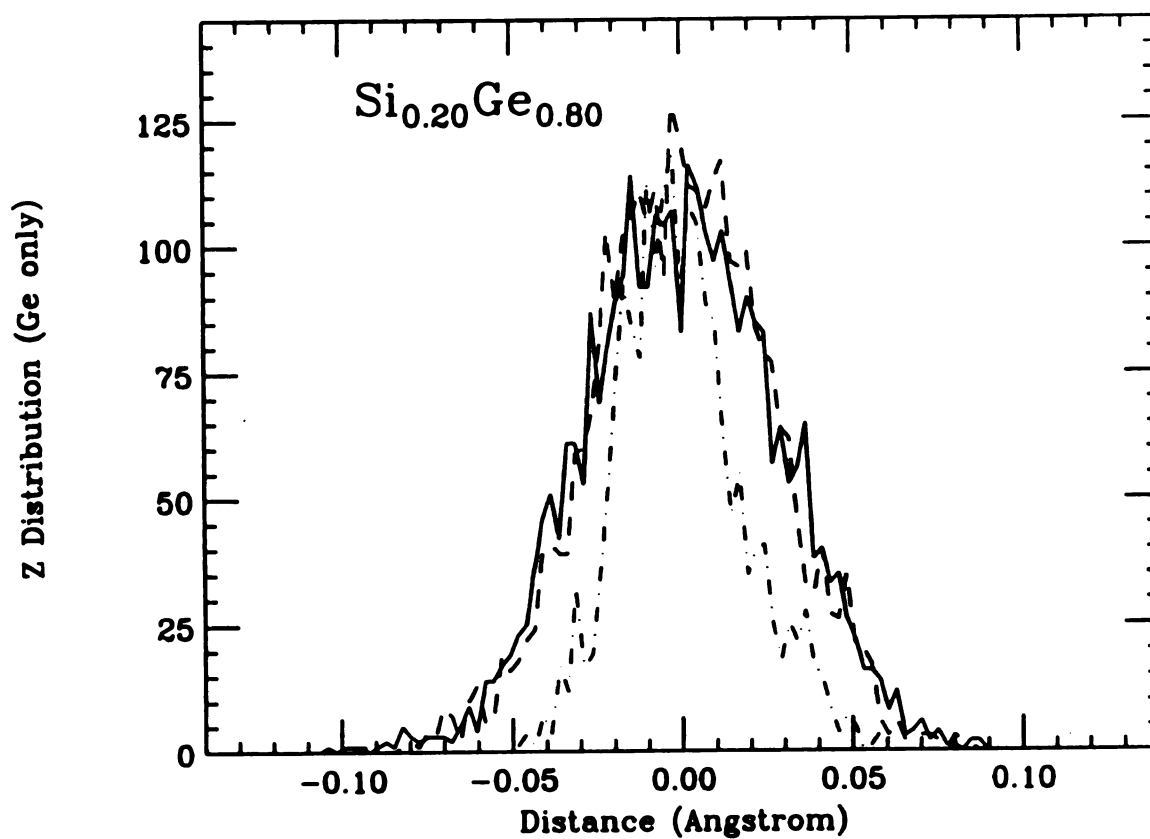


Figure 6.7: Si displacement distribution along  $z$  at the surface (111), the sub-surface and the center of a slab of  $\text{Si}_{20}\text{Ge}_{80}$  (solid, dash and dot-dash lines). The curves are averaged over 20 configurations from a 16,000 atom cell.

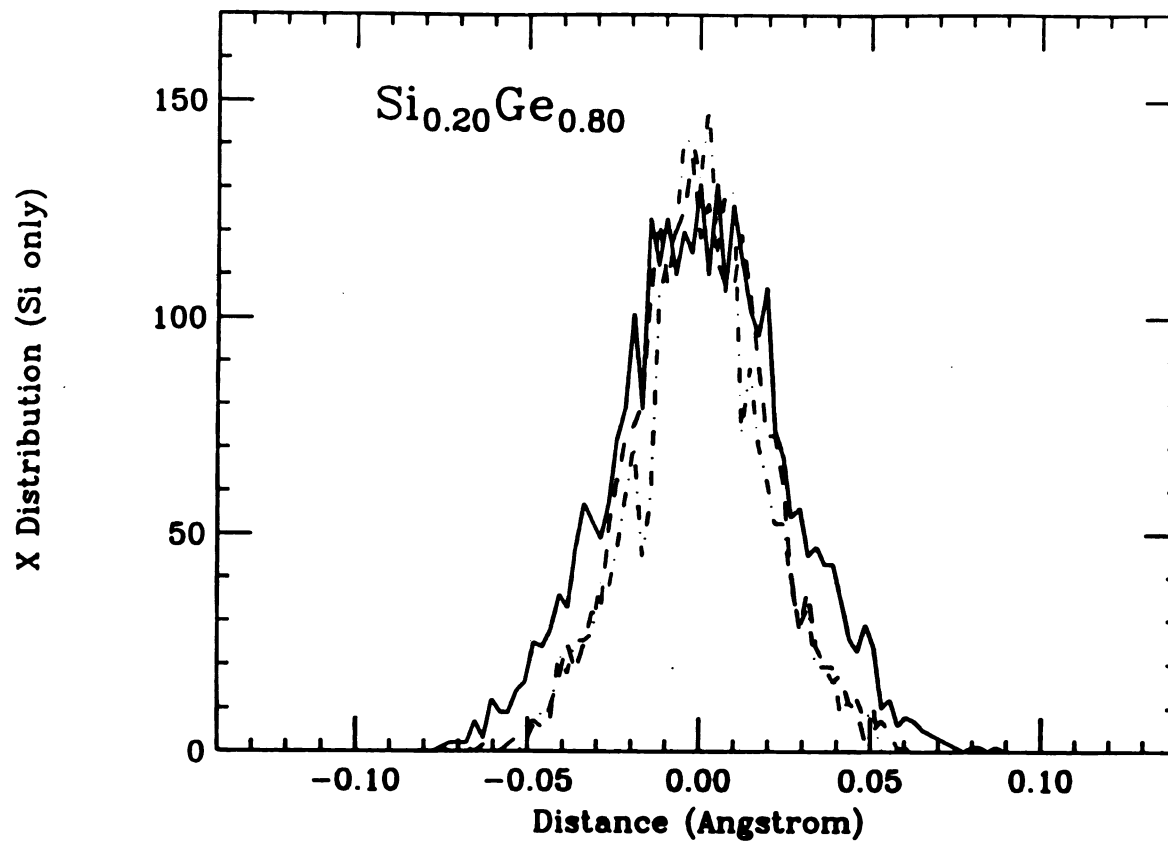


Figure 6.8: Ge displacement distribution along  $x$  at the surface (111), the sub-surface and the center of a slab of  $\text{Si}_{20}\text{Ge}_{80}$  (solid, dash and dot-dash lines). The curves are averaged over 20 configurations from a 16,000 atom cell.

function of the mismatch and the concentration of species. These relations have been spelled out in section 6.1 and provide an easy check of the simulation. I have therefore performed relaxation at two different concentrations ( $x = 0.85$  and  $0.50$  in  $\text{Si}_{1-x}\text{Ge}_x$ ) and verified that all quantities behaved as they should. From the results presented in this section, the called  $z$ -plot is indeed respected for any layer; the topological rigidity parameter  $a_l^{**}$ , although a function of layer number, remains unchanged when varying the concentration of species.

## 6.5 Conclusion

Although reconstruction is often present at the surface, it is interesting to be able to develop a phenomenological theory that would allow some understanding of the relaxation phenomenon at the surface. I have presented such a theory here and applied it to the 2D triangular lattice and the SiGe (111) and (100) surfaces. These predictions could be verified (1) by measuring the distances between the centers of atoms at the surface or (2) directly, using some kind of scanning microscope (see Figure 6.9). Recent developments in scanning force microscopy give some hope to see a precision along the vertical displacement good enough to see the distributions described here (Meyer and Heinzlmann, 1992; Meyer, 1993).

The study of surfaces is also important because it emphasizes the effects of mismatch. All the distributions are enhanced and therefore easier to see, the strain is reduced at the cost of increasing the distortions in the crystalline lattice. As we could see, the concept of topological rigidity allows us to describe quantitatively the floppiness of the network as we approach the surface. In both the 2D and 3D cases, the effects of surface on the relaxation die out very fast in the bulk, after only a couple layers. I have also shown that it is possible to calculate the

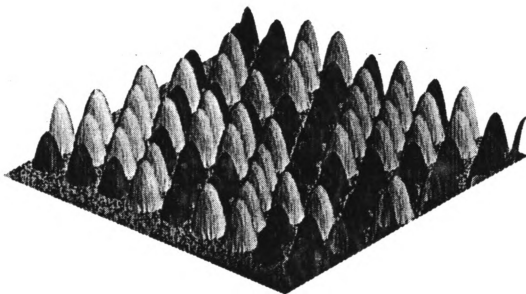


Figure 6.9: Simulated density plot of the surface (111) of  $Si_{50}Ge_{50}$  alloy. The darker peaks are Si atoms and the lighter, Ge.

topological constant locally simply by applying a force on a few atoms. This method is much simpler than trying to obtain  $a^*$  or  $a^{**}$  directly from the Green's functions, particularly in non-symmetric configurations.

Although  $a^{**}$  and the displacement distribution are not directly related, the same theory applies at the surface and in the volume. If the surface results are in agreement with the theory then one can hope that the theory is also valid in the bulk. Therefore, a measurement of the surface relaxation can give important clues about the volume strain in the limits of this theory.

## Chapter 7

# Two-dimensional melting

The concept of bond and site mismatch can also be useful in two dimensions where the stability of phases is very sensitive to disorder. Unlike surfaces, which are quasi two-dimensional systems, these systems are restricted to motion in the plane only, leading to unique behavior. This peculiar behavior of phases in two-dimensional systems has been predicted a long time ago, independently, by Peierls (1934) and Landau (1937) who showed that a long-range crystal cannot persist at any finite temperature. More recently, Mermin (1966) was able to show that only the position-position correlation would decay at any finite temperature while the angular correlation would remain long-range. A few years later, Kosterlitz and Thouless (1973) introduced a theory of melting particular to two-dimensional systems that would be driven by defects (vortices in superconductors, point defects in crystals). This theory was refined by Young (1979) and Nelson and Halperin (1978) in the case of elasticity. The KTHNY theory of two-dimensional melting predicted a third phase, included between the solid and liquid phases, that was called *hexatic*. This phase has been the subject of a large number of studies since 1979, but, to this date, it has not been found in any perfectly two-dimensional

system.

After reviewing the KTHNY theory of melting, I will present an application of the size-mismatch theory to the two-dimensional case. I will then describe the details of the simulation and present the results. Almost all the theoretical and experimental study of the two-dimensional melting has concentrated on temperature as the driving force. However, the temperature is fairly difficult to control with a great accuracy close to a phase transition. It is possible to define in size-mismatch systems, a quantity that is strictly equivalent for the description of effects of disorder, to the temperature. By using size mismatch, one can therefore drive the phase transition from a different perspective, offering complementary results to the temperature driven transition. Also, since with size mismatch a simple static relaxation is enough to reach equilibrium, it is possible to use much a larger system size which is always needed when one wants approach as close as possible a phase transition.

## 7.1 Review

The proof of the crystalline instability in two dimensions is very simple and can be obtained by various ways. I will be using here the Landau theory of phase transition and the general discussion he gives in his book on statistical physics (Landau and Lifshitz, 1980).

Defining  $\mathbf{u}(x, y)$  as the displacement from equilibrium  $\mathbf{r}(x, y)$ , the probability of any thermal fluctuation is given by

$$w \propto \exp(-\Delta F/k_B T), \quad (7.1)$$

where

$$\Delta F = \int (F - \bar{F}) dA \quad (7.2)$$

is the deviation of the total free energy from its average value and  $F$  is the free energy per unit of area. Taking the harmonic approximation for interactions in the solid, the free energy becomes

$$\Delta F = \frac{1}{2} V \sum_{ijk} u_{i\mathbf{k}} u_{j\mathbf{k}}^* \lambda_{ilmn} k_m k_n, \quad (7.3)$$

where  $\lambda$  is a real tensor, and is a function of the direction of the vector  $\mathbf{k}$  and  $u_{i\mathbf{k}}$  is the first derivative with respect to  $x_i$  of the momentum space representation of the displacement

$$\mathbf{u} = \sum_{\mathbf{k}} \mathbf{u}_{\mathbf{k}} e^{i\mathbf{k}\cdot\mathbf{r}}. \quad (7.4)$$

To obtain the mean square value of the displacement, we use the usual statistical technique

$$\langle u_{i\mathbf{k}} u_{j\mathbf{k}} \rangle = \frac{\sum_{\{\mathbf{u}(\mathbf{r})\}} u_{i\mathbf{k}} u_{j\mathbf{k}} e^{-\Delta F[\mathbf{u}]/k_B T}}{\sum_{\{\mathbf{u}(\mathbf{r})\}} e^{-\Delta F[\mathbf{u}]/k_B T}} \quad (7.5)$$

where the sum is over all possible displacement fields  $\mathbf{u}(\mathbf{r})$ . Solving for this equation, we obtain

$$\langle u_{i\mathbf{k}} u_{j\mathbf{k}} \rangle = \left( \frac{T}{A} \right) \frac{\lambda_{ilmn}^{-1}}{k_m k_n}, \quad (7.6)$$

and

$$\langle u_{i\mathbf{k}} u_{j\mathbf{k}'} \rangle = 0 \quad (7.7)$$

for  $\mathbf{k}' \neq -\mathbf{k}$ .

The mean values are found by summing over the  $k$ 's. The mean square displacement vector is therefore given by, changing the discrete sum into an integral:

$$\langle |\mathbf{u}|^2 \rangle = T \int \frac{A_{ll}(\hat{\mathbf{n}})}{k^2} \frac{d^2 k}{(2\pi)^2}, \quad (7.8)$$

$$= \frac{T}{(2\pi)^2} \int_0^{2\pi} A_{ii}(\phi) d\phi \int_0^{1/d} \frac{dk}{k}.$$

If one performs the integral over  $k$ , one finds that it diverges logarithmically as  $k \rightarrow 0$  or, in the real space, as the distance goes to infinity. The divergence of the mean square displacement implies that, on average, the atoms on a heated lattice find themselves at an infinite distance (logarithmically speaking) from the point they were at, at zero temperature. For any fluctuation greater than  $\sqrt{\langle |u|^2 \rangle} \approx a$ , the ideal lattice spacing, it becomes impossible to assign a posteriori a crystal point to an atom, and therefore the long-range periodicity is lost. Thus, in two dimensions, thermal fluctuations always destroy the long-range periodicity of a lattice, for any non-zero temperature.

The lack of long-range periodicity does not preclude all long-range order. As noted by Landau in 1937, “[i]f the body is isotropic, then  $\rho = \text{const}$ ; however, from  $\rho = \text{const}$  it does not follow that the body should necessarily be isotropic” (from Brock, 1992). For example, the angle between the local crystallographic axes and the axes of the ideal lattice (Mermin, 1968)

$$\theta(x, y) = \frac{1}{2}(\partial_x u_y - \partial_y u_x), \quad (7.9)$$

where  $\mathbf{u}(x, y)$  represents the displacement field vector introduces in its Fourier transform a factor  $k$  more than in the displacement field itself:

$$\theta(x, y) = \frac{1}{2} \sum_{\mathbf{k}} (ik_x u_{y,\mathbf{k}} - ik_y u_{x,\mathbf{k}}) e^{i\mathbf{k}\cdot\mathbf{u}}. \quad (7.10)$$

Therefore, the thermal average becomes

$$\langle \theta^2 \rangle = \frac{T}{(4\pi)^2} \int_0^{2\pi} f_i(\phi) f_j(\phi) A_{ij}(\hat{n}) d\phi \int_0^{1/d} k dk, \quad (7.11)$$

with  $f_x(\phi) = \cos(\phi)$  and  $f_y(\phi) = \sin(\phi)$ . In this thermal average of the angular fluctuations, all divergence is lost and the quantity  $\langle \theta^2 \rangle$  is well defined. Because

Table 7.1: The three phases of a two-dimensional solid as predicted by the KTHNY theory with their associated correlation and defects.

	Solid	Hexatic	Liquid
$C_G(R)$	Algebraic decay	Exponential decay	Exponential decay
$C_\theta(\infty)$	Constant	Algebraic decay	Exponential decay
Defects	Pairs of dislocations	Pairs of disclinations	Disclinations

all the fluctuations do not diverge at  $d \rightarrow 0$ , this phase is called *quasi-long-range order*.

A few years later, Kosterlitz and Thouless (1973) proposed a model for melting in two dimensions. This model was applied in multiple contexts from superconductor-normal state to solid-liquid transition. In the latter case, it predicted that the melting would be driven by the separation of dilute dislocation pairs. Later and independently, Nelson and Halperin (1979) and Young (1979) discovered that another transition could be predicted from the Kosterlitz-Thouless theory if one would let the dislocations break into pairs of disclinations. The new phase was introduced between the solid and liquid phase and was called the *hexatic* phase in reference to liquid crystals where this type of oriented phase happens frequently. Table 7.1 presents the different phases as well as the kind of defect and correlation associated with them.

In two dimensions the translational order  $C_G(R)$ , defined as

$$C_G(R) = \langle \rho_G(R) \rho_G(0) \rangle \quad (7.12)$$

with

$$\rho_G(R) = e^{i\mathbf{G}\cdot[\mathbf{R}+\mathbf{u}(\mathbf{R})]}, \quad (7.13)$$

can be rewritten as

$$C_G(R) \simeq R^{-\eta_G(T)} \quad (7.14)$$

for  $T < T_M$ , using the logarithmically divergent  $\langle u^2 \rangle$  from Equation (7.9).

And  $\eta_G(T)$  is function of the Lamé elastic constants of the solid ( $\mu$  and  $\lambda$ ):

$$\eta_G(T) = k_B T |\mathbf{G}|^2 \frac{3\mu_R + \lambda_R}{4\pi\mu_R(2\mu_R + \lambda_R)}. \quad (7.15)$$

So the translational order decays algebraically to zero at large distance in the solid phase. The only defects present are isolated pairs of dislocations with opposite Burger's vector (see Figure 7.1). These defects affect the lattice only very locally; they do not perturb the general properties of the solid and so they only renormalize the Lamé constants. The deformation due to these pairs decays as  $R^{-2}$  and they can therefore be seen as the elastic equivalent of electric dipoles.

As one raises the temperature to  $T > T_m$ , the pairs of dislocations begin to unbind, creating a new phase similar to what is found in liquid crystals. Above  $T_m$ , the finite number of free dislocation leads to an exponential decay of the translational order,

$$C_G(R) \sim \exp(-R\xi_+(T)) \quad (7.16)$$

where the correlation length  $\xi_+$  diverges as  $T$  approaches  $T_m$  from above

$$\xi_+ \sim e^{\frac{\text{const}}{(T-T_m)^\nu}} \quad (7.17)$$

with

$$\bar{\nu} = 0.36963... \quad (7.18)$$

However, if one looks at the orientational order, one finds that the correlation decays only algebraically with distance

$$\langle \psi^*(R)\psi(0) \rangle \sim R^{-6(T)} \quad (7.19)$$

where

$$\psi(R) = e^{6i\theta(R)} \quad (7.20)$$

and  $\theta$  is given by Equation (7.10). The 6 appears because of the local coordination on a triangular lattice; for a square lattice, it would be 4. Although in this phase the translational order is completely lost, there is still quasi-long range order for the orientation of the solid. Since there is still some angular correlation in this phase region, Nelson and Halperin (1979) dubbed it *hexatic*, in reference to the typical names given for phases in liquid crystals.

Until now, the disclinations, a missing or surplus row of atoms on a lattice, have not been considered since they are very unfavorable in view of their high energy cost (see Figure 7.1). As free dislocations appear on the lattice, they offer a screening for the disclinations, producing a weak logarithmic binding. Since dislocations can be seen as a bound disclination pair, it becomes possible to apply again the KT theory to study the unbinding transition of disclinations. Above the second transition temperature  $T_l$ , both the translational *and* the orientational order decay exponentially, signature of a liquid phase.

After the KTHNY theory of two-dimensional melting was proposed, a large amount of theoretical and experimental studies was performed in order to find the hexatic phase. However, the search for signatures of two different second-order phase transition has been unsuccessful until now. For a more detailed review of the work done in this field, the article by Strandburg (1988) remains appropriate since few major articles have appeared since then. On the experimental side, the

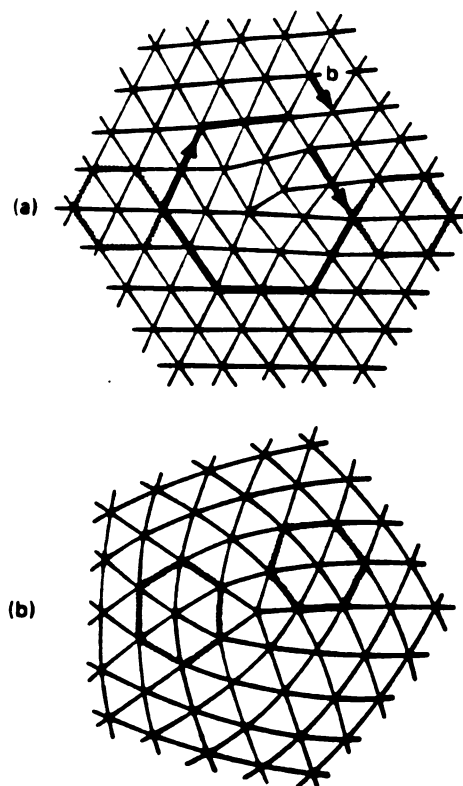


**Figure 7.1:** Different types defects on the two-dimensional triangular lattice. (a) dislocation (pair of disclinations); (b) disclinations (Brock *et al.*, 1989). The vector labeled  $b$  in (a) indicates the Burger's vector associated with the dislocation.

hexatic phase has been found only in liquid crystal where one can argue about the dimensionality of even mono-layered films; it is difficult to consider these long molecules as a perfect two-dimensional system. There are interactions along these molecules that can distribute the strain along the third dimension also. Some work has also been performed with magnetic bubbles and colloidal suspensions (see Murray, 1992, for a review of this work) but the phase transition happens at a much higher density of defects than predicted by the KTHNY theory. From the theoretical side, the efforts have gone on two fronts. The first one, analytical, was the development of first-order transition theory for the two-dimensional melting, analogous to what is found in three dimensions. One of the major problems with the KTHNY theory is that the density of defects must be low enough so that one can neglect the interactions between them. In most simulations, the number of defects present at the phase transition is large enough so that it is not clear if this approximation misses important physical interactions. Chui (1983) and Kleinert (1983) have proposed another mechanism for melting that do not support the presence of an hexatic phase. However, there are also problems with the different approximations present in the later theories. The second theoretical effort was directed to trying to simulate directly the two-dimensional melting but this project turned out to be much more difficult than predicted. Many groups have tried to obtain a phase diagram for two-dimensional melting using different configurations and potentials but nobody has yet seen the hexatic phase.

## 7.2 Theory

The problems with computer simulations are numerous: finite-size, sensitivity to boundary conditions and difficulty in handling the long-range fluctuations close

to the phase transition. One of the solutions is to use size mismatch to drive the transition. Thorpe and Cai (1991) have shown that it is possible to map the mismatch to the temperature in two-dimensional harmonic solids. The *effective* temperature was found to be, for bond mismatch,

$$k_B T_D = Kx(1-x)(L_B^0 - L_A^0)^2, \quad (7.21)$$

and

$$k_B T_D = \frac{1}{2}Kx(1-x)(L_{BB}^0 - L_{AA}^0)^2 \quad (7.22)$$

for site mismatch, when  $L_{AB}^0 = 1/2(L_{AA}^0 + L_{BB}^0)$ . In the rest of this chapter, I put  $k_B = 1$  and  $K = 1$ .

The relation 7.22 is found by comparing the equations for the correlation as a function of size mismatch with the one found in the KTHNY theory. In the case of translational order, the position-position correlation is

$$C_Q(R) = \frac{B(Q)}{R^\eta} \quad (7.23)$$

where

$$\eta = \frac{2}{3\sqrt{3}\pi}x(1-x) \left[ Q(L_{BB}^0 - L_{AA}^0) \right]^2. \quad (7.24)$$

Which is equal to Equation (7.15) for  $k_B T$  described by Equation (7.22) and the Lamé constant  $\lambda = \mu = \sqrt{3}K/4$ .

Similarly, by using similar derivations as those used in Thorpe and Cai (1989) for the bond mismatch, one finds that the angular correlation in the site mismatch case are

$$C_\theta(\infty) = e^{-W_6}, \quad (7.25)$$

where

$$W_6 = 2.466x(1-x) \left[ \frac{(L_{BB}^0 - L_{AA}^0)}{\langle L \rangle} \right]^2. \quad (7.26)$$

These results are valid only in the solid phase and are not directly extensible to predict a phase transition since the derivation assumes that the network is perfectly coordinated. The inclusion of defects would call for an effective-medium theory similar to the KTHNY derivation and therefore lead to identical results. However, there are fundamental differences between temperature and mismatch disorder in the localization of the second compared with the former. Nevertheless, following the exact results described earlier, we can propose a phase diagram in the temperature-mismatch plane (see Figure 7.2). It would be therefore possible to pass continuously from the pure mismatch disorder to the pure temperature disorder. There is of course a difference between these two disorders: the equilibrium phase. In mismatch alloys, the random configuration is never the lowest energy one. Even if the potential favors equally phase separation and ordering, the equilibrium phase would be a mixture of phase separated and ordered regions. In spite of this difference, such alloys exist in real life because the time scale for reaching the lowest state is too long, this is why the analogy proposed here can be regarded as exact.

### 7.3 Details of simulations

For simulations, it is important to have a finite-range potential, to allow for the formation of defects, i.e. variable number of neighbors, which is not included in the harmonic theory developed in the preceding section. However, I had to keep a quadratic term around the minimum of the potential so that it would be possible to compare the results in the solid phase with the analytical theory. I

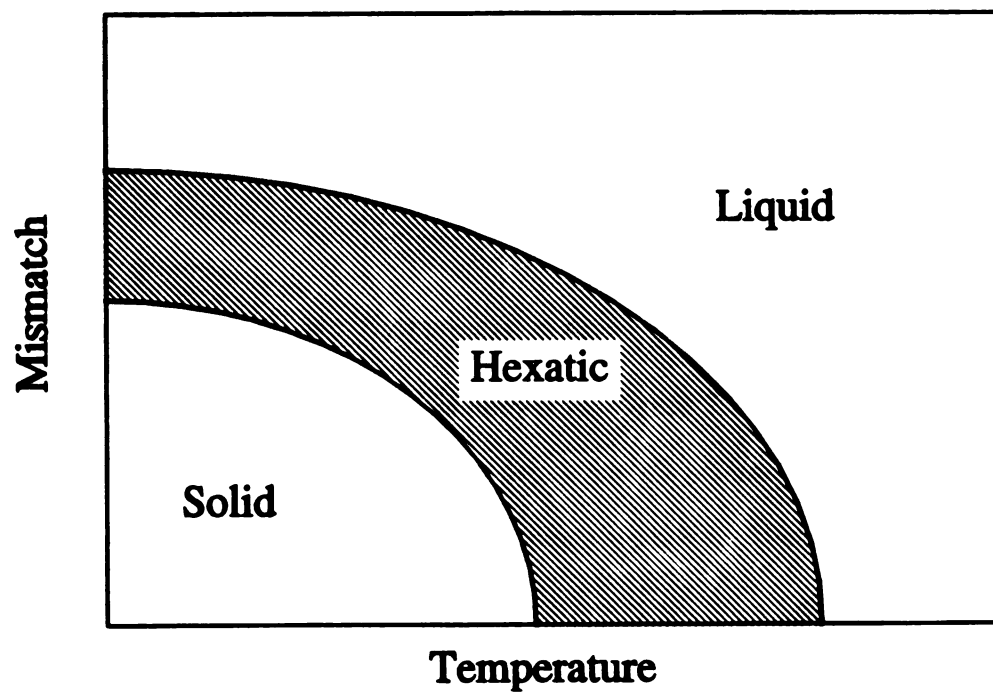


Figure 7.2: Proposed phase diagram of the two-dimensional melting in the mismatch-temperature plane.

had therefore constructed a pseudo-harmonic potential composed of four parts:

$$\left(\frac{\sigma}{r}\right)^{12} + \epsilon_1 \quad \text{for } r < r_1 \quad (7.27)$$

$$V(r) = K_2(r - r_{eq})^2 + \epsilon_2 \quad \text{for } r_1 < r < r_2$$

$$K_3(r - r_3)^2 \quad \text{for } r < r_3 \quad (7.28)$$

$$0 \quad \text{for } r > r_3,$$

where  $K_2, r_1, r_{eq}, r_2$  and  $r_3$  are variables and

$$K_3 = K_2 \frac{(r_2 - r_{eq})}{r_2 - r_3} \quad (7.29)$$

$$\epsilon_2 = K_2(r_2 - r_{eq})^2 - K_3(r_2 - r_3)^2$$

$$\sigma = \left[ \frac{K_2 r_1^{13} (r_{eq} - r_1)}{6} \right]^{1/6} \quad (7.30)$$

$$\epsilon_1 = K_2(r_1 - r_2)^2 - \epsilon_2 - \left(\frac{\sigma}{r_1}\right)^{12}$$

The shape of this potential is shown in Figure 7.3 and its derivative, in Figure 7.4. Typically, I chose the same depth for all interactions, insuring that there would be no tendencies to cluster or phase separate. Also, the  $AB$  length is always taken to be

$$L_{AB}^0 = \frac{1}{2}(L_{AA}^0 + L_{BB}^0) \quad (7.31)$$

I have also performed simulations using a truncated Lennard-Jones potential (truncated between the 3rd and 4th neighbor) in order to verify which results are general and which ones depend on the nature of the potential. The functional form of the potential is

$$V(r) = \epsilon \left[ \left(\frac{\sigma}{r}\right)^{12} \left(\frac{\sigma}{r}\right)^6 \right], \quad (7.32)$$

where I defined the  $\epsilon$  related to the partial lengths  $AA$ ,  $AB$  and  $BB$  such that the depth of the potential is constant:

$$\epsilon_{AB} = \epsilon_{AA} \frac{\sigma_{AB}^2}{\sigma_{AA}^2} \quad (7.33)$$

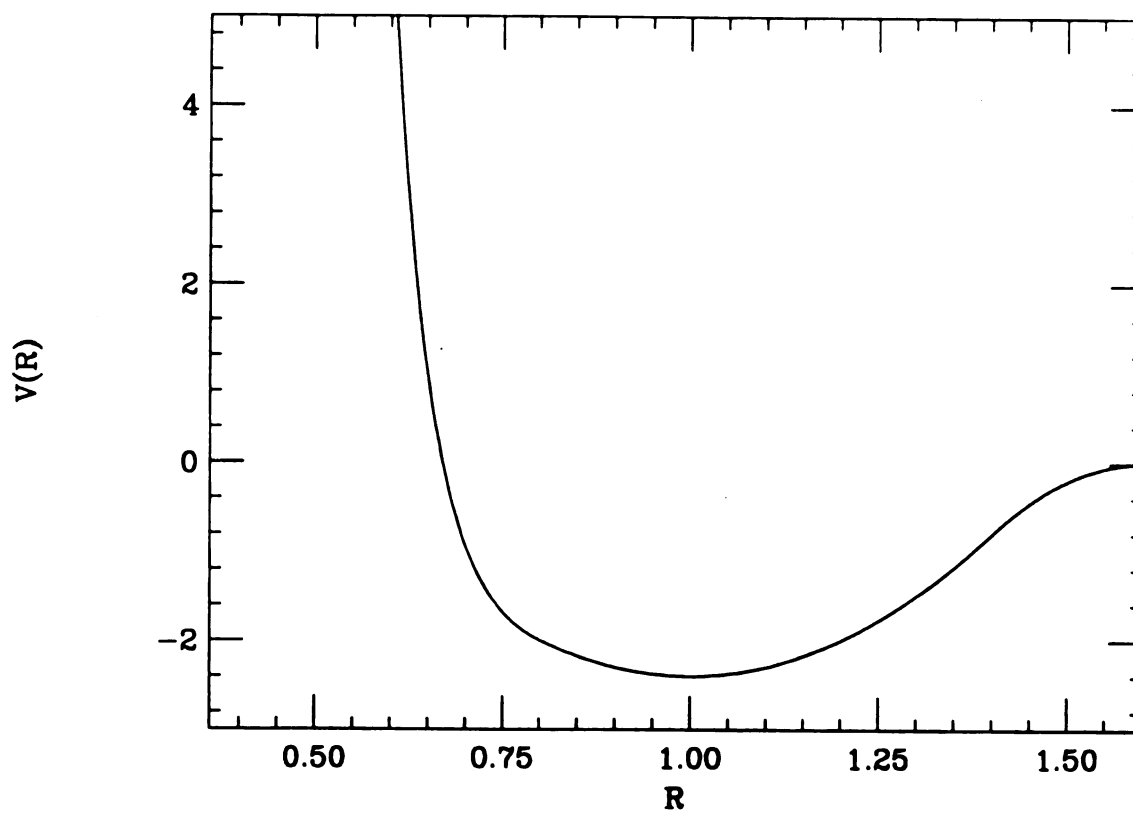


Figure 7.3: Pseudo-harmonic potential.

and

$$\epsilon_{BB} = \epsilon_{AA} \frac{\sigma_{BB}^2}{\sigma_{AA}^2}. \quad (7.34)$$

By using the geometric average for the  $AB$  ideal bond length,

$$r_{AB}^0 = \frac{1}{2}(r_{AA}^0 + r_{BB}^0) < r_{AB}^e \quad (7.35)$$

with

$$r_{AB}^e = \sqrt{2} \frac{r_{AA}^0 r_{BB}^0}{\sqrt{r_{AA}^{02} + r_{BB}^{02}}} \quad (7.36)$$

where  $r_{AB}^e$  is the mixed length needed for no favoring clustering or phase separation. In the present situation, clustering would be favored at  $T \neq 0$ .

The minimization procedure was completed using the conjugate gradient algorithm described in Appendix A. The simulation presented in this chapter were performed using large cells of 10,000 sites with randomly distributed species  $A$  and  $B$ . In most cases, the concentration was 50–50 or 25–75.

Finally, it is no longer possible to obtain the neighbor simply from a list, as was done in the previous chapters. I have used the standard Voronoi algorithm to find, uniquely, the first neighbor shell. Although not perfect for very distorted lattices, it is the most effective and stable method for defining clearly the local environment.

## 7.4 Results

The first step was to verify the application of the harmonic theory to the pseudo-harmonic potential in the solid phase region and to verify the validity of the effective temperature as the main disorder parameter. Figure 7.5 also presents results at different concentrations but with the same  $T_D$ . Figure 7.5 also shows

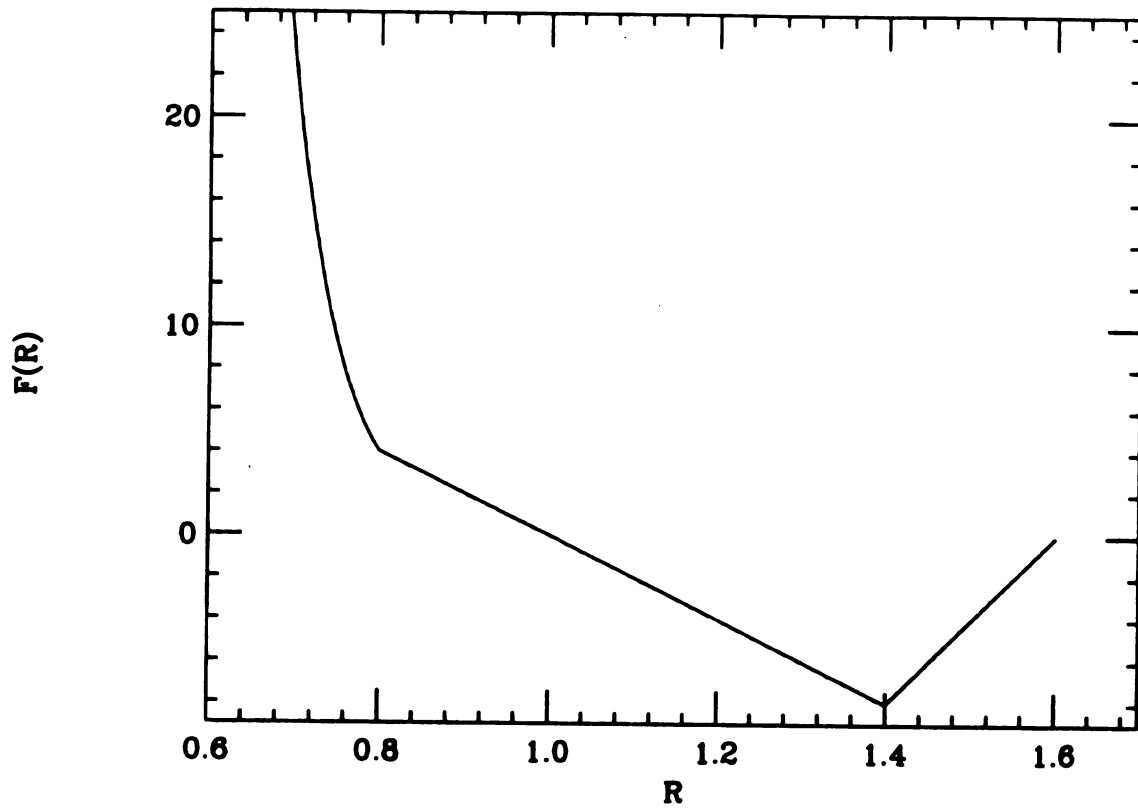


Figure 7.4: First derivative of the pseudo-harmonic potential.

that the pseudo-harmonic potential agrees well with the theory until the first defects develop. Again, the results are in excellent agreement with the theory. This is not the case with the Lennard-Jones potential which is highly anharmonic even at very low mismatch although the general behavior is consistent. As the effective temperature increases, the Lennard-Jones system departs strongly from the harmonic theory well before the first structural defect appears (see Figure 7.6). The abrupt change of slope at large  $R$  in Figures 7.5 and 7.6 is only due to the finite size of the lattice.

I have also tested the validity of the parameter  $T_D$  after the creation of defects. For a harmonic potential, this parameter is strictly valid; however, nothing guarantees that the relation holds when the first defects appear.

As the number of defects created increases, a phase transition occurs and the nature of the correlation functions changes. The translational order decays exponentially while the angular correlation decays algebraically. One can see the latter results in Figure 7.7 which shows the value of angular correlation coefficient at  $R \rightarrow \infty$  as well as the number of defects as a function of  $T_D$ . It indicates that around  $T_D = T_m = 0.005$  a transition occurs. However, this transition is not the one predicted by the KTHNY theory. For  $T_D < T_m$ , we find essentially no defects in the solid: in a  $100 \times 100$  lattice, they begin to appear only as we reach  $T_m$ . Contrary to the prediction of the KTHNY theory, there are no pairs of Burger's vectors in the lattice at low mismatch. For  $T_D > T_m$ , we assist at the creation of a large number of defects. However, almost none of them unbinds into pairs of dislocations. Only by going to very large mismatch do we begin to see the unbinding predicted by Kosterlitz and Thouless; however, the density of defects becomes large enough such that the mean-field non-interactive KTHNY

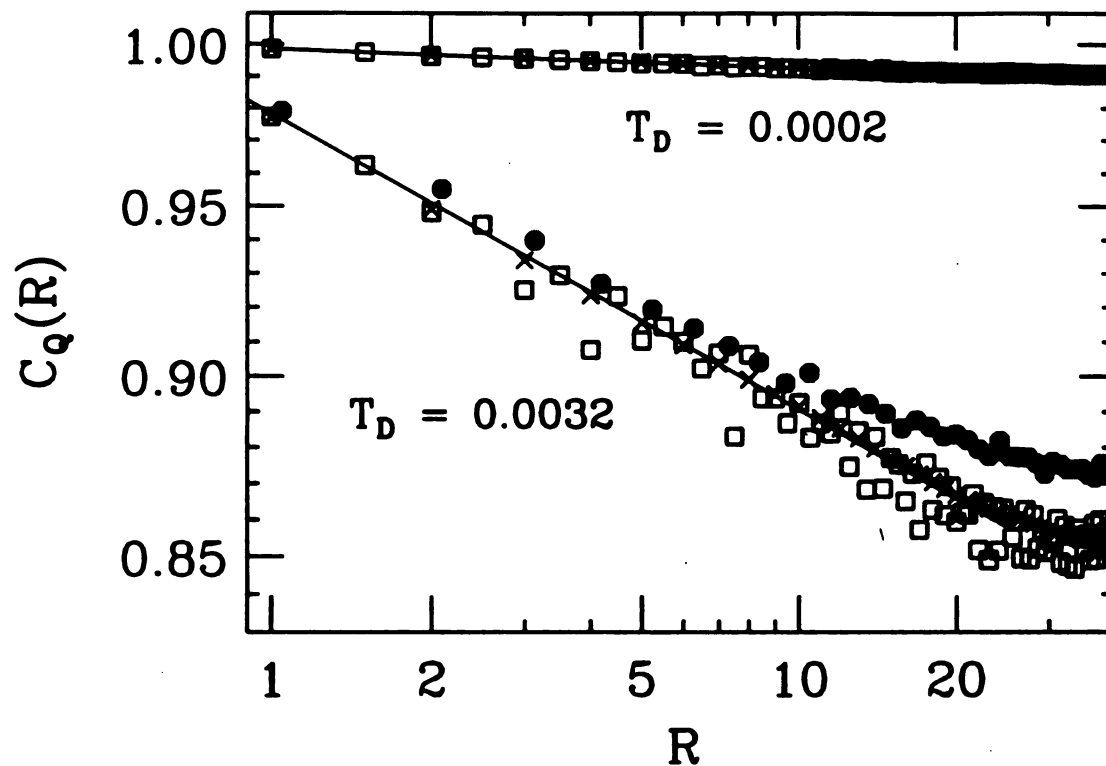
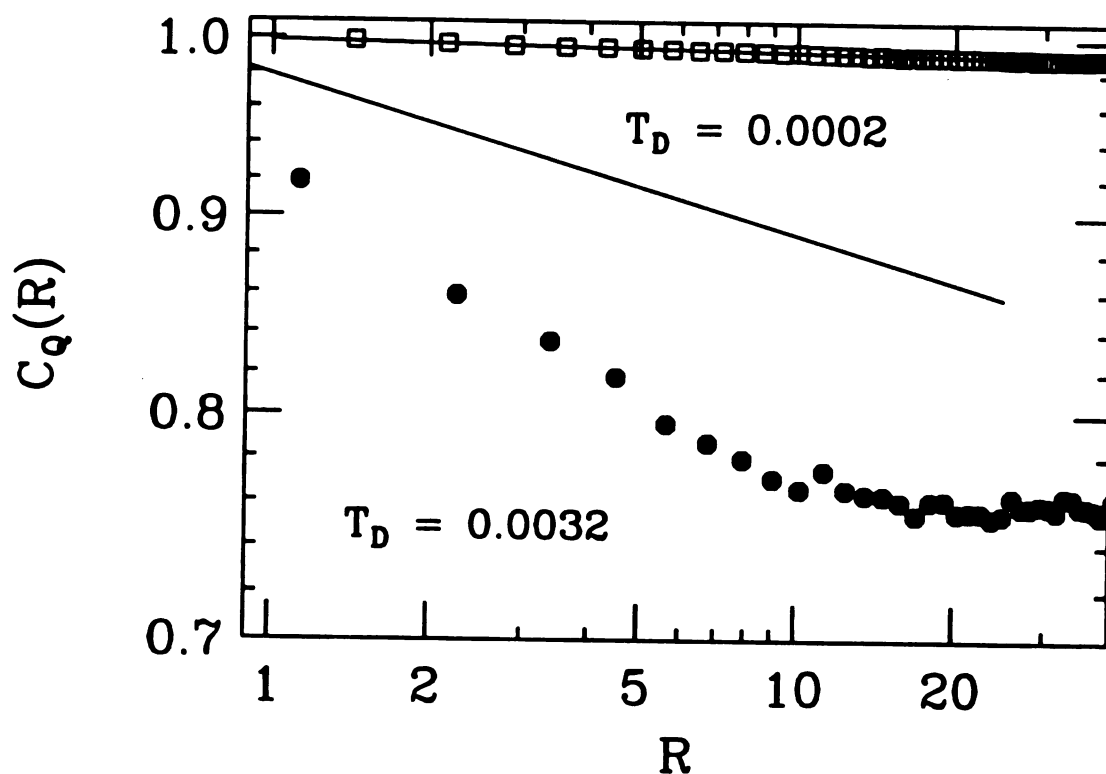


Figure 7.5: Variation of the position-position correlation as a function of distance at two effective temperatures. The solid curves are from the theory, the open squares are for a 50-50 concentration using the pseudo-harmonic potential on a  $100 \times 100$  site lattice; the crosses are for a perfectly harmonic potential on a  $200 \times 200$  site lattice; and the closed circles are for a 25-75 concentration with pseudo-harmonic potential on a  $100 \times 100$  lattice.



**Figure 7.6:** Variation of the position–position correlation as a function of distance at two effective temperatures using the truncated Lennard–Jones potential. The solid curves are from the theory and correspond to the effective temperature at which the systems were relaxed. The full symbols are for a 50–50 concentration on a  $80 \times 80$  site lattice.

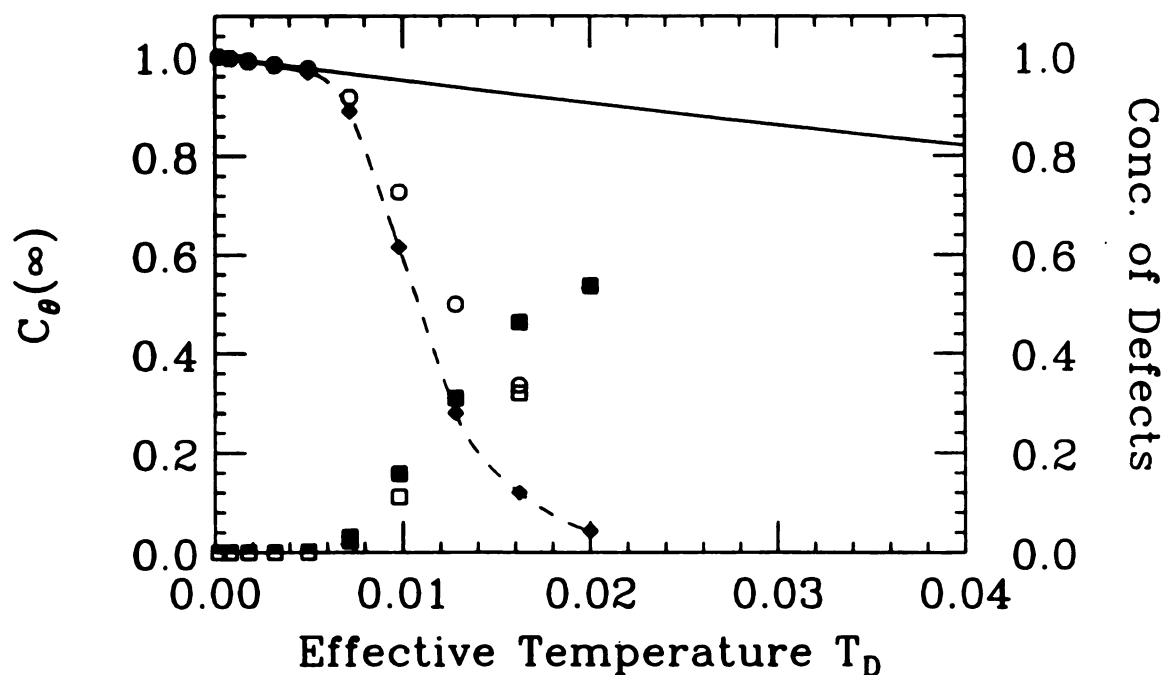


Figure 7.7: Angular correlations (circles) and number of defects (squares) as a function of  $T_D$  using the pseudo-harmonic potential. The solid line is from the theory, the dash line is a guide to the eye, the open symbols are from a 50 – 50 alloy while the closed ones are from a 25 – 75 alloy.

theory can hardly be thought to apply. Here again, the lattice relaxed using a truncated Lennard-Jones potential departs from the harmonic theory for the angular correlation at very low effective temperature and it becomes therefore difficult to point to a phase transition.

When looking at the total configurational energy for the pseudo-harmonic potential as function of temperature (Figure 7.9), we find an inflexion point at  $T_D = T_m$ , indicating a second-order phase transition at this point. Even by going to very large temperature, up to  $4T_m$ , when it is almost impossible to find

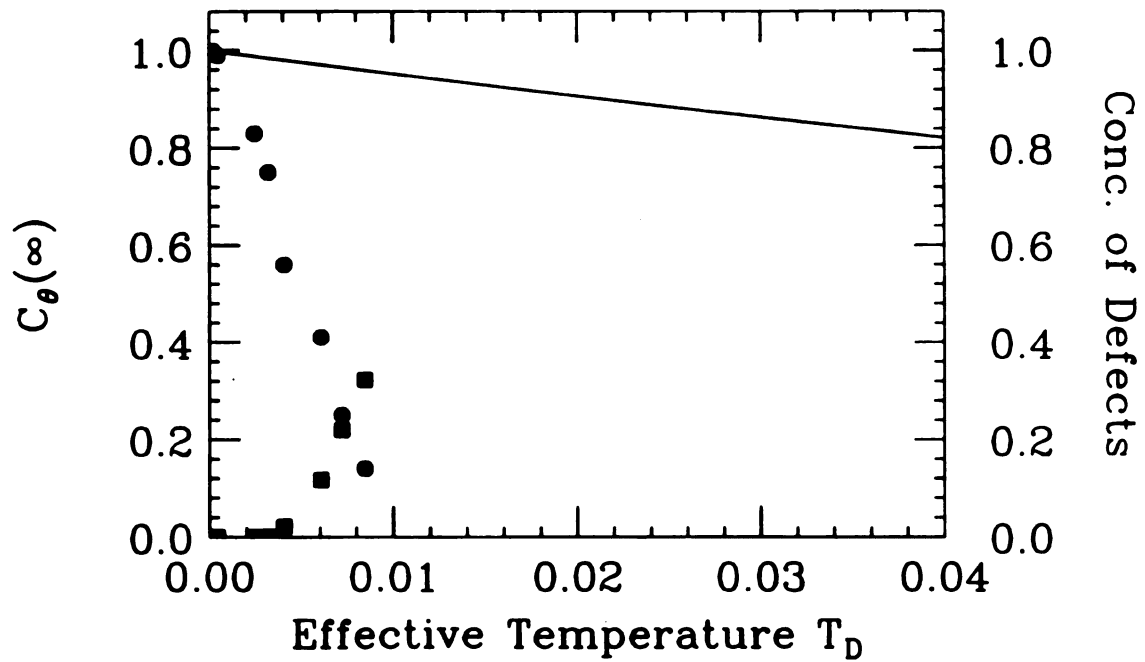


Figure 7.8: Angular correlation (circles) and number of defects (squares) as a function of  $T_D$  using the truncated Lennard-Jones potential. The solid line is from the theory and the symbols are from a 50 - 50 alloy.

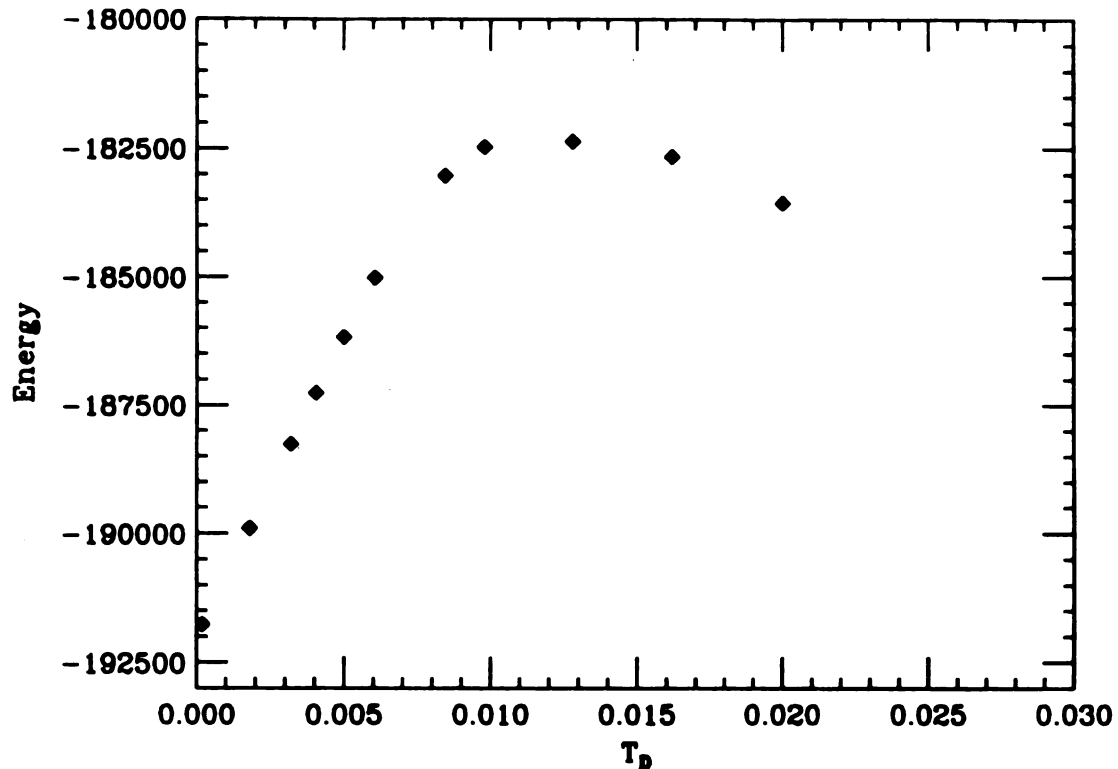


Figure 7.9: Configurational energy as a function of effective temperature  $T_D$  for a lattice relaxed using the pseudo-harmonic potential.

a relatively stable minimum, there is no sign of a second phase transition as predicted by the KTHNY theory. Since the depth is not the same for the three interactions with the truncated Lennard-Jones potential, the total configurational energy does not indicate so clearly the presence of a phase transition. These effects are convoluted with the difference in the potential depths between the species. However, it is clear, from directly looking at the cell, that there is no phase transition at a low concentration of defects corresponding to the KTHNY solid-hexatic transition.

Another characterization can be performed by measuring the elastic con-

stants of the system. For a triangular network with nearest-neighbor interactions, only one elastic constant defines the full macroscopic elasticity. However, as the number of defects increases, the lattice loses its symmetry and the need for more elastic constants appears. Since the shear modulus vanishes in the liquid phase while the bulk modulus remains finite, the choice of these two elastic constants seems a good one: monitoring the variation of the elastic constants with effective temperature should provide a reliable test of phase transition. Since the shear modulus would also vanish in the hexatic phase, another elastic constant is needed. The most obvious one is the splay rigidity (Figure 7.10) which, in the solid phase is simply

$$S = \frac{2}{9}C_{44} = \frac{2}{3}C_{11}. \quad (7.37)$$

As we go to the hexatic phase, the orientational order is still present so it costs energy to apply a splay deformation to the system. In the liquid, any deformation that preserves the volume costs no energy so the splay rigidity should vanish at the hexatic-liquid transition. As a signature of the behavior of the elastic constants for the different phase of the KTHNY theory of melting is presented in Figure 7.11. Note that the measurement of the bulk modulus does not really bring any information on the status of the system but does provide a useful scale against which to check the two other elastic constants.

It turns out that the measurement of these quantities is not as simple as it may seem. As soon as the defects appear, the lattice becomes extremely unstable against even very small deformations. Some defects appear and then disappear, creating jumps in the total energy and us preventing from obtaining a significant value for the elastic constants. Although straightforward and easy to interpret in theory, the actual computation of elastic constants turns out to be a real problem

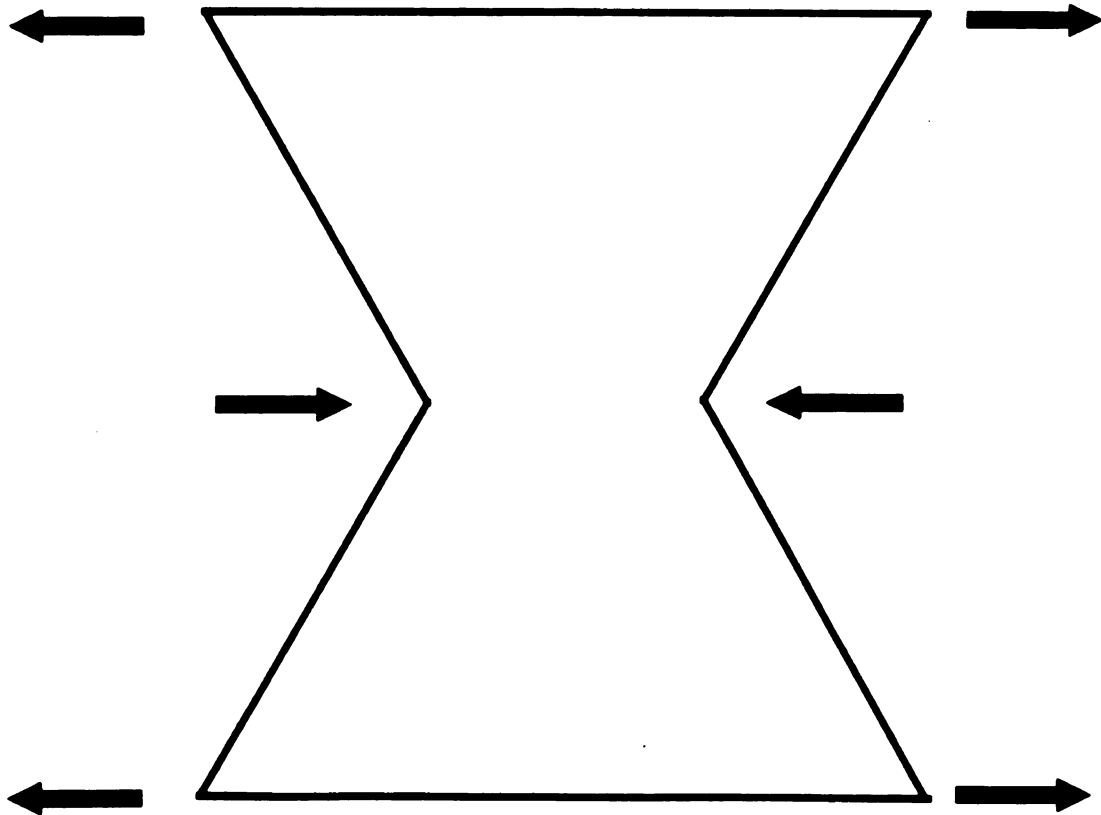


**Figure 7.10:** Splay rigidity. The arrow indicates the direction of the strain field applied to measure the splay rigidity.

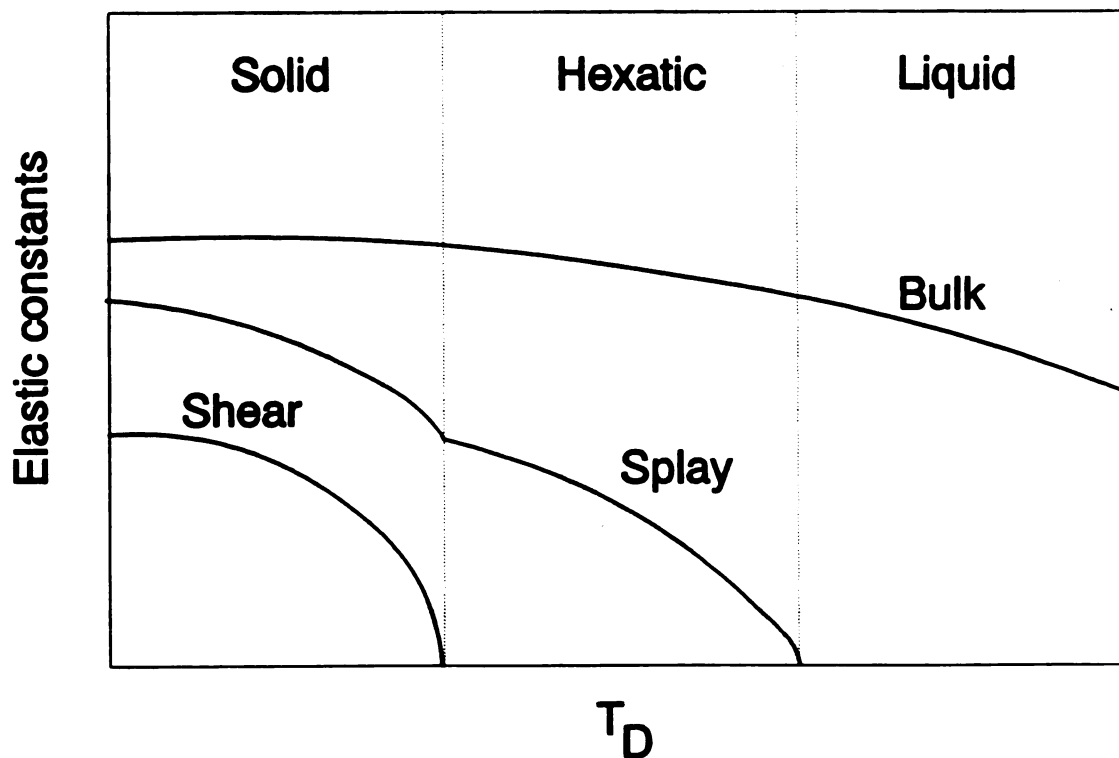


Figure 7.11: Possible phase transitions for the KTHNY theory in the elastic constants–temperature space.

and more work is needed to find ways to stabilize the system enough to be able to obtain reliable results. The problem does not seem to be the choice of potential since these difficulties are found using a Lennard–Jones potential. It comes more probably from the strain on the lattice at these high  $T_D$ .

## 7.5 Discussion

From all the different tests and simulations performed on lattices statically relaxed using a pseudo–harmonic or Lennard–Jones potential, one can draw two

conclusions: (1) The harmonic theory extends very well to the pseudo-harmonic potential for  $T < T_m$  and only at very low mismatch for the Lennard-Jones potential. (2) There is no sign of a hexatic phase or any phase transition à la Kosterlitz-Thouless. The first point emphasizes the validity of the  $T_D$  parameter to study and understand the properties of the lattice until the first defects appear. This one-to-one correspondence between size-mismatch and temperature disorder allows one to compare two very different methods of driving a phase transition. The temperature disorder creates a globally equilibrated system while the size-mismatch disorder is only locally equilibrated. Waiting long enough, at a non zero temperature, we would see the atoms segregating in ordered or phase-separated alloys. However, as with glasses, on normal time scales, the two dimensional size-mismatched alloys can be considered as equilibrated. As the mismatch increases and defects are created, the effective temperature is no longer a meaningful quantity. Once defects appear, the local stress as well as the number of contact points between the two species of the alloy will determine the overall properties. For example, by looking at Figure 7.12, which indicates the defects and the bond type on a lattice with 40 % mismatch, one sees that there is a tendency for the pairs of dislocation to form in a diamond configuration with alternate species on the corners. It is therefore natural that  $T_D$  defined previously no longer gives an accurate picture of the situation. In other terms,  $T_D$  is valid only when harmonic terms dominate. The creation of defects, being non-harmonic, opens other avenues for decreasing the stress that are not accounted for in the previous theory.

The second point is very important in the search for the elusive hexatic phase. It shows that static systems will not organize themselves in a hexatic phase. Any local strain (due to the local and frozen nature of mismatched alloys

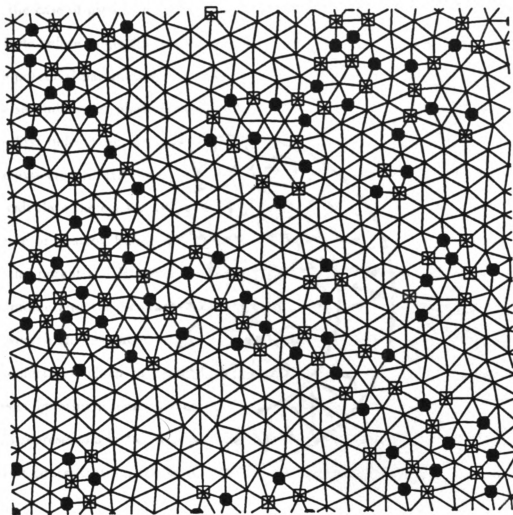


Figure 7.12: Section of a 50-50 alloy with 40 % mismatch relaxed using the pseudo-harmonic potential. The solid line represents  $A - A$  bonds, the dash one,  $A - B$  bonds, and the dotted line,  $B - B$  bonds; a open square indicates an atom its 7 first neighbors and a full circle, an atom with five-fold coordination.

by opposition with the non-local nature of temperature disordered systems) will preclude the separation of Burger's vectors. Only when a very high density of defects screens considerably the interaction do *some* dislocation pairs unbind. In the case of pseudo-harmonic potential, one can almost fill up the lattice with defects before single disclinations appear. This effect could be due to the choice of the potential parameters, too deep or too shallow. However, it would not explain the second-order phase transition indicated by the configurational energy when the first defects appear, at  $T_m = 0.0005$ . This transition is totally different from the expected KTHNY one. The new phase seems extremely unstable and efforts to calculate the elastic constants have shown that a very small perturbation can create or destroy hundred of defects. One could believe that the problem lies in the potential. However, although many results differ between the pseudo-harmonic and the Lennard-Jones potential, there are two constants: (1) Even at very high mismatch, single disclinations do not appear; and (2) the density of defects at which some unbinding happens turns out to be very high and a theory ignoring interactions between pairs of dislocations cannot be valid. Figure 7.13 represents a lattice relaxed with Lennard-Jones potential, even at very large defect concentration, one finds only very few single disclinations.

## 7.6 Conclusion

Although the search for hexatic phase comes in empty-handed once again, the study of mismatch-driven phase transitions gives us a better understanding of the limits of the harmonic approximation and of the KTHNY theory. Because static relaxation is more straightforward than Monte-Carlo or molecular dynamics, it is possible to look at much bigger samples. The correspondence between

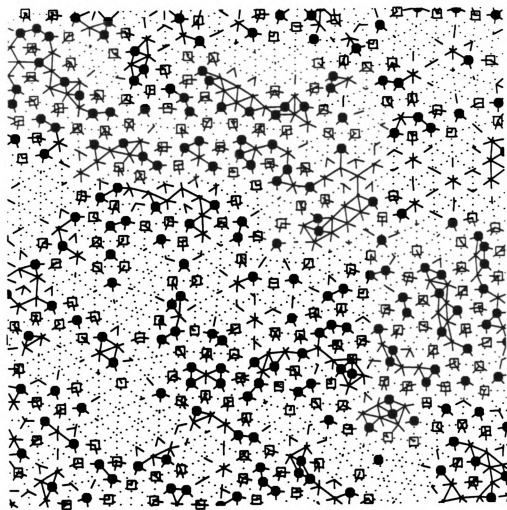


Figure 7.13: Section of a 50-50 alloy with 26 % mismatch relaxed using the Lennard-Jones potential. A open square indicates an atom with 7 first neighbors and a full circle, an atom with five-fold coordination.

temperature and mismatch is exact at low  $T_D$ , allowing a meaningful comparison between both. However, this relation breaks down somewhat when the first defects appear. Also, lattices become unstable at large mismatch and create chains of pairs of dislocations that eventually fill up almost all the lattice without evidence of a second phase transition. Since the details of the phase transition in the system presented here differ dramatically from what is predicted by the KTHNY theory, it is possible to conclude that the KTHNY transition is not always favored in 2D and, at least, does not reflect the behavior of mismatched systems.

# Chapter 8

## Conclusion

The knowledge of the structure of a solid is primordial to a satisfying understanding of its electronic properties. Too often, physicists make very accurate calculations based on a poor model. In this thesis, I have tried to improve the understanding of the structural properties of relatively weakly disordered systems: binary solid solutions. Even with this low disorder, the structure turns out to be very different from what was predicted using perturbation theory; instead of a large distribution around the linear combination of the properties of each species, we find multiple peaks centered close to the individual natural lengths.

In the case of metallic alloys, the simple Hooke's spring approach pursued here does not always give precise results; it is often necessary to account for the changes in the electronic environment that affect the quality of the chemical bonds. Nevertheless, the qualitative predictions of the harmonic theory remain valid: small rigidity parameter, three-peak distributions, etc. It is to be noted also that the more complex embedded-atom potential fails as often as the spring model to replicate the average length of the alloys.

Using the Cai and Thorpe (1992a) theory for semiconductor alloys, I

have calculated the structural properties one would expect for crystalline and amorphous SiGe solid solutions. I have shown that the effect of size mismatch on amorphous semiconductor is roughly the same as that predicted for a crystalline one. In the former case, it is possible to treat size mismatch as a perturbation compared to the large disorder introduced in the process of amorphisation. However, it turns out that the predictions for crystalline and amorphous SiGe alloys are in disagreement with recent experimental results. Because the topological rigidity parameter, which determines all the properties of the disordered network, depends only on the connectivity of the perfect lattice, it is difficult to believe that the predictions are wrong qualitatively. Some more experimental work remains to be done on this problem in order to obtain a definitive answer.

I have also extended the formalism to the surface. Although it is not possible to obtain analytically the value for  $a^{**}$ , the general ideas developed previously still hold. At the surface, the difference between the average partial lengths is larger than in the bulk, due to the lower coordination. Having predicted the height distribution as it should be seen from the surface, we can only wait to see how this prediction will compare with experiment. A consistent result at the surface would probably indicate that the bulk predictions are equally valid. It is obvious that in the treatment of the surface problem, I have not considered any reconstruction. First, due to the generality of the principle, one would expect to obtain a qualitatively similar result. Second, by covering the surface (111) with hydrogen or by heating it up to 600 C, it is possible to deconstruct completely the surface and to obtain a structure similar to what I have studied here. I have also showed the equivalence between the topological rigidity calculated globally and locally. This equivalence will be very helpful in understanding the rigidity of

non-symmetric systems.

Finally, I have attempted to look at the solid-hexatic mismatch-driven phase transition. At low mismatch, a perfect correspondence between temperature and mismatch can be found that will predict the appropriate structural correlations. However, I could not find any trace of the hexatic phase or Kosterlitz-Thouless type of phase transition. The problem of hexatic phase has been around for almost 15 years but it remains highly controversial. However, we have seen that it is not universal in the size-mismatch problem. Moreover, at low mismatch (strictly equivalent to low temperature), there is no sign of the bound dislocations predicted by the KTHNY theory, even in systems much larger than studied previously. As the first defects appear, a transition seems to occur but with the density of defects increasing very rapidly there is not even the appearance of phase transition or global unbinding of defects to be seen. With the creation of defects, the correspondence between mismatch and temperature is weakened leaving a direct extrapolation of the results between both kind of disorder somewhat less direct. It remains, nevertheless, that the results speak not for a KTHNY-type phase transition but for a more conventional one that remains to be fully characterized.

A lot of questions have been raised in this thesis. I believe that they will be answered in a near future. Many of the answers lie on the experimental side and one can only hope for the development of better analysis for EXAFS measurements. This way, it would be possible to settle the questions about the predictions for SiGe random alloys. It would also complement happily the series of numerical results obtained for the metallic alloys particularly regarding the strange behavior observed in the AuAg alloy. Some more theoretical work is still needed to understand why the EAM and CFM potentials seem to be so complementary

in their predictions. The study of surfaces is still in its infancy and so I am confident that we will soon have some experimental results to compare with the many predictions presented here. Some research would be useful to characterize quantitatively the effect of size-mismatch on reconstruction. It may be possible to prevent reconstruction by using large enough impurities at the surface. Although 2D melting has been heavily studied during the last decade, I believe we have here a solid proof that the hexatic phase is not universal. However, more work is needed in order to develop efficient tools to characterize the phase transition. The choice of elastic constants seems very appropriate but many problems remain to be solved before one can use them, in a computer simulation, as a good indicator of the structural phases. I have no doubts that many of these questions will be addressed in the next few years.

# Appendix A

## Conjugate–gradient method

The problem of finding the global minimum of a multidimensional surface is generally impossible to solve. However, there exists multiple techniques that allow one to find a *local* minimum. In the case discussed in the main text, with relatively weak disorder and fixed coordination, we can be almost certain that the minimum found by a straightforward and linear method will lead to the global minimum. In view of this insurance, the conjugate–gradient method (CGM) was used in every case. The following discussion is based on the one given in *Numerical Recipes* (Press *et al.*, 1986).

The first step in the minimization is to convert the multidimensional problem to a set of line minimizations, i.e. that we try to find a scalar  $\lambda$  that will minimize the energy  $E(\mathbf{x} + \lambda\mathbf{y})$ . The problem is now to choose appropriately the vectors  $\mathbf{x}$  and  $\mathbf{y}$ . The CGM is based on the fact that the gradient of a function minimized along a vector  $\mathbf{x}$  will be perpendicular to it at the minimum.

To see how this method works, let's start by a Taylor expansion around

some point  $\mathbf{x}_0$ :

$$E(\mathbf{x}) = E(\mathbf{x}_0) + \sum_i \frac{\delta f}{\delta x_i} |_{x_0} x_i + \frac{1}{2} \sum_{ij} \frac{\delta^2 f}{\delta x_i \delta x_j} |_{x_0} x_i x_j + \dots \quad (\text{A.1})$$

By keeping only up to the quadratic term, we get

$$E(\mathbf{x}) \simeq c + \mathbf{b} \cdot \mathbf{x} + \frac{1}{2} \mathbf{x} \cdot \mathbf{A} \cdot \mathbf{x}. \quad (\text{A.2})$$

Using this latter equation to obtain the gradient of the total energy,

$$\nabla E = \mathbf{A} \cdot \mathbf{x} + \mathbf{b}. \quad (\text{A.3})$$

By posing  $\nabla E = 0$ , one finds a set of linear equations to solve by inverting the matrix  $\mathbf{A}$ . However, this method would require the knowledge and the storage of a matrix  $N \times N$ . The CGM demands only the total energy and its gradient, an order  $N$  in information.

So, let's take two sets of vectors  $\mathbf{g}_i$  and  $\mathbf{h}_i$  with  $\mathbf{g}_0 = \mathbf{h}_0$  and a recursion defined as

$$\mathbf{g}_{i+1} = \mathbf{g}_i - \lambda_i \mathbf{A} \cdot \mathbf{h}_i \quad (\text{A.4})$$

$$\mathbf{h}_{i+1} = \mathbf{g}_{i+1} + \gamma_i \mathbf{h}_i,$$

where orthogonalisation for  $\mathbf{g}$  and conjugation for  $\mathbf{h}$  are required:

$$\mathbf{g}_{i+1} \cdot \mathbf{g}_i = \mathbf{h}_{i+1} \cdot \mathbf{A} \cdot \mathbf{h}_i = 0. \quad (\text{A.5})$$

This latter requirement defines the two scalars

$$\lambda_i = \frac{\mathbf{g}_i \cdot \mathbf{g}_i}{\mathbf{g}_i \cdot \mathbf{A} \cdot \mathbf{h}_i} \quad (\text{A.6})$$

and

$$\gamma_i = \frac{\mathbf{g}_{i+1} \cdot \mathbf{A} \cdot \mathbf{h}_i}{\mathbf{h}_i \cdot \mathbf{A} \cdot \mathbf{h}_i}. \quad (\text{A.7})$$

Moreover, these relations also imply (as can be proven by induction) that for all  $i \neq j$

$$\mathbf{g}_i \cdot \mathbf{g}_j = \mathbf{h}_i \cdot \mathbf{A} \cdot \mathbf{h}_j = 0. \quad (\text{A.8})$$

It is also possible to rewrite equations A.6 and A.7 as

$$\gamma_i = \frac{\mathbf{g}_{i+1} \cdot \mathbf{g}_{i+1}}{\mathbf{g}_i \cdot \mathbf{g}_i} = \frac{(\mathbf{g}_{i+1} - \mathbf{g}_i) \cdot \mathbf{g}_{i+1}}{\mathbf{g}_i \cdot \mathbf{g}_i}, \quad (\text{A.9})$$

and

$$\lambda_i = \frac{\mathbf{g}_i \cdot \mathbf{h}_i}{\mathbf{h}_i \cdot \mathbf{A} \cdot \mathbf{h}_i}. \quad (\text{A.10})$$

Although the last two terms in equation A.9 are equal when the function is exactly quadratic, most of the time, the total energy used is not and therefore the orthogonalisation is not perfect. The first term on the right is named after Fletcher and Reeves while the second one is called the Polak-Ribiere method. I have used the latter.

The interest of the CGM is that it does not require the knowledge of the Hessian matrix  $\mathbf{A}$ . Suppose that one has

$$\mathbf{g}_i = -\nabla E(\mathbf{x}_i) = -\mathbf{A} \cdot \mathbf{x}_i + b. \quad (\text{A.11})$$

one also sets  $\mathbf{g}_{i+1} = -\nabla E(\mathbf{x}_{i+1})$  where  $\mathbf{x}_{i+1}$  is the new minimum of the total energy obtained by minimizing the energy along a vector  $\mathbf{h}_i$ .

Since

$$\begin{aligned} \mathbf{g}_{i+1} &= \mathbf{A} \cdot (\mathbf{x}_i + \lambda \mathbf{h}_i) + b \\ &= \mathbf{g}_i - \lambda \mathbf{h}_i, \end{aligned} \quad (\text{A.12})$$

at the minimum, obtained by varying  $\lambda$ ,

$$\mathbf{h}_i \cdot \nabla E = -\mathbf{h}_i \cdot \mathbf{g}_{i+1} = 0. \quad (\text{A.13})$$

Using this condition and equation A.10, A.13 is the same as A.5. It is therefore possible to find the minimum of the total energy without ever evaluating the Hessian matrix **A**.

## Appendix B

### Johnson's long-range potential

As I mentioned in chapter 3, the gold-silver alloy was treated a bit differently from the other alloys. Instead of using a first-neighbor interaction, I have used a long-range one, going up to the thirteenth neighbor, developed also by Johnson (1990). It is essentially an extension of the embedded-atom potential presented in chapter 3.

The basic equations are the same as the one given in chapter 3. The energy is a sum of a repulsive pair potential and an attractive electron-density term

$$E_t = \sum_{\langle ij \rangle} \phi(r_{ij}) + \sum_i F(\rho_i), \quad (\text{B.1})$$

$$\rho_i = \sum_{j \neq i} f(r_{ij}), \quad (\text{B.2})$$

with

$$F(\rho) = E_c \left\{ 1 + \alpha \left[ \left( \frac{\rho_e}{\rho} \right)^{1/\beta} - 1 \right] \right\} e^{\alpha \left[ \left( \frac{\rho_e}{\rho} \right)^{1/\beta} - 1 \right]} - \phi_e \left[ \left( \frac{\rho}{\rho_e} \right)^{\gamma/\beta} - \frac{\gamma}{\beta} \left( \frac{\rho}{\rho_e} \right) \right]. \quad (\text{B.3})$$

The parameter  $\alpha$  depends on the core energy  $E_c$ , the bulk modulus  $B$ , and the

atomic volume  $\Omega$ ,  $\alpha = \sqrt{9\Omega B/E_c}$ . The exponents  $\beta$  and  $\gamma$  are given by

$$\beta = \sqrt{\frac{15\Omega G E_c E_{lv}^f}{(E_{lv}^f + E_c) E_{lv}^f}}, \quad (\text{B.4})$$

$$\gamma = \sqrt{\frac{15\Omega G (E_{lv}^f + E_c)}{E_{lv}^f E_c}} \quad (\text{B.5})$$

where  $G$  is the shear modulus.

Moreover, in this potential the electron-density function and the pair potential are given by

$$f(r) = f_e \left[ \frac{r_{1e}}{r} \right]^\beta \quad (\text{B.6})$$

and

$$\phi(r) = \phi_e \left[ \frac{r_{1e}}{r} \right]^\gamma \quad (\text{B.7})$$

where the parameters  $f_e$  and  $\phi_e$  are scaled a weighted sum of the atoms in the first  $n$  neighbor shells:

$$f_e = \frac{E_c}{S_\beta \Omega}, \quad S_\beta = \sum_{i=1}^n \frac{N_i}{k_i^\beta}, \quad (\text{B.8})$$

$$\phi_e = 2 \frac{E_c}{S_\gamma}, \quad S_\gamma = \sum_{i=1}^n \frac{N_i}{k_i^\gamma}, \quad (\text{B.9})$$

where  $N_i$  is the number of atoms in the  $i$ th shell and  $k_i$  is the distance a the  $i$ th shell to the central atom in units of  $r_1$ ,  $r_i = k_i r_1$ .

# Bibliography

Ackland, G. J., and V. Vitek (1990), *Phys. Rev. B* **41**, 10324.

Ancillitto, F. and A. Selloni (1992), *Phys. Rev. Lett.* **68**, 2640.

Balzarotti, A. (1987), in *Ternary and Multinary Compounds*, Eds. S. K. Deb and A. Zunger, Materials Research Society, Pittsburgh, PA, p. 333.

Bidwell, L.R. (1964), *Acta Cryst.* **17**, 1473.

Boyce, J. B. and J. C. Mikkelsen, Jr. (1985), *Phys. Rev. B* **31**, 6903.

Brock, J. D, R. J. Birgeneau, J. D. Litster and A. Aharony (1989), *Contemporary Physics* **30**, 321.

Brock, J. D. (1992), in *Bond-Orientational Order in Condensed Matter Systems*, ed. K. J. Strandburg, Springer-Verlag, New York, 1.

Bublik, V. T., S. S. Gorelik, A. A Zaitsev, and A. Y. Polyakov (1974), *Phys. Stat. Sol. B* **66**, 427.

Cai, Y, J. S. Chung, M. F. Thorpe and S. D. Mahanti (1990), *Phys. Rev. B* **42**, 8827.

Cai, Y. and M. F. Thorpe (1992a), *Phys. Rev. B* **46**, 15872.

- Cai, Y. and M. F. Thorpe (1992b), *Phys. Rev. B* **46**, 15879.
- Chen, J. and M. F. Thorpe (1992), unpublished.
- Chui, S. T. (1983), *Phys. Rev. B* **28**, 178.
- Coles, B. R. (1964), *J. Inst. Metals* **84**, 346.
- Darby, J. B. and K. M. Myles (1972), *Met. Trans.* **3**, 653.
- Daw, M. S., and M. I. Baskes (1983), *Phys. Rev. Lett.* **50**, 1285.
- Daw, M. S. and M. I. Baskes (1984), *Phys. Rev. B* **29**, 6443.
- de Gironcoli, S., P. Giannozzi, and S. Baroni (1991), *Phys. Rev. Lett.* **66**, 2116.
- Dismukes, J. P., L. Ekstrom and R. J. Paff (1964), *J. of Phys. Chem.* **68**, 3021.
- Ebert, H., J. Abart, and J. Voitländer (1983), *J. Less-Common Met.* **91**, 89.
- Elliott, R. J., Krumhansl, J. A. and Leath, P. L. (1974), *Rev. Mod. Phys.* **46**, 465.
- Elliott, S. R. (1989), *Adv. in Physics* **38**, 1.
- Feng, S., M. F. Thorpe and E. J. Garboczi (1985), *Phys. Rev. B* **31**, 276.
- Feynman, R. P. (1939), *Phys. Rev.* **56**, 340.
- Finnis, M. W., and J. E. Sinclair (1984), *Phil. Mag. A* **50**, 45.
- Foiles, S. M. (1985), *Phys. Rev. B* **32**, 7685.
- Fournet, G. (1953), *J. phys. radium* **14**, 374.
- Friedel, J. (1955), *Phil. Mag.* **46**, 514.

- Halperin, B. I. and D. R. Nelson (1978), *Phys. Rev. Lett.* **41**, 121.
- Hayes, T. M. and J. B. Boyce (1982), *Solid State Physics*, vol. 37, Academic Press, New York, 173.
- He, H. and M. F. Thorpe (1985), *Phys. Rev. Lett.* **54**, 2107.
- Hume-Rothery, W. (1948), *Electrons, Atoms, Metals and Alloys*, Cassies Co., London.
- Ichimura, M., Yoichi Nishino, Hiroshi Kajiyama and Takao Wada (1990), *Jap. Jour. of Appl. Physics* **29**, 842.
- Incoccia, L. , S. Mobilio, M. G. Proietti, P. Fiorini, C. Giovannella, and F. Evangelisti (1985), *Phys. Rev. B* **31**, 1028.
- Itaya, K, R. Sugawara, Y. Morita and H. Tokumota (1992), *Appl. Phys. Lett.* **60**, 2534.
- Jacobsen, K. W. (1988), *Comments Cond. Mat. Phys.* **14**, 129.
- Jaros, M. (1985), *Rep. Prog. Phys.* **48**, 1091.
- Jesson, D. E., J. J. Pennycook, J.-M. Barribeau and D. C. Houghton (1992), *Phys. Rev. Lett.* **68**, 2063.
- Johansson, C. H. and J. O. Linde (1930a), *Ann. Phys. (Leipzig)* **6** , 458.
- Johansson, C. H. and J. O. Linde (1930b), *Ann. Phys. (Leipzig)* **7**, 408.
- Johnson, R. A. (1988), *Phys. Rev. B* **37**, 3924.
- Johnson, R. A. (1989), *Phys. Rev. B* **39**, 12554.

- Johnson, R. A. (1990), Phys. Rev. B **41**, 9717.
- Jones, R. S. (1990), Phys. Rev. B **41**, 3256.
- Kajiyama, H., S.-I. Muramatsu, T. Shimada, and Y. Nishino (1992), Phys. Rev. B **45**, 14005.
- Karmazin, L. (1969), Czech. Jour. of Physics **19**, 634.
- Keating, P. N. (1966), Phys. Rev. **145**, 637.
- Kirkwood, J. G. (1939), J. Chem. Phys. **7**, 506.
- Kleinert, H. (1983), Phys. Lett. **95A**, 381.
- Klement, Jr., W., and H. L. Luo (1963), Trans. Metall. Soc. AIME **227**, 1253.
- Kosterlitz, J. M. and D. J. Thouless (1973), Phys. C: Solid State Phys. **6**, 1181.
- Landau, L. D. and E. M. Lifshitz (1990), *Statistical Physics, part 1*, translated by J. B. Sykes and M. J. Kearsley, Pergamon Press, Oxford, 544pp.
- Lihl, F., H. Ebel, and W. Baumgartner (1971), Z. Metallkde **62**, 42.
- Linde, J. O. (1932), Ann. Phys. **15**, 249.
- Mackenzie, K. D., J. R. Eggert, D. J. Leopold, Y. M. Li, S. Lin, and W. Paul (1985), Phys. Rev. B **31**, 2198.
- Maley, N. and J. S. Lannin (1987), Phys. Rev. B **36**, 1146.
- Martins, J. L. and A. Zunger (1986), Phys. Rev. Lett. **56**, 1440.
- Matsuura, M., J. M. Tonnerre and G. S. Cargill III (1991), Phys. Rev. B **44**, 3842.

- Mealand, A. and T. B. Flanagan (1964), *Can. J. Phys.* **42**, 2364.
- Mermin, N. D., 1968, *Phys. Rev.* **176**, 250.
- Meyer, E. (1993), Private communication.
- Meyer, E. and Heinzlmann, H. (1992), in *Scanning tunneling microscopy I*, H.-J. Güntherodt and R. Wiesendanger eds., Springer-Verlag, Berlin, 99.
- Mikkelsen, J. C. Jr. and J. B. Boyce (1982), *Phys. Rev. Lett.* **49**, 1412.
- Mikkelsen, J. C. Jr. and J. B. Boyce (1983) *Phys. Rev. B* **28**, 7130.
- Mousseau, N. and L. J. Lewis (1990), *Phys. Rev. B* **41**, 3702.
- Mousseau, N. and M. F. Thorpe (1992a), *Phys. Rev. B* **45**, 2015.
- Mousseau, N. and M. F. Thorpe (1992b), *Phys. Rev. B* **46**, 15 887.
- Mousseau, N. and M. F. Thorpe (1993), (to be published *Phys. Rev. B*).
- Murray, C. A. (1992), in *Bond-Orientational Order in Condensed Matter Systems*, ed. K. J. Strandburg, Springer-Verlag, New York, 137.
- Nagakura, S., S. Toyama, and S. Oketani (1966), *Acta Metal.* **14**, 73.
- Nishino, Y., S.-I. Muramatsu, Y. Takano, H. Kajiyama (1988), *Phys. Rev. B* **38**, 1942.
- Nelson, D. R. and B. I. Halperin (1979), *Phys. Rev. B* **19**, 2457.
- Newkirk, J. B. (1953), *J. Metals* **5**, 823.
- Newman K. E. and Dow, J. D. (1983), *Phys. Rev. B* **27**, 7495

- Nix, F. C. and D. Macnair (1941), *Phys. Rev.* **60**, 597.
- Novikova, O. A. and A. A. Rudnitskii (1957), *Zh. Neorg. Khim.* **2**, 1840.
- Osbourn, , G. C. (1982), *J. Appl. Phys.* **53**, 1586. (1986), *IEEE J. Quant. Electron.* **QE-22**, 1677.
- Owen, E. A. and L. Pickup (1934), *Z. Krist. A* **88**, 116.
- Pankove, J. I. and N. M. Johnson (1991), in *Semiconductors and semimetals*, vol. 34, edited by J. I. Pankove and N. M. Johnson (Academic Press, San Diego).
- Pascarelli, S., F. Boscherini, S. Mobilio and F. Evangelisti (1992a), *Phys. Rev. B* **45**, 1650.
- Pascarelli, S., F. Boscherini, S. Mobilio, A. R. Zanatta, F. C. Marques, and I. Chambouleyron (1992b), *Phys. Rev. B* **46**, 6718.
- Pauling, L. (1966), *The nature of the chemical bond*, Ithaca, N.Y., Cornell University Press, page 444.
- Pearsall, T. P. (1990), in *Strained-layer superlattices physics*, Edited by T. P. Pearsall, *Semiconductors and Semimetals*, vol. 32, Academic Press, San Diego, 275+ix pages.
- Pearson, W. B. (1958), *Handbook of Lattice Spacing and Structure of Metals and Alloys*, Pergamon Press, New York.
- Phillips, J. C. (1973), *Bonds and Bands in Semiconductors*, New York Academic Press.

- M. Podgorny, M. T. Czyzyk, A. Balzarotti, P. Letardi, N. Motta, A. Kisiel and M. Zimmel-Starnawska (1985), *Solid State Comm.* **55**, 413.
- Press, W. H., B. P. Flannery, S. A. Teukolsky and W. T. Vetterling (1986), *Numerical Recipes*, Cambridge University Press, 818pp.
- Renaud, G., N. Motta, F. Lançon, and M. Belakhovsky (1988), *Phys. Rev. B* **38**, 5944.
- Schulze, G. and M. Henzler (1983), *Surf. Science* **124**, 336.
- Soven, P. (1967), *Phys. Rev.* **156**, 809.
- Steinmetz, D., F. Ringeisen, D. Bolmont and J. J. Kouzman (1990), *Surf. Science* **273**, 135.
- Stern, E. A. (1985), in *Physical Properties of Amorphous Materials*, Edited by D. Adler, B. B. Schwartz and M. C. Steele, Plenum Press, New York, 201.
- Stott, M. J. and E. Zaremba (1980), *Phys. Rev. B* **22**, 1564.
- Strandburg, K. J. (1988), *Rev. Mod. Phys.* **60**, 161.
- Strandburg, K. J. (1992), *Bond-Orientational Order in Condensed Matter Systems*, Springer-Verlag, New York, 338 pp.
- Stutzmann, M., R. A. Street, C. C. Tsai, J. B. Boyce, and S. E. Ready (1989), *J. Appl. Phys.* **66**, 569.
- Taylor, D. W. (1967), *Phys. Rev.* **156**, 1017.
- Thorpe, M. F. (1983), *J. Non-Cryst. Solids* **57**, 355.

- Thorpe, M. F. and Y. Cai (1991), *Phys. Rev. B* **43**, 11019.
- Thorpe, M. F. and E. J. Garboczi (1990), *Phys. Rev. B* **42**, 8805.
- Thorpe, M. F., W. Jin and S. D. Mahanti (1989), *Phys. Rev.* **40**, 10294.
- Thorpe, M. F. and W. Tang (1987), *J. Phys. C* **20**, 3925.
- Végard, L. (1921), *Z. Phys.*, **5** 17.
- Weidmann, M. R. and K. E. Newman (1992), *Phys. Rev. B* **45**, 8388.
- Wooten, F. (1991), (private communication).
- Wooten, F. and D. Weaire (1987), *Solid State Physics* **40**, 1.
- Wooten, F. and D. Weaire (1987), *Solid State Physics* **40**, 1.
- Wooten, F., K. Winer and D. Weaire (1985), *Phys. Rev. Lett.* **54**, 1392.
- Yishimo, Y., S. Muramatsu, Y. Takano, and H. Kajiyama (1988), *Phys. Rev. B* **38**, 1942.
- Yndurain, F. (1978), *Phys. Rev. B* **18**, 2876.
- Young, A. P. (1979), *Phys. Rev. B* **19**, 1855.
- Zunger, A. and Jaffe J. E. (1983), *Phys. Rev. Lett.* **51**, 662.

MICHIGAN STATE UNIV. LIBRARIES



31293008850962